Mémoire d'Habilitation à Diriger des Recherches

Université Paris 7

# The high-energy universe as a
# laboratory for particle physics

Pierre Brun

*À Anaïs, à Elliot,*

## Remerciements

# Introduction

This manuscript presents part of the work that I have conducted since I joined the Particle Physics Department of the Institute of Research into the Fundamental Laws of the Universe (Irfu), at CEA Saclay. The common thread of my work is based around the idea of advancing particle physics and cosmology by performing measurements of particles in their natural environment. In a sense this approach corresponds to doing *in vivo* particle physics, whereas scientists working on controlled experiments such as those using particle accelerators are doing *in vitro* particle physics. This might be considered very ambitious but it actually recovers the tradition that led until the 50's to the discovery and the study of new particles. In 2012 a new particle has been discovered, with properties that resemble a lot to that of the Higgs particle, which is supposed to explain the masses of elementary particles. The next fundamental particle to be discovered might be the dark matter particle that could explain most of the mass of the universe, or the axion that can solve some of the inconsistencies of the standard model of particle physics. In this report it is argued that natural –astrophysical– environments, in particular those involving high-energy phenomena, can play an essential role in this endeavor. This will mainly be illustrated by the search for a solution to one of the greatest Nature's puzzle, namely the identification of the missing mass of the universe often referred to as the dark matter problem. Over the years, the research presented in this essay has represented an excellent opportunity for me to initiate many pleasant collaborations with physicists mainly from Saclay, Paris, Annecy, Zurich, Erlangen, Tübingen, Heidelberg, Padova, Barcelona and Santa Cruz.

The first chapter is a very short preamble setting the framework of my research. In particular, I introduce the reason why new yet undiscovered fundamental components might exist in the universe. The following three chapters describe part of the research activities that I conducted in that perspective. Chapter 1 is devoted to searches for particle dark matter with charged cosmic rays; some constraints on new physics models are obtained and some limitations of the method are outlined. Chapter 2 mainly deals with searches for new particles using very high-energy gamma rays. This includes dark matter in the form of weakly-interacting massive particles and axion-like particles. In chapter 3, the difficult and essential issue of building instruments capable of breakthrough in the area is addressed. This is done through the example of the development of new kinds of mirrors for ground-based gamma-ray astronomy.

Of course important parts of my work do not appear in the present report. This is the case for all the ideas that turned out to be dead ends and on-going projects that are not yet fully mature. I have been involved in activities such as refereeing for peer-reviewed journals and in scientific committees, particularly with the French INSU national program PNHE (Programme National Hautes Energies) and the European Strategy for Particle Physics conducted by CERN. I have also devoted a significant fraction of my time to teaching and outreach, as well as supervising research students. I have enjoyed giving numerous seminars for the general public and secondary school students. I have also been very involved in teaching general physics to adults returning to full time education at the Université Paris 11, as well as to the students of École Nationale des Techniques Avancées and École des Mines de Paris.

# Contents

**3 Development of mirrors for next-generation Cherenkov telescopes**     **57**

# Preamble: the need for new components in the universe

*"I know this defies the law of gravity, but, you see, I never studied law."*
–Bugs Bunny

Most of the work presented in this document deals with what is referred to as beyond standard model physics. In particular, this work includes the search for new particles that may solve some current puzzles. It is therefore necessary to accurately define our framework, and to motivate the new physics models whose parameters will later be constrained. This preamble is a very brief and incomplete presentation of some of the important open questions in the field of particle physics and cosmology. It is not intended to be a review but rather to provide essential theoretical background needed to understand the following chapters in their context.

## 1 The standard model of cosmology

A general description of a homogeneous and isotropic universe includes a scalar number, which determines if its overall geometry is closed, open or flat. Our observable universe is flat, probably because of an early inflationary phase during which the expansion rate has accelerated. The observable universe is therefore a very small fraction of a larger region, making its flatness natural. It is commonly assumed that inflation ended by a phase called reheating, producing all known particles and perhaps some yet undiscovered ones. From this hot and dense state all further evolution of the universe is described by departures from thermal equilibrium, due to the expansion-induced cooling and dilution. Various phase transitions have occurred and have led to a neutral universe that was re-ionized when the first stars formed. Those stars betrayed the process of the growth of structure that –in a hierarchical way– eventually led to the formation of the biggest observed structures such as galaxies and galaxy clusters. In the latest stage of its evolution, the universe has been experiencing a new accelerated expansion phase, the origin of which is still unknown.

Most of the information we have about the early universe comes from the study of the cosmic microwave background (CMB) that was emitted when the first atoms were formed. The CMB has been discovered in 1965 with microwave antennas [1], at that time no anisotropy was observed. Some degree of anisotropy was expected though, as their origin is the matter inhomogeneity that is necessary to later form galaxies. Almost 30 years later, the proof has been made that the CMB energy density is a perfect blackbody, and that it is anisotropic [2]. Only after the results of the WMAP satellite observations the CMB anisotropies were measured well enough to perform detailed statistical analysis of the information they contain [3]. In 2013 the first results of the Planck mission were released and the data demonstrated a impressive consistency of the current cosmological model. Its energy content is dominated by vacuum energy density and matter. The first one is possibly a fundamental parameter, the cosmological constant $\Lambda$, and is called dark energy. The matter density includes conventional matter, of known type (dubbed baryonic), and matter of a new type, which will be referred to later as dark matter. The relative energy densities of these components are usually expressed as dimensionless numbers corresponding to a fraction of the total energy density. According to the latest measurements by Planck, combined with other cosmological probes [4],

the main cosmological parameters are

$$\Omega_\Lambda = 0.692 \pm 0.01$$
$$\Omega_{\text{cold dark matter}} = 0.259 \pm 0.004$$
$$\Omega_b = 0.0483 \pm 0.0005$$

These numbers are obtained from a fit to the cosmological data including probes of the universe's growth rate and CMB anisotropies[1]. It appears that the baryonic fraction is only a small part of the matter fraction (19%), meaning that there is a large part of the matter content that is non baryonic, in other words of unknown nature.

Despite its stunning consistency, the standard model of cosmology requires three unknown components, namely the field responsible for the inflation, the vacuum energy density and the dark matter. It is important to stress that although well described and understood on large scales, the fundamental components of the universe still lack a microscopic description. As we shall see in the following, the latter would most probably imply new physics.

## 2 The cold dark matter problem

The CMB anisotropies are the imprints of the oscillations of the primordial plasma. When the universe was totally ionized, the two antagonist effects of gravitational attraction and radiation pressure led to oscillations and propagation of sound waves. The related density fluctuations led to the anisotropies that are observed in the CMB at the level of $\delta = \delta\rho/\rho \sim 10^{-5}$, where $\rho$ is the density. The measurements of the CMB anisotropies by WMAP and Planck allow to adjust very finely the parameters that determine the amplitudes of the oscillations at all scales. The results are shown in the form of an angular power spectrum, that displays how the variance of the temperature map is distributed with respect to the angular scale. In Fig. 1, this power spectrum as measured by Planck [4] is shown on the right panel. The peak corresponds to an angular scale of about one degree; it means that the fundamental mode of the primordial oscillations is now seen on a one-degree scale, where most of the map variance comes from.
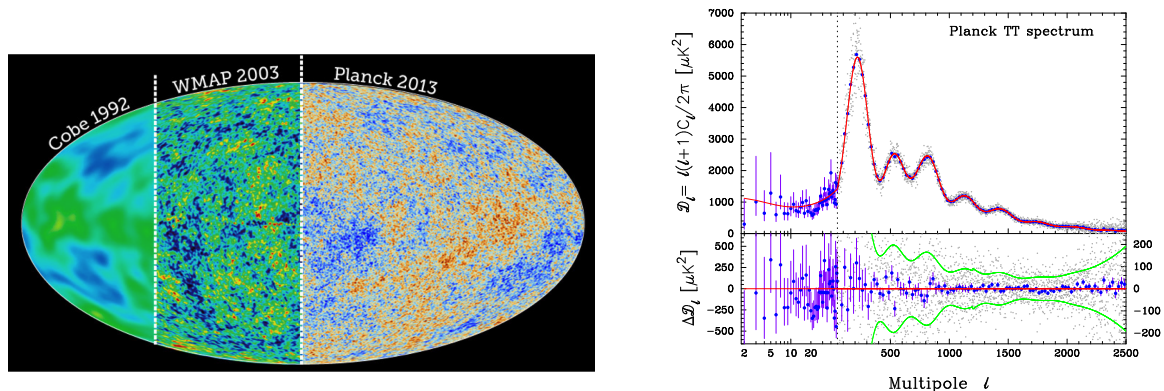


Figure 1: Temperature maps of the cosmic microwave background from COBE, WMAP and Planck (left), and angular power spectrum measured by Planck (right).

The positions and the heights of the peaks are very sensitive to the energy content of the universe at the time when the CMB was emitted. A fit of the shape of the power spectrum allows determining the

---

[1]These numbers are obtained with a Hubble constant $H_0 = 67.8$ km/s/Mpc.

proportion of the different components. This requires the introduction of non-baryonic matter which does not couple to light, that is dark matter. As an illustration, one can try to replace the dark matter by known components like neutrinos or baryons. In the left panel of Fig. 2 this is done for neutrinos, and in the right panel of Fig. 2, this is done for baryons. It appears obvious that replacing dark matter with *e.g.* neutrinos would be in serious conflict with the measurements.
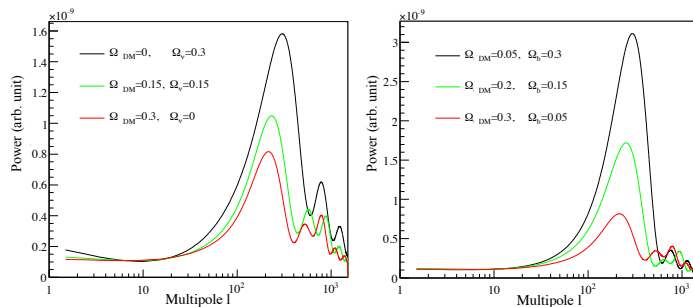


Figure 2: Simulations of CMB angular power spectrum by replacing dark matter by neutrinos (left) and baryons (right). In both cases the red curve is close to the actual measurements. These simulations have been performed with the CMBFAST package [5, 6].

One can notice that the CMB homogeneity seems to be in conflict with the very existence of galaxies. Indeed, the CMB radiation shows a homogeneous universe at the level of $\delta = \delta\rho/\rho \sim 10^{-5}$, whereas nowadays obviously $\delta \gg 1$. As $\delta$ grows proportionally to the scale factor of the metric, if the universe was as homogeneous as the CMB was at recombination, $\delta$ would be of the order of $10^{-2}$ at present. This simple fact points out to the need to introduce a new type of matter which could present larger fluctuations already at the time of recombination. In order not to affect the CMB –which is very well described with known particles–, such new type of matter must not interact with light, therefore being non-baryonic. The overall cosmological fit including other probes that the CMB yields the following proportions for the matter component of the universe, 84% is non-baryonic *i.e.* of unknown type, 15.6% is baryonic and does not emit light, 0.4% emits light (see Fig. 3).
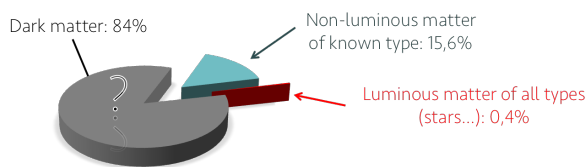


Figure 3: Composition of the matter in the universe.

The cosmological dark matter discussed in previous paragraphs is indeed observed not only on the largest scales, but actually at all scales from galaxy clusters down to Galactic satellites. The large-scale structure of the universe displays a filament-like structure, which is correctly described by numerical simulations that include dark matter. These simulations show that the dark matter particles have to be cold, *i.e.* their motions in the universe have to be non-relativistic. If this condition is not satisfied, the potential wells in which galaxies are supposed to form are not deep enough, resulting in a universe that is not clustered enough. Figure 4 illustrates this point: in the left panel, dark matter is hot (like if it was neutrinos), in the central panel, dark matter is warm (as in the case of hypothetical massive neutrinos), and in the right panel, dark matter is cold. Actual observations show that the universe resembles more the right panel.
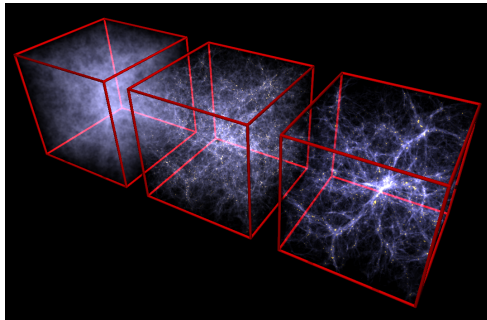
Figure 4: Simulation of structure formation with hot, warm and cold dark matter (resp. left, middle, right). The observed structure of the universe has the properties of the right panel, showing that dark matter is most likely a cold component (figure from [7], obtained with data from [8]).

On the scale of galaxy clusters, it has first been noticed in 1933 that the mass of galaxy clusters obtained from galaxy counts is not compatible with the mass inferred from the study of their motion. In [9, 10], the virial theorem is used to estimate the mass of the Coma cluster. The large discrepancy observed at that time led to the introduction of the term "dark matter". Recent observations of the remnants of galaxy cluster collisions allow to even deduce some properties of the dark matter. In [11], such a collision is observed in 1E0657-558 (the so-called bullet cluster) with two complementary methods. X-ray data from the Chandra satellite allow to locate the hot gas, warmed up by the friction during the encounter, and data from the Hubble Space Telescope are used to map the mass by gravitational lensing of the background image. These images are shown in Fig. 5, they show a clear spatial separation between the gas and the mass. This observation is of paramount importance in the determination of the nature of dark matter. It shows an astrophysical system where the conventional matter is physically separated from the mass. Owing to its nature, the conventional matter has the property to heat up when compressed, this is what the X-ray observations display. On the opposite, the optical observations of gravitational lensing reveal another kind of matter that does not heat up when it is compressed and went through the cluster collision without interacting. Such a kind of matter is called collisionless, the nature of which is by definition unknown. The observation of the bullet cluster allows us to rule out theories where dark matter does not exist but rather appears as an illusion due to the modification of the gravitational laws through which the motion of astronomical objects are interpreted. In all modified gravity models, the source of the gravitational potential is always the conventional matter, so that the mass of galaxy clusters could not be physically separated from it.

There is strong evidence that the missing mass observed indirectly in the CMB, the large scale structures and galaxy clusters is also present at the galactic scale. It has been shown in 1978 that the rotation curves of galaxies are flat, indicating the presence of an extended invisible mass halo [12]. This is illustrated in the left panel Fig. 6 for a collection of galaxies. Our own Galaxy makes no exception, though harder to measure, the rotation curve of the Milky Way reveal the presence of dark matter, as shown in the right panel of Fig. 6 [13]. The search for microlensing events showed that the dark matter in the Milky way cannot be made of 100% of compact objects [14], an upper limit of 8% has been set [15].

On scales smaller than the Galactic scale, dark matter is observed in Milky-Way satellites. In dwarf spheroidal galaxies, the velocity dispersion of stars indicate the presence of a dark matter halo, the profile of which can be fitted to the observation, as shown in Fig. 7 from [16]. Numerical simulations of structure formation on the scale of Milky-Way-sized galaxies predict the presence of even smaller dark matter structures, dark matter clumps. The largest of them accreted baryons and are visible through the stars they harbor, like in the case of dwarf galaxies. Smaller clumps are likely present in the Milky Way without being massive enough to contain baryons. They are essentially invisible, Fig. 8 displays a view of the Galaxy if dark matter was visible [17].
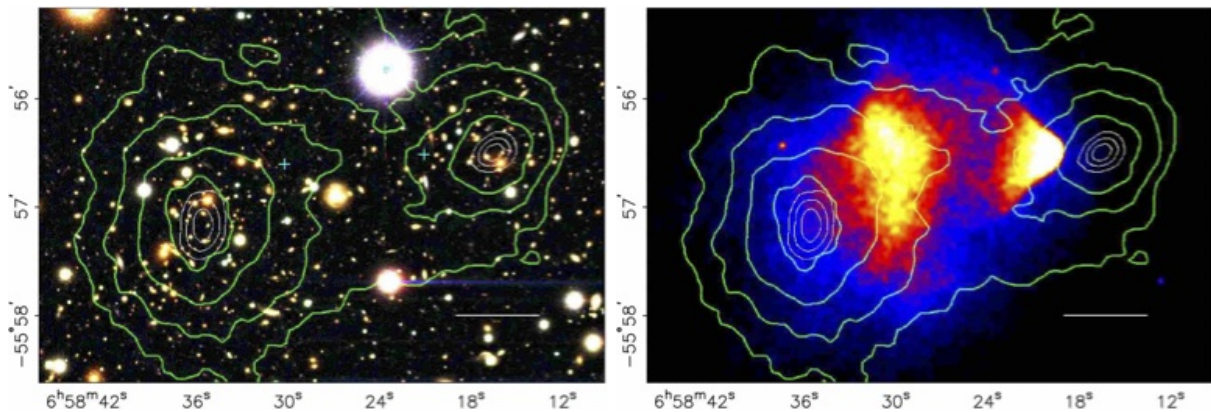
Figure 5: Observation of the bullet cluster, in the left panel, the contours represent the mass deduced from gravitational-lensing-induced deformation of the background image, in the right panel these contours are superimposed on the image of the same field observed in X rays [11]. This observation shows that dark matter must be composed of massive particles with weak interactions.
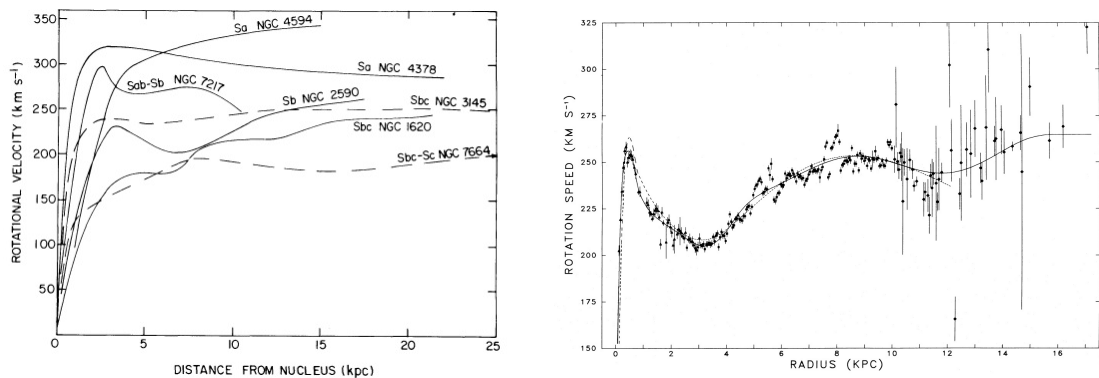


Figure 6: Rotation curves of external galaxies (left [12]) and of the Milky Way (right [13]). The flatness of the rotation curves indicates the presence of extended dark matter halos around galaxies.

## 3    Some problems related to the cold dark matter paradigm

Though very appealing, the cold dark matter hypothesis is not problem-free. In particular, some of the predictions related to its dissipationless nature are not verified, in particular on small scales. For example, a generic prediction of the cold dark matter model is that the center of structures should exhibit cuspy density profiles. Although some bias must exists between dark matter and baryonic matter, the observed baryonic density profiles are always cored, which is not easy to explain. Simulations based on pure cold dark matter also predict massive satellites to be present in the close environment of Milky-Way-size galaxies, that are not observed [18]. Such simulations also predict a larger number of satellites than what is actually observed [19]. In summary, the cold dark matter hypothesis is challenged on small scales and in regions where the dark matter density is high.

Should dark matter be warm, these problems would not arise but, as seen above, warm dark matter is not favored by the CMB measurements and the properties of large scale structures. The missing satellite problem itself is probably explained in part by the fact that many faint satellites could remain undetected [20]. One possible mechanism is the feedback from baryons on the dark matter density [21, 22]. In that case, supernovae explosions could be responsible for the disruption of the cores and the Milky-Way satellites, and also explain why the most massive subhalos are not observed. It would be however

5
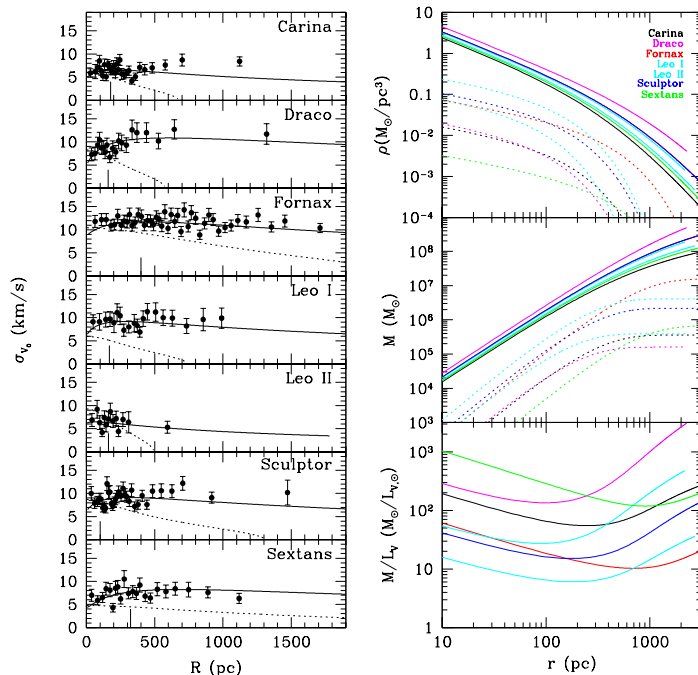
Figure 7: Velocity dispersion of stars in seven Milky Way dwarf galaxies, together with the fit of the dark matter mass profile (figure from [16]).

surprising that this mechanism could work efficiently even in very faint Milky-Way satellites, the reason being that there is probably not enough baryonic content [23]. One interesting possibility is that dark matter particles have a significant self-scattering cross section (this is the model of "self-interacting dark matter") [24]. In that case, the predictions for large scale structures are identical, but the inner parts of the halos are expected to be cored, and the most massive subhalos simply do not form. These models can be tested for instance by studying mergers like the bullet cluster or galaxy-cluster mergers [25].

# 4    The standard model of particle physics and beyond

The standard model of particle physics is based on the concept of gauge symmetry. Strong interactions are well described by quantum chromodynamics (QCD) with a SU(3) local symmetry that applies to the color charge of quarks and gluons. Electromagnetic and weak interaction are nicely described in a unified way by a local SU(2)×U(1) symmetry where the SU(2) group is related to rotations of left-handed particles within doublets and U(1) is related to hypercharge. Exact SU(2)×U(1) symmetry implies massless gauge bosons, which is at odds with the observation of the very massive $W$ and $Z$ bosons. This means that the symmetry is broken at low energy, according to the Higgs mechanism. The cornerstone of the standard model is therefore the Higgs particle which has likely been observed at the LHC in 2012 [26, 27]. The standard model of particle physics reproduces all current accelerator data with an incredible precision and no experimental result has yet really challenged the model [28].

However, the model has some known limitations. For example, if the Higgs particle is confirmed to be an elementary scalar boson, its mass should be very sensitive to radiative corrections. For its value to be stabilized at the observed value of less than 130 GeV, new physics must come into play at energies not much above the TeV scale. Otherwise the standard model parameters would need to be very fine tuned. These new phenomena could be compositeness of the Higgs particle, new particles or extra-dimensions
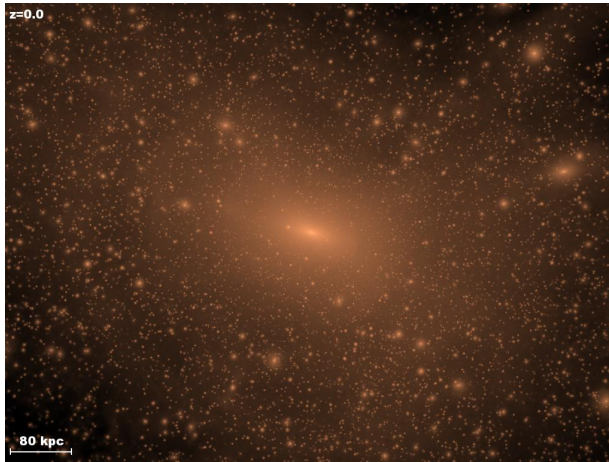
Figure 8: Stucture of the Milky Way dark matter halo obtained from numerical simulations [17]. The scale of the image is such that the visible Galactic disk would be entirely contained in the central dense region.

for example. It cannot be excluded for instance that one of the new particles related to the Higgs mass stabilization has something to do with the cosmological cold dark matter. Another limitation of the standard model is aesthetic in some sense. When the interaction strengths of the three gauge interactions are extrapolated at high energy, they nearly converge to a common value but not exactly and it would be satisfying if they did. This can be realized in models beyond the standard model that assume the existence of new particles. Also, the standard model does not include gravitation, and any physics observable that can reach the Planck scale is interesting in that respect. Perhaps the first indication of beyond standard model physics from laboratory data is neutrino masses. In the strict framework of the standard model, neutrinos are massless and the introduction of mass terms is formally a first order correction beyond the standard model [29]. It is interesting to note then that this hint for beyond-standard-model physics partly comes from the observation of an extraterrestrial source of neutrino –the Sun– (in addition to beam experiments, atmospheric production and reactor experiments) showing that *in vivo* particle physics has already been fruitful in the recent past.

# 5 Hypothetical new particles relevant to cosmology: WIMPs and axions

Independently from the cosmological arguments presented above, models beyond the standard model of particle physics can predict the existence of new massive stable particles that have the required properties to make up the cosmological non-baryonic matter, called dark matter (DM) in the following. A widely studied case is the one of neutral massive particles that only interact through the weak interaction. These new particles are weakly interacting massive particles called WIMPs (see [30] for a review). Interestingly enough, these DM candidates were originally not proposed to solve the non-baryonic matter issue but were introduced when trying to address the limitations of the standard model. The current cosmological WIMP DM density is determined by their annihilation rate in the early universe. This provides a natural value for the annihilation cross section of $\langle \sigma v \rangle \sim 3 \times 10^{-26}$ cm$^3$s$^{-1}$, where $\langle \sigma v \rangle$ is the velocity-weighted annihilation cross-section. Such a value happens to be very close to what would be expected for a generic weakly interacting particle. In fact, the cosmological value of the annihilation cross-section is deduced from the physics of the early universe, which should not have anything to do with the electroweak scale. This coincidence is often seen as an invitation to consider that the link between cosmology and particle physics is materialized because the cold dark matter is indeed composed of WIMPs. As we shall see in

7

the next chapters, this value for the cross section defines a clear target for experiments that are sensitive to the annihilation signals.

One aspect of the standard model that is not completely understood is the absence of charge-parity (CP) violation in QCD. The most general QCD Lagrangian includes a complex phase term which –if not exactly zero– induces CP violation. The non-observation of even a very small electric dipole moment for the neutron [31] implies that this phase is smaller than $10^{-11}$. This fact alone seems unnatural and calls for an explanation. A possible one is given by making this phase a dynamical field whose value is driven to zero by the action of its classical potential. This is made possible by the introduction of a new U(1) global symmetry which is spontaneously broken at some scale $f$ (this is the so-called Peccei-Quinn symmetry [32]). A new particle, called the axion, is then predicted as the associated pseudo Nambu-Goldstone boson [33, 34]. In the original idea of Peccei and Quinn, $f$ was of the order of the electroweak scale (EW), implying a mass of $\sim$100 keV for the axion, which was quickly ruled out (see [35, 36] for details). It was then proposed that $f$ was much greater than the EW scale, leading to a very light and weakly interacting axion (dubbed the "invisible axion"). Axions are good candidates to form the cold dark matter. Although they are light, they could act as cold dark matter as they would form Bose-Einstein condensates [37]. If dark matter was made of axions, galaxy formation would have occurred the same way as if it had been WIMPs.

The mechanism that leads to axions is very generic and many models actually predict the spontaneous breaking of a global U(1) symmetry at high energy, resulting in the prediction of axion-like particles (ALPs, see for instance [35]). ALPs can couple to photons in the same way as axions, but unlike axions their coupling strength and mass are generally independent parameters. In general ALPs do not provide a solution for the strong CP problem, only some realizations of ALP models do [38]. ALPs are ubiquitous in string theory, for which $f$ can be of the order of the string scale and $m$ can be as low as $10^{-13}$ eV [39, 40, 41]. In some regions of the parameter space, and even at these very low masses, ALPs are also good candidates to form the cold dark matter of the universe [42]. These ALPs could have been produced by different mechanisms in the early universe, either thermally or non-thermally [42].

# 6  Relevance of the observation of the high-energy universe

Astrophysical environments, and in particular the high-energy universe, offer peculiar physical conditions which one can take advantage of to search for new phenomena. Concerning the search for dark matter annihilations, the Earth environment is obviously not the best location. Indeed given the dark matter density at the Earth, a pair of 500 GeV WIMPs is typically found in a 15 cm cube, making them unlikely to collide. It is then natural to look for locations where the DM density is large: close to black holes, in dwarf galaxies or at the center of galaxy clusters. The observation of these objects at very-high energy is particularly interesting because the DM annihilation signals are expected in the energy ranges close to the DM mass. High energies in the universe are often associated with large magnetic fields or large magnetized regions, which can be of primordial importance in the search for axions. Also, very distant high-energy sources are interesting because high-energy particles travel cosmological distances. These long baselines allow to probe the metric, to perform searches for exotic mixing between photons and new particles, or to search for violation of the Lorentz invariance. In the next chapters, concrete examples of the use of high-energy messengers for these types of quests are developed.

# Chapter 1

# Charged cosmic rays and particle dark matter

*"Okay, wise guys, you always wanted me to catch him. Now what do I do?"*
–W.E. Coyote

## 1   Introduction

This section deals with a possible exotic origin of GeV to TeV cosmic rays. Emphasis is put on some sub-dominant species, such as positrons and antiprotons. One objective of the precise measurement of the abundance and energy distribution of those species is related to the search for WIMP dark matter. Indeed, it has long been thought to be a promising channel for the search of dark matter particle annihilations in our Galaxy. The main reason is that the conventional production of antimatter particles was expected to be marginal whereas annihilations of dark matter particles would produce matter and antimatter evenly. Over the last years, new measurements have been performed with the PAMELA and Fermi satellites, AMS-02 onboard the International Space Station as well as the balloon-borne ATIC detector and ground-based Cherenkov telescopes. It is now established that not all these measurements are correct, in particular thanks to the precision of the AMS-02 spectrometer. The study of these observations and the adjustment of exotic signals has however been a nice pretext to reassess deeply the possibility of using the cosmic ray channel to search for dark matter particles, so these observations led to a deep reconsideration of the issue of dark matter searches through cosmic rays.

Together with the LAPTH group led by Pierre Salati in Annecy we developed codes describing the propagation of charged particles in the Galaxy. These codes use semi-analytical models whose equations can be solved very quickly, allowing to perform scans over the parameter space of the propagation models. This is particularly useful because it allows to estimate the theoretical errors on the conventional cosmic ray background and the expected signal. We used these codes when the results from PAMELA came out. In particular, we were able to rapidly publish a study showing that the antiproton measurements leave little room for exotic signals, even taking into account the model uncertainties [43]. In the same study, we showed that common WIMPs could not explain the positron fraction rise without violating the antiproton constraints. Our result gave birth to the so-called *leptophilic* models, for which the antiproton production is suppressed, and generated a great deal of interest in the literature. In the meantime, I participated in the development of the `micrOMEGAs` code, in particular its indirect detection module, which predicts signals in all channels from any exotic signal [44]. This code is now extensively used by the community. After that, independent studies showed that leptophilic models were in tension with other observables, such as radio data or the CMB. Then, a remaining possibility was that the positron excess was due to a nearby substructure. I studied this possibility, in particular with Stefano Profumo and Jürg Diemand during a visit at UC Santa Cruz. We used state-of-the-art numerical simulations of dark matter structures

in the Galaxy and ruled out this possibility [45]. These pieces of work contributed to rule out WIMP dark matter as reasonable candidates to explain the observed cosmic ray anomalies. This chapter tells this story; first, measurements of cosmic particles in the GeV to TeV range are presented, then a short introduction on how particle dark matter signals are estimated is given in Sec. 3. Sec. 4 deals with the fits that can be performed to the data. Sec. 5 and 6 consider the possibilities for signal enhancements that are required to account for the observations. In Sec. 7, these hypotheses are balanced against conventional scenarios. Finally, some prospects are discussed in Sec. 8.

## 2 Cosmic particles in the GeV to TeV range

### 2.1 Observations of cosmic particles

The observation of high energy cosmic particles requires a medium in which they deposit their energy. The particle identification and the measurement of its energy depend on the type of medium and instrumentation. In the energy range of interest here, the vast majority of the particles hitting the top of the atmosphere consists of protons. This fact is shown in Fig. 1.1 and Fig. 1.2, in which the spectra of protons, Helium and electrons are displayed. These spectra are approximately power laws with large indices so to be more readable, the spectra are re-weighted with a power law. At 1 GeV the weight is the same for all spectra and one can see that most of the incoming particles are protons, with a factor of 10 less in flux come Helium nuclei, and electrons come with a further factor of 10 less. Therefore, the environment is charge asymmetric and it is much more difficult to identify a positively charged particle that is not a proton than a negatively charged particle.
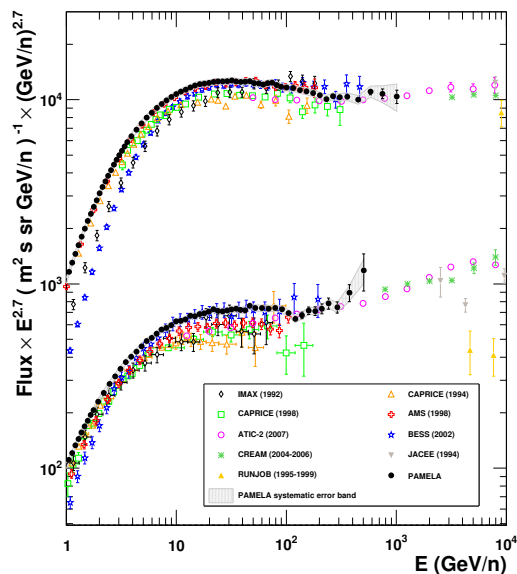


Figure 1.1: Flux of proton and Helium nuclei between 1 GeV per nucleon and 10 TeV per nucleon, figure from [46].

Different experiments measure these fluxes, and essentially they fall into two categories: magnetic spectrometers and calorimeters. For the first ones, magnets are used, the size of which determines the acceptance of the detector. Different subsystems are used to identify the nature of the particles, in addition to tracking its way inside the magnet to determine its charge. Calorimeters are primarily designed to measure the energy of electromagnetic particles –electrons, positrons and photons– and have been used

in the past few years to measure the fluxes of cosmic electrons and positrons. More details about these detectors are given in the following section but now one can see there are two classes of measurements when it comes to measuring electrons and positrons. Magnetic spectrometers can measure electrons and positrons separately and calorimeters measure the flux of the sum of electrons and positrons (diffuse gamma rays are neglected below 1 TeV). This distinction is made in Fig. 1.2, with blue data points indicating a measurement of the sum of electrons and positrons. Positrons have long been expected to be in minority but as shown in Fig. 1.3, the positron fraction rises at high energy, up to a level of about 1/3. What happens at higher energies is currently unclear.
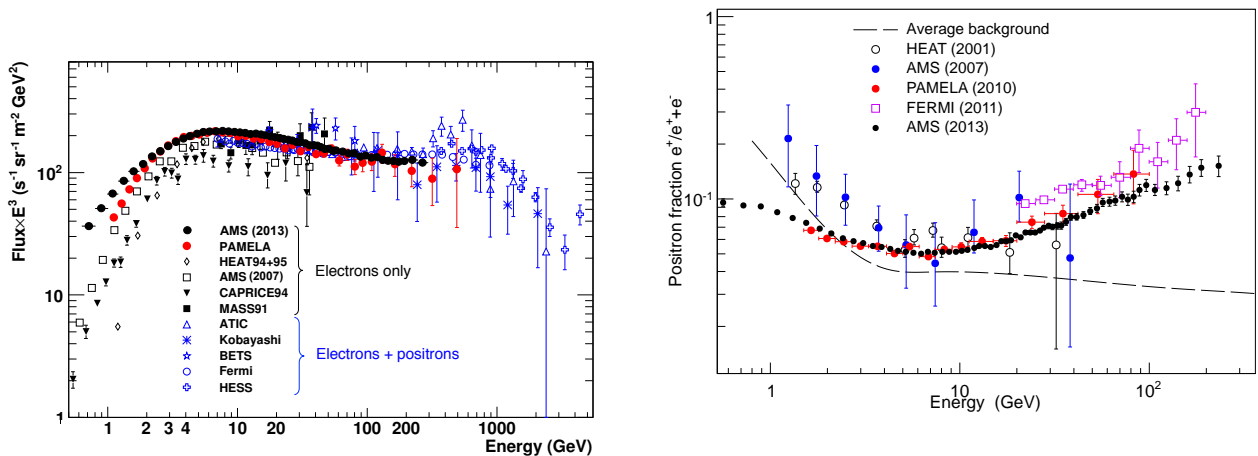


Figure 1.2: Electron and positron spectra between 1 GeV and 4 TeV, adapted from [47].
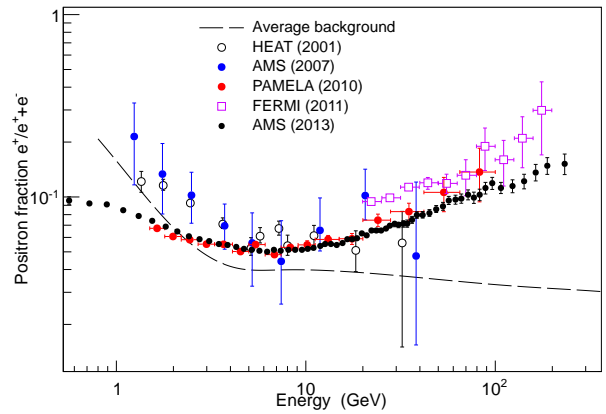


Figure 1.3: Positron fraction in the range from 1 GeV to 200 GeV. The dashed line represents the average expected background from secondary positron production in the Galaxy, data are from [48], [49], [50], [51] and [52].

After positrons, the other antimatter particle observed in the cosmic ray species is the antiproton. At 1 GeV the antiproton flux is $\sim 10^{-2}$ particles per GeV, per $m^2$, per s and per sr, a factor of $10^4$ less than protons. To have a purity of only 10%, a rejection factor of at least $10^5$ is required, which is only achievable with the identification capabilities allowed by magnetic spectrometers. Fig. 1.4 and Fig. 1.5 show the antiproton flux and the antiproton to proton ratio respectively, for kinetic energies between 100 MeV to 100 GeV.

For all species, the apparent discrepancy between different measurements at low energy is not worrisome, it is due to solar modulation; the data have been taken at times when Solar activity was different. Solar modulation only concerns measurements below a few GeV. In particular for positrons the real problem lies at higher energies.

## 2.2   Experiments whose results are discussed here

In this short section, some details are given about the detectors that allowed the measurements discussed in this chapter. The main part of the data that is of interest here was provided by five very different experiments between 2008 and 2013. As we shall see these results have been subsequently widely discussed in the literature.

PAMELA is a satellite borne spectrometer launched in June 2006 [54]. This experiment provided the first firm observation of a rise of the positron fraction [50], although hints had previously been found [48, 49] (see Fig. 1.3). The PAMELA experiment comprises: a time-of-flight system, a magnetic spectrometer with silicon tracker planes, an anticoincidence system, an electromagnetic imaging calorimeter, a shower tail catcher scintillator and a neutron detector. The presence of a lead-scintillator electromagnetic calorimeter
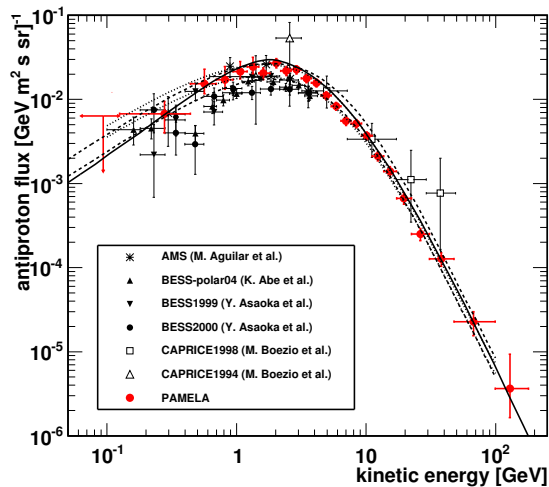
Figure 1.4: Antiproton flux for kinetic energy ranging from 100 MeV to 100 GeV, figure from [53]. The solid line represents the expected conventional flux, and the dotted lines represents the associated theoretical uncertainty (see text for details).
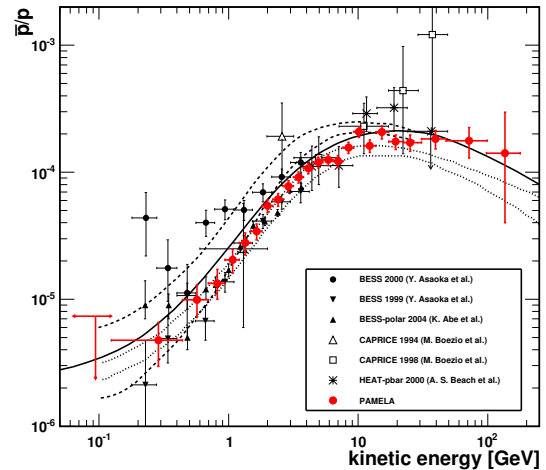
Figure 1.5: Antiproton to proton ratio for kinetic energy ranging from 100 MeV to 100 GeV, figure from [53]. The lines represent different estimates of the ratio values in conventional scenarios.

allows to reach an energy resolution of the order of 6%. Antimatter identification is limited in energy by spillover effects to 190 GeV for antiprotons and 270 GeV for positrons. If positrons are not separated from electrons, the apparatus is able to measure the total flux up to 2 TeV. As shown in Fig. 1.2, the measurements are not limited by statistics and extend up to ~ 600 GeV. PAMELA provided the most accurate measurement of antiproton fluxes to date, thanks to its advanced identification capabilities and relatively large aperture. PAMELA results for antiprotons are displayed in Fig. 1.4 and Fig. 1.5, together with earlier measurements.

ATIC is an experiment originally designed to measure the charge composition and energy spectra of cosmic ray nuclei in the 100 GeV to 10 TeV range [55]. The detector comprises a large electromagnetic calorimeter that permits to measure the $e^+ + e^-$ flux up to about 1 TeV. The experiment is balloon borne and two flights led to the results reported in Fig. 1.2. Those flights carried the detector at an altitude of about 37 km above Antarctica in 2000 and 2002. Due to the depth of the calorimeter, the energy resolution is of the order of 2% in the case of electrons. For electron analyses, the threshold of the experiment is 20 GeV and above 2 TeV the proton and photon backgrounds become too important. In 2008 the ATIC experiment reported the observation of an excess in the electron plus positron flux in the 300-800 GeV range [56].

Fermi is a satellite borne experiment designed for gamma-ray astronomy in the 100 MeV to 300 GeV range and the study of gamma-ray bursts at lower energies. The first task is managed by a telescope (the LAT) that comprises a silicon tracker and a thallium-doped cesium iodine (CsI(TI)) calorimeter [57]. Basically the first system provides angular resolution and the second one provides accurate energy measurement. The energy resolution for gamma rays is of the order of 5%. The Fermi instrument was launched in June 2008. Being an efficient electromagnetic particle detector, Fermi LAT has been used in 2010 to measure the $e^+ + e^-$ flux [58]. These results are shown in Fig. 1.2. Unlike gamma-ray ones, these analyses extend up to the TeV range because electrons are an irreducible background for gamma rays above 300 GeV. Of course with no magnet it is not possible to separate electrons from positrons in the apparatus itself. However, a clever trick consists of taking advantage of the Earth geomagnetic field to separately measure electrons and positrons in a lower energy range [51]. These results are shown in Fig. 1.3.

HESS is a gamma-ray observatory in Namibia, comprising four telescopes since 2004 and a fifth one

12

since 2012 [59]. It uses the atmosphere as a calorimeter: high-energy particles entering the atmosphere produce secondary particles which in turn emit Cherenkov radiation. The telescopes are designed to capture that light. The threshold is of the order of 100 GeV and the detector allows detecting gamma rays up to about 100 TeV. The experimental technique will be discussed in more details in Chap. 2; what matters here is that the observatory has been used in 2008 and 2009 to observe cosmic-ray electrons and positrons between 400 GeV and 5 TeV [60, 61]. The results are displayed in Fig. 1.2.

The AMS-02 experiment is a magnetic spectrometer onboard the International Space Station. While taking data since May 2011, at the moment results are published only for the positron fraction [52]. We briefly describe the instrument here as it will provide most of the near future results. A AMS-01precursor flight has been performed with a limited detector in the space shuttle for ten days in 1998. AMS-02 is a comprehensive magnetic spectrometer including many sub-systems for particle identification. It includes a transition radiation detector, a time-of-flight detector, a silicon tracker, an imaging Cherenkov detector and an electromagnetic calorimeter. The acceptance is larger than that of PAMELA, the identification capabilities are higher and the calorimeter is bigger so that significant improvements in the measurements come from both statistics and precision.

|  | Location | Magnetic | Calorimetry | Geometrical acceptance | Energy resolution |
|---|---|---|---|---|---|
| PAMELA | space | yes ( $10^{-3}$ Tm$^2$) | lead-scintillator, 16.3 X$_0$ | $2.15 \times 10^{-3}$ m$^2$sr | 6% |
| ATIC | ballon | no | BGO, 18 X$_0$ | 0.1 m$^2$sr | 2% |
| Fermi | space | marginal | CsI(Ti), 8.6 X$_0$ | 2.8 m$^2$sr | 5%, $^{+5}_{-10}$% scale |
| HESS | ground | no | atmosphere, 27 X$_0$ | $\sim 10^2$ m$^2$sr (after cuts) | 15%, $\pm$15% scale |
| AMS-01 | space | yes (0.14 Tm$^2$) | tracker | 0.45 m$^2$sr | 10% |
| AMS-02 | space | yes (0.14 Tm$^2$) | tracker + lead-scintillator | 0.45 m$^2$sr | 1.5% to 10% |

Table 1.1: Main characteristics of the cosmic ray experiments relevant to this chapter. $X_0$ is the radiation length.

In Tab. 1.1, the main characteristics of these experiments are given. Note that these figures are only intended to give orders of magnitudes, as most of the performance of the detectors depend on the data taking conditions, analysis details and on the energy for instance. Also, these figures are not the only way to make comparisons between experiments, for example exposure times are very different from one another: PAMELA, Fermi and AMS-02 will take data continuously for years whereas ATIC and HESS have limited data taking times. Also, some systematic errors appear in ATIC and HESS due to the modeling of the atmosphere. All detectors but HESS are qualified with test beam data, partly explaining (together with the uncontrolled nature of the detection medium) why the energy resolution of HESS is poorer.

## 2.3   A word of caution concerning cosmic-ray data

The results that are discussed in this chapter have not been obtained with detectors of equal sensitivity and comparable systematics. For instance, Fermi is designed to observe gamma rays and the detector is not optimized for the measurement of electrons. In the case of ATIC, the background rejection is very dependent on the analysis for the above mentioned reasons. Obviously PAMELA and AMS-02 results should be considered as more reliable as the detectors were designed to perform these measurements. It is clear, at least in the case of electrons, that all the results cannot be simultaneously correct. This appeared as soon as the Fermi results came out, as they were incompatible with the ATIC results. Now both their results are being compared to AMS-02 measurements, and preliminary results seem to indicate that none of them correctly reproduced the right electron flux. Both the $\bar{p}$ flux and the electron flux from AMS-02 confirm a smooth featureless spectrum. On the other hand, most recent data point that the excess in the positron fraction is real. At the time when the ATIC results were published, the realness of the sharp features were already questioned. However, these results were a perfect test bed for the dark matter models that predict cosmic ray excesses.

## 2.4    Origin of cosmic radiation

Cosmic particles are expected to be accelerated in astrophysical environments, in a bottom-up way. Top-down scenarios are very unlikely for the bulk of cosmic rays as they involve exotic physics and potential acceleration sites exist and are observed. The best candidate acceleration sites are core collapse supernovae. One can see that quite easily with the energetics involved. The cosmic ray energy density is $\omega \sim 10^{-12}$ erg/cm$^3$. The power required to produce them in a volume $V$ and assuming they are confined during a time $\tau$ is $Q \simeq \omega V/\tau$. Now we know from cosmic ray spallation data that the mean cosmic ray path length is $x \sim 5$ g/cm$^2$. The spallation is caused by the Galactic gas which weighs about $M \sim 2 \times 10^{43}$ g, that is 10% of the total mass of the Galaxy. So one can re-write $x \simeq \rho \tau c$ with $\rho$ the gas density and $c$ the speed of light in vacuum, leading to $Q \sim \omega Mc/x$. All in all, to maintain this population of cosmic rays in the Galaxy a power of $Q \simeq 10^{41}$ erg/s is needed. Galactic supernovae happen at a rate of about 1 every 30 years, about 85% of those are core collapse of massive stars. Each explosion releases $\sim 10^{51}$ erg in ejecta, thus generating $\sim 10^{42}$ erg/s of power. It appears that Galactic cosmic rays can be produced by supernovae shocks if 10% of the energy released goes into acceleration of charged particles. Such an efficiency has been proven to be plausible (see for instance [62]). Recently the observation of supernova remnants such as the observation of RXJ-1713-3946 by HESS showed that electrons are accelerated at very-high energies within this object. Indeed gamma-rays are observed up to $\sim 50$ TeV, indicating the presence of charged particles typically ten times more energetic [63]. Concerning heavier species, observation of supernova remnants such as W44 [64] (Fig. **??**), IC 443 [65] and Tycho [66] provided evidence of acceleration of hadrons within these objects.
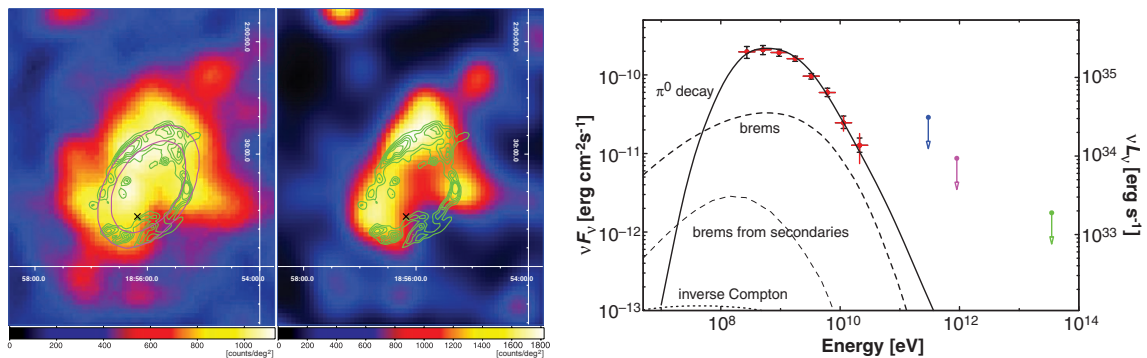


Figure 1.6: Morphology of the gamma-ray signal observed by Fermi in the direction of the supernova remnant W44 (left) and energy spectrum (right) [64]. The energy spectrum is well reproduced by pion decays, providing evidence for hadron acceleration.

The charged particles that are accelerated in the sources are called primary cosmic rays. After their production, they diffuse in the Galactic magnetic field during a certain time and eventually can be detected on Earth.

Cosmic rays diffuse in a region which has the same radial extension as the Milky Way, but thicker. This region can be parameterized with only a few parameters, as sketched in Fig. 1.7. The stars, the gas and the conventional cosmic ray sources are located in a thin disk of thickness $e$, of typically a few 100 pc. Particles diffuse in a halo that is about a factor of 100 times thicker. That region is where magnetic fields are present and is also affected by convective wind resulting from past explosions of supernovae in the thin disk. There are two ways to quantitatively describe the transport of cosmic rays in the Galaxy. The first one makes use of extensive numerical simulations and include all current knowledge about the inter-stellar medium, sources etc. This is the case of the GALPROP code [67], which is used in particular to compute the diffuse background for gamma-ray experiments. This approach has the advantage of including the most up-to-date astrophysical data but on the other hand is more an empirical representation of the condition in the Galaxy for propagation than a first-principles simulation. One drawback in particular is that it requires quite a large amount of computing time, in particular when one wants to test different

sets of propagation parameters. The method used in the papers that are summarized in this manuscript is different. It is based on semi-analytical computations in a diffusion model. It is clear that cosmic ray data are not precise enough to break the numerous degeneracies between the parameters used to feed numerical models. Following such a remark, one can look for the minimal set of parameters that enters in the prediction of cosmic ray at the Earth. Those parameters are basically the ones appearing in Fig. 1.7, plus the diffusion coefficient and its dependence on energy. These parameters are only phenomenological and this approach has significant advantages when it comes to estimating the uncertainty on the prediction of the background and signals, essentially because the computation times are significantly lower than for full numerical codes.
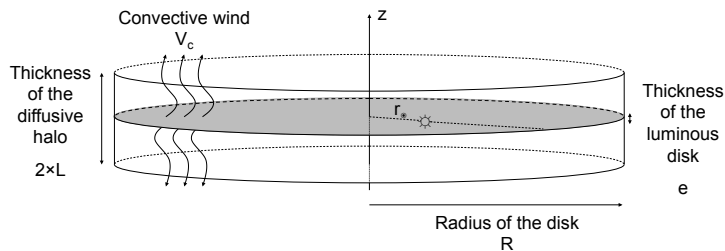


Figure 1.7: Boundary conditions for the diffusion of Galactic cosmic rays, and associated geometrical parameters.

The transport of particles in the Galaxy can be described by a diffusion-convection type equation, with energy redistribution terms and source terms (both for creation and disappearance of particles). The master equation is of the form

$$\frac{\partial}{\partial z} V_c \psi - K(E)\Delta\psi + \frac{\partial}{\partial E}\left[b(E)\psi - K_{\text{reac}}(E)\frac{\partial}{\partial E}\psi\right] = \mathcal{Q}(\vec{x}, E) \ , \tag{1.1}$$

where $\psi = \psi(\vec{x}, E)$ is the particle flux, $K$ is the diffusion coefficient, $b$ and $K_{reac}$ are the energy redistribution terms (respectively losses and re-acceleration), $V_c$ is a convective term accounting for past Galactic supernovae and $\mathcal{Q}$ is the source term. The latter includes the production in the source as well as interactions in the disk so that the source term for conventional sources is confined to the thin disk so $\mathcal{Q}$ can be taken as zero everywhere but at $z = 0$ ($\mathcal{Q} \propto \delta(\vec{z})$), where $z$ is the axis crossing the disk (see Fig. 1.7).

As mentioned earlier in this chapter, two types of cosmic rays are observed at the top of the atmosphere, namely primaries and secondaries. Primary cosmic rays are produced in the sources whereas secondary cosmic rays are produced by the first ones when crossing the disk during their trip. The most common example is Carbon nuclei that are produced during supernovae explosion and Boron which is not produced in supernovae (this is known from spectroscopy) but later in Carbon-Hydrogen collisions. The ratio B/C as measured at the Earth provides a measurement of the ratio of the diffusion coefficient to the thickness of the diffusive halo $K/L$. In a similar way, some isotopic ratios such as $^{10}$Be/$^9$Be give precious information on the confinement time. Indeed the unstable nuclei $^{10}$Be are predominantly produced in the sources and further decay into $^9$Be during the propagation. In that way the parameters of Eq. 1.1 as well as its boundary conditions are constrained from observations.

Depending on the particle species considered (here essentially antiprotons and positrons), some simplifications can be made to Eq. 1.1. For instance in the case of antiprotons, the energy loss term can be neglected, whereas it is dominant for electrons and positrons.

The observations of the electron features and the rise of the positron fraction, together with the absence of anomalies in the p̄ channel is a indication for a nearby primary source of leptons. Before further investigating the dark matter hypothesis, one should emphasize here that the electron features are

no longer seriously considered, and that there is no unconventional thing in having a nearby source of leptons. During the course of the studies described below, astrophysical explanations of these phenomena have always been preferred, as detailed in the last section of this chapter. The point was essentially to see how far the dark matter interpretation could be pushed, with the aim to reject the hypothesis in the end.

## 2.5 Now the stage is set...

Back in 2009 before PAMELA published its results, it was commonly admitted that antimatter particles were of secondary origin. That includes positrons and antiprotons, those being the only antimatter particles observed at the top of the atmosphere. In particular, the positron background with respect to which the excess shown in Fig. 1.3 appears is computed with the assumption that positrons are of secondary origin. The same is true for the antiproton background of Fig. 1.4 and 1.5. At that time there was hope that dark matter could appear in the cosmic ray data as a primary source of antimatter particles. The signature that was sought is typically a bump in the antimatter spectra, or a rise and fall in the antimatter to matter ratio. As exposed in the next section, this cutoff would correspond to the kinematic limit of particle production in dark matter annihilation at the mass of the dark matter particle. Actual observations went even beyond that hope. At the same time, PAMELA reported an excess in the positron fraction above 10 GeV ([50], Fig. 1.3) and ATIC published its results on a excess around 600 GeV in the $e^+ + e^-$ flux ([56], Fig. 1.2). Even though even at that time the results were questioned, these results were seen as a good pretext to reassess the possibility that cosmic ray channels could be used to search for dark matter. In addition, the antiproton results released by PAMELA did not display any anomaly ([53], Fig. 1.4 and Fig. 1.5). There was considerable excitement about these results in the community, as well as skepticism regarding the sharp features presented by ATIC. In particular a very good place to discuss them has been the TANGO in PARIS workshop organized in Paris (chairs: P. Brun and G. Bertone)[1], where specialists attended and three measurements were first presented there by Fermi, HESS and ATIC. Fermi reported the observation of a feature in the $e^+ + e^-$ spectrum ([58], Fig. 1.2) and then the same measurement was released by HESS ([60, 61], Fig. 1.2). A basic description of the problems raised there can be found in [68]. Although Fermi data seemed to exhibit a feature around the ATIC peak, HESS results seemed to disfavor the ATIC results on the total electron and positron flux. However note that ATIC has a much bigger calorimeter than Fermi and a better energy resolution. On the other hand, ATIC has a layer of atmosphere on top of it, which has to be taken into account and might induce systematic errors. In addition, the normalization of the HESS and Fermi fluxes are known to within about 10% so that the discrepancy may not be as significant as it looks. One thing clear was that not all measurement could be simultaneously correct and at that time AMS-02 results were eagerly awaited.

In the following, some pieces of work conducted after the release of these results are summarized. They were primarily intended to demonstrate that WIMP dark matter could not reasonably account for the observed excesses. The general idea is to prove it by contradiction: make the assumption that the signals are produced by dark matter, see where that leads and exhibit either some inconsistency or contradiction with some measurement. The path to this demonstration has been to re-assess the issue of backgrounds, in both antiproton and electron/positrons. Then the apparent incompatibility between the dark matter (DM) hypothesis and the comparison between hadronic and leptonic data allowed to constrain the parameters of the supposedly responsible dark matter candidate. As we shall see the results on antiprotons imply that dark matter annihilates either into some specific channels or in some specific locations in the Galaxy. These hypotheses have also been refuted, as shown in the following.

## 3 Primary cosmic rays from dark matter particle collisions

It is necessary here to give some details about dark matter annihilations and how the dark matter cosmic ray signal is estimated. Dark matter collisions in the Galaxy occur at a rate proportional to its density squared in a given location. In the annihilation process, standard model particles are assumed to be

---

[1]http://irfu.cea.fr/meetings/tangoinparis

produced with an equal amount of matter and antimatter. These standard model particles are elementary and their type depend on the interactions of the WIMP and depend on the other particles present in the model. For illustration purpose, one can consider a supersymmetric neutralino annihilating to quark-antiquark pairs through a s-channel production of a heavy Higgs particle, as sketched in Fig. 1.8.
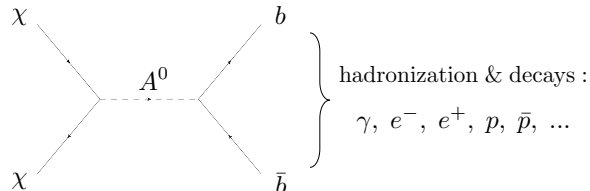


Figure 1.8: A example of an annihilation amplitude through a hypothetical $A^0$ boson decaying into a $b$ quark pair.

The hadronization and decays of the particles produced in the annihilation end up in stable particles such as photons, electrons and positrons, protons and antiprotons. Since the annihilation occurs almost at rest in the Galaxy reference frame, the energy of those particles is at most equal to the mass of the dark matter particle, defining the aforementioned kinematic limit of primary particle production in dark matter annihilation processes. Any WIMP model can be described phenomenologically through a few parameters which are the WIMP mass $m_\chi$, its annihilation cross-section $\sigma v$ and the branching ratios for the different final states. Different final states yield different efficiencies in the production of what will later be primary cosmic rays. For instance, the $b\bar{b}$ channel will often be considered as a conservative channel. Indeed, because of the larger number of intermediate particles between the annihilation and the production of stable particles, the energy is handed out between more particles during the process and $b\bar{b}$ produce soft spectra. Because backgrounds fall rapidly with energy, a general rule for a signal to be visible is that the harder the better. Compared to other channels, $b\bar{b}$ leads to softer spectra. Another obvious example of the importance of final states in the phenomenology at stake here is given by studying annihilations into lepton pairs. In that specific case the antiproton yield is null. This will be discussed later in this chapter. In the following, no specific particle physics model is usually specified because one can retrieve any WIMP model from final state combinations.

If charged, the primary particles being produced the way described above, they will propagate into the diffusive halo of the Milky Way. The corresponding source term to fill in Eq. 1.1 is the following:

$$\mathcal{Q}_{\mathrm{DM}}(\vec{x}, E) \;\; = \;\; \frac{\sigma v}{m_\chi^2} \times \frac{\rho^2(\vec{x})}{2} \times \sum_i f_i \times \frac{dN_i}{dE} \;\; , \qquad (1.2)$$

where $f_i$ is the branching fraction into some final state $i$ (a pair of standard model particles), $dN/dE$ is the energy repartition of the considered primary (stable) particles for that specific final state, $m_\chi$ is the mass of the dark matter particle, and $\rho$ is the dark matter density. The other terms have been previously defined. Contrary to the conventional source term, $\mathcal{Q}_{\mathrm{DM}}$ is not restricted to the luminous disk. Instead the dark matter density $\rho$ is spherical and follows a profile which is concentrated at the center and has a radius of the order of 100 kpc. The density close to the Sun, about 8 kpc from the Galactic center is $\rho_\odot \sim 0.3$ GeV/cm$^3$. For canonical 500 GeV WIMPs, this corresponds approximatively to 600 particles per cubic meter or one particle per cube of 20 cm sides. These signals are typically computed using sophisticated numerical codes such as micrOMEGAs, described in [44].

An important point for what follows is the fact that the annihilation rate scales as the square of the dark matter density. This is basically due to the fact that WIMP pairs annihilate, so for a population of $N$ WIMPs in a given volume $N(N-1)/2$ pairs can be formed. As a consequence, $\mathcal{Q}_{\mathrm{DM}}$ as given is Eq. 1.2 can be seen as an average value. If the dark matter distribution is not homogeneous, it could be that $\langle \rho^2 \rangle > \langle \rho \rangle^2$, leading to the so-called boost factors that are often invoked in dark matter searches. Other kinds of boost factors can come from particle physics effects that increase the annihilation cross-section,

as for example the Sommerfeld effect [69, 70]. Most of the work presented in this chapter deals with constraining the possible magnitude of boost factors.

## 4 Confrontation of leptonic and hadronic data

To estimate the level of exotic production that the data can accommodate in a given channel, the conventional signal has to be correctly estimated. In the case of antiprotons, the conventional background for dark matter searches consists of secondary antiprotons. In [43], the antiproton conventional signal is calculated with improved input data compared to previous estimates (*e.g.* [71]). Antiprotons are produced by the spallation of cosmic ray proton and Helium, the contribution of heavier nuclei being negligible [72]. A good description of the p and He interstellar fluxes is mandatory to correctly provide the $\bar{p}/p$ ratio in the 0.1 GeV to 100 GeV range. These fluxes are parameterized following data from AMS-01, BESS98 and BESS-TeV. The above described diffusion model is used to compute the fluxes. The propagation parameters are fixed from the B/C data as in [73]: $L = 4$ kpc is the half thickness of the halo, the diffusion coefficient is $K(E) = K_0 \beta \mathcal{R}^\delta$ with $K_0 = 0.0112$ kpc$^2$/Myr, $\delta = 0.7$ and $V_c = 12$ km/s, $\beta$ being the Lorentz factor and $\mathcal{R}$ the rigidity. The reacceleration term is $K_{\mathrm{reac}}(E) = 2/9 E^2 \beta^4 V_a^2 / K(E)$ with $V_a = 52.9$ km/s being the speed of the scatterers responsible for the energetic diffusion (magnetic field inhomogeneities). One great advantage of the semi-analytical approach describe here is that is allows accurate computations of the theoretical uncertainties on the conventional signal.

Because Eq. 1.1 can be easily solved for different parameters, the errors on the inputs such as p and He fluxes, cross-sections and propagation parameters from B/C data can be propagated to estimate the error on the standard $\bar{p}$ flux. This is illustrated in Fig. 1.9. On the left panel of Fig. 1.9 the antiproton flux is presented together with the uncertainty band related to cross-section productions only. The data represent interstellar fluxes, *i.e.* they have been demodulated, meaning the effect of solar winds have been taken into account. In the right panel, along with the demodulated $\bar{p}/p$ data, the curves bounding the propagation uncertainty on the $\bar{p}$ calculation are shown. Note that at the time of that study, the $\bar{p}$ measurement from PAMELA was not available, only the ratio was. Including the $\bar{p}$ results from PAMELA does not change the conclusions.
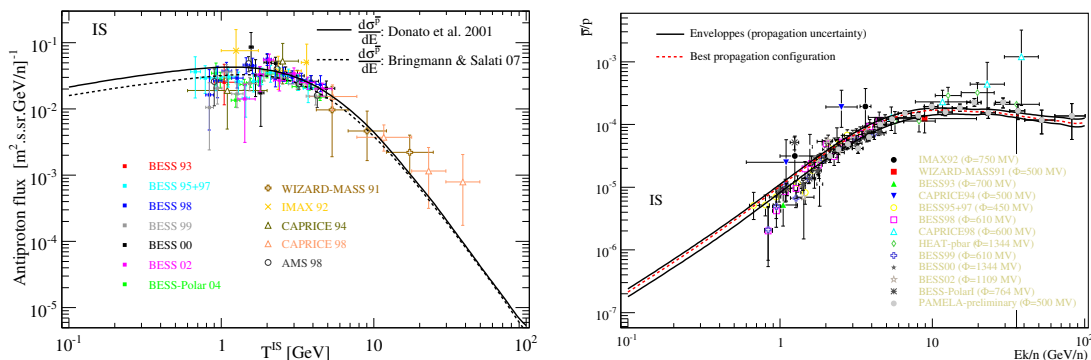


Figure 1.9: Left: interstellar $\bar{p}$ flux for the B/C best fit parameters and two parameterizations of the production cross-sections. Right: propagation uncertainty envelopes on the interstellar $\bar{p}/p$ ratio for the same cross-sections as in the left panel. Figures from [43].

The precise measurement of the $\bar{p}/p$ ratio from PAMELA and the possibility to compute the uncertainty on the conventional signal allowed to derive limits on a possible exotic component. Focusing on the high-energy bins where solar modulation does not play a role [74], one can assume the presence of an additional component of antiprotons produced by annihilations of WIMPs filling the dark halo. Their distribution is taken as a cored isothermal sphere with a local density $\rho_\odot = 0.3$ GeV/cm$^3$. The annihilation cross-section is taken as $\sigma v = 3 \times 10^{-26}$ cm$^3$/s with an annihilation branching ratio being 100% $b\bar{b}$. Actually, it turns

out that the propagated p̄ flux is only very mildly dependent on the annihilation channel and the DM distribution, so that the assumptions can be considered valid for a generic WIMP except for a rough rescaling factor. Propagation is treated in the same way as for the secondary component. As a reference case, the best fit transport parameters mentioned above are used (in that case of primary production, the uncertainty inferred on the propagated flux is larger than for the conventional one, the prediction spans over about one order of magnitude). The calculated p̄ flux is added to the secondary component and the total flux is compared to each PAMELA high energy bin: 15.3 GeV, 19.5 GeV, 25.9 GeV, 37.3 GeV and 61.2 GeV. The most conservative set of cross-sections (leading to the short-dashed curve on the left panel of Fig. 1.9) is used. Then the factor by which the DM flux could be enhanced without exceeding experimental data (at $1\sigma$) is derived for each energy bin. The maximum allowed boost factor is plotted in Fig. 1.10 as a function of the WIMP mass: it cannot exceed 6-20-40 for $m_\chi = 100 - 500 - 1000$ GeV respectively.
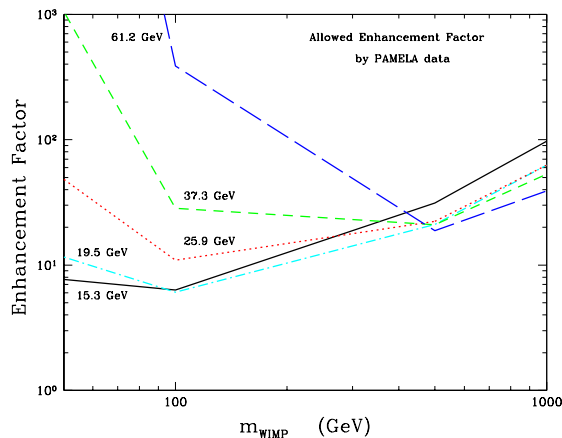


Figure 1.10: Maximum allowed enhancement factors allowed by the PAMELA p̄/p ratio data, as a function of the WIMP mass. Each colored curve corresponds to a bin in the PAMELA p̄/p ratio. Figure from [43].

The above conclusions have important consequences on the explanation of the positron data based on the annihilation of DM particles in the halo. As shown in [43, 75], the positron fraction suffers from large uncertainties related, for instance, to the poorly determined electron spectral index above 10 GeV. The following study assumes an electron index of 3.44, leading to the positron fraction displayed in Fig. 1.11 (long-dashed curve featuring a low background case). It has been shown later in [47] that the measured electron spectrum is harder, which has the consequence of lowering even more the positron fraction at high energy, therefore the conclusions of this section should now be stronger. With a typical thermal cross section, WIMPs do not produce enough positrons to reproduce the observed increase. As we shall see in the next sections, boost factors from DM clumps are unlikely to enhance the signal by more than a factor of about 10. A plausible mechanism to enhance the DM annihilation cross-section is the Sommerfeld effect, for which a heavy DM species is a prerequisite. A generic 1 TeV WIMP is then considered, with annihilation into $W^\pm$ pairs (to provide a harder injection spectrum). If the thermal cross-section is boosted by a factor of 400, one obtains the solid line in Fig. 1.11 that better accommodates the data.

Although an annihilation cross-section of $1.2 \times 10^{-23}$ cm$^3$/s is possible should non-perturbative effects be invoked, the consequences on antiprotons are drastic. The red solid line shown in Fig. 1.12 features an unacceptable distortion of the p̄ spectrum. The DM positron signal cannot be enhanced without playing havoc with the antiproton measurements.

At this point of the story, it is clear that the first attempts to simultaneously fit hadronic and leptonic data lead to inconsistencies. The DM hypothesis is weakened but not dead, it is still possible that DM annihilations lead to negligible p̄ flux, and significant e$^+$/e$^-$. The first possibility is that DM annihilation simply do not produce antiprotons. The above results motivated the so-called leptophilic DM models, in
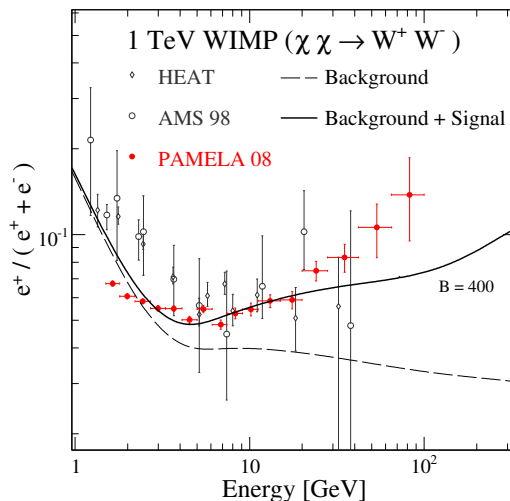
Figure 1.11: Dark matter signal in the positron fraction channel from a 1 TeV WIMP (solid line) compared to the PAMELA measurements. The dashed line represent the expected conventional signal from secondary cosmic rays. Figure from [43].

which DM annihilate into leptons only. This may be the case for instance if DM annihilate through a new particle that do not couple to quarks. As previously shown even in that case the annihilation rate required to reproduce the rise in the positron fraction has to be enhanced in some way with respect to the thermal cross-section. The second possibility is that the enhancement comes from the inhomogeneity of the spatial DM distribution. Those two hypotheses are discussed in the two next sections and a short review of these results can be found in [76].

## 5  Enhancement of dark matter signals from particle physics effects

Compared to the thermal cross section, the enhancement required to explain the cosmic lepton data is more than $10^3$. This has implications for observations with other messengers. For instance, if leptons are produced at such a rate in the Galactic center region (or any other dense region), they might produce observable effects through the photons they subsequently emit. Those photons can be gamma rays of energy of order $m_\chi$ or radio emission from synchrotron emission. Many studies gave constraints on the DM models that fit the leptonic excesses, a nice and comprehensive one can be found in [77]. An example of results that appear in [77] is displayed in Fig. 1.13. Here the green band is the region that is favored by PAMELA positron data, and the red region is what remains if one wants to simultaneously fit the ATIC excess. The different lines correspond to exclusions that one can place based on different observations. For most cases, the leptophilic model is excluded.

Other strategies include for instance constraints based on the extragalactic gamma-ray background (from annihilations since the formation of halos), see [78], and possible distortions of the cosmic microwave background (CMB) anisotropy spectrum [79]. Both these studies show that if DM particles produce leptons at the rate required for explaining PAMELA and ATIC, predictions are in conflict with observations.
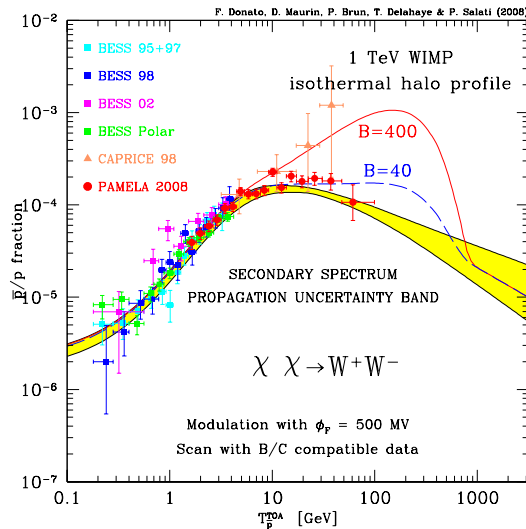
Figure 1.12: Antiproton DM signal from 1 TeV WIMP and boost factors of 40 and 400 (dashed blue curve and solid red curve respectively. The yellow band represents the expected level of secondary-induced conventional signal and its theoretical uncertainty. Figure from [43].

# 6 Enhancement of WIMP signals from dark matter substructures

A remaining possibility so far is that of the enhancement of the signal by a local over-density of DM. In the following, leptophilic types of models are being considered but in principle the over-density scenario could evade the antiproton constraints if the associated yield is not too large. In that case, because of the different propagation properties of electrons and antiprotons, the antiproton paradox can be avoided. Indeed antiprotons normally do not lose energy while they propagate. As a consequence, they diffuse in the Galaxy for a long enough time to explore a large fraction of the diffusive halo. For electrons though, it is the contrary, they quickly lose energy when they propagate. Thus the observation of a high-energy electron means that is has not been produced very far away. Actually the further they go, the more energy they lose. All in all this means that antiprotons and electrons do not dilute similarly, and that electrons are more local species. These energy and species dependences of the boost factors were pointed out in [80, 81, 82].

In the present section, the possibility that a DM clump contributes substantially to the lepton anomalies is studied, following the line of [45]. The distance of the clump $D$ and its luminosity $L$ are adjusted to the data. Then, the clump parameters are compared to the cosmological N-body simulation *Via Lactea II* to compute the odds to find such a configuration in the Milky Way. The possibility that a single nearby DM clump contributes substantially to the lepton anomalies had previously been studied, *e.g.* in [83, 84, 85], but the question of the probability of the subhalo configuration had never been addressed before.

The lepton density $\psi = dn/dE$ is related to its source $q$ through the stationary cosmic ray diffusion equation described before. Lepton propagation throughout the diffusive halo is dominated by space diffusion and energy losses via synchrotron emission and inverse Compton scattering on the CMB and stellar light. The propagation parameters are those providing the best-fit to the B/C ratio data. The positron flux at the Earth $\phi_{e^+} = \phi_{e^+}^{sec} + \phi_{e^+}^{s} + \phi_{e^+}^{c}$ results here from three contributions. The astrophysical background $\phi_{e^+}^{sec}$ is provided by the secondary species produced by primary cosmic rays impinging on the interstellar

Figure 1.13: Multi-wavelength constraints on the DM particle parameters that are required to reproduce the cosmic lepton features. The green regions are the best-fit regions for the PAMELA signal, the red area is excluded by radio observations of the Galactic center and the blue areas are exclusion from gamma-ray observations. Figure from [77].

material and is computed as in [86]. The smooth DM halo contributes to the source term

$$q_{\mathrm{DM}}^{\mathrm{s}}(\vec{x}, E) \;=\; \frac{1}{2} \, \langle \sigma v \rangle \left\{ \frac{\rho_{\mathrm{s}}(\vec{x})}{m_\chi} \right\}^2 f(E) \;\;, \tag{1.3}$$

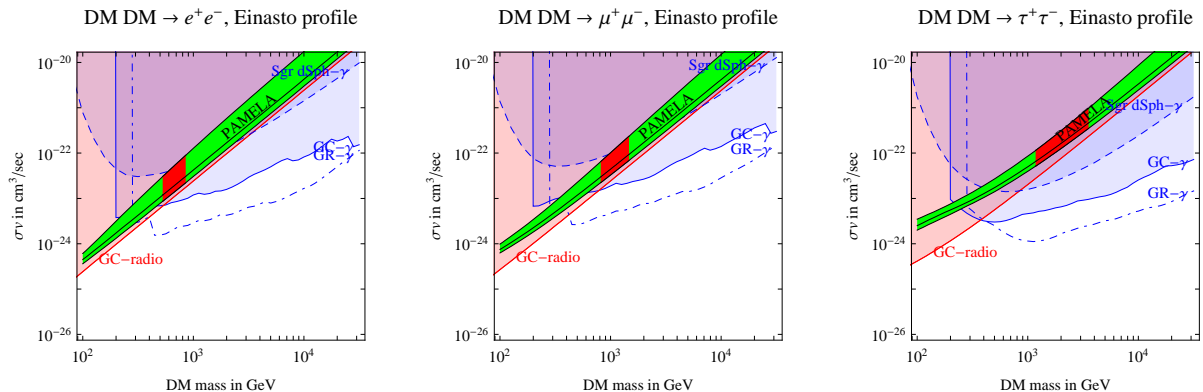where $f(E)$ is the energy spectrum of the positrons created in the annihilation process. The Galactic DM halo density $\rho_{\mathrm{s}}$ is borrowed from the results of the *Via Lactea II* simulation, with a spherical profile featuring an inner (outer) logarithmic slope of -1.24 (-3) and a 28.1 kpc scale parameter. The local density $\rho_\odot$ is equal to 0.37 GeV cm$^{-3}$. The galactocentric distance of the Earth is $r_\odot = 8.5$ kpc. Finally, the contribution of a nearby clump located at $\vec{x}_c$ can be expressed as

$$q_{\mathrm{DM}}^{\mathrm{c}}(\vec{x}, E) \;=\; \frac{1}{2} \, \langle \sigma v \rangle \, \frac{L}{m_\chi^2} \, \delta^3(\vec{x} - \vec{x}_c) \, f(E) \;\;, \tag{1.4}$$

where $L = \int_{\mathrm{clump}} \rho_c^2(\vec{x}) \, \mathrm{d}^3 \vec{x}$ is defined as the subhalo luminosity. Furthermore, as clumps are treated here as point-like objects (the scale radii of the clumps are always much smaller than the typical lepton diffusion length), the source terms $q_{\mathrm{DM}}^{\mathrm{s}}$ and $q_{\mathrm{DM}}^{\mathrm{c}}$ add up directly to yield the total DM lepton signal.

The annihilation cross-section of the DM particles under scrutiny is set equal to the thermal value $\sigma v = 3 \times 10^{-26}$ cm$^3$ s$^{-1}$ and 100 GeV and 1 TeV WIMPs are considered as benchmark cases. Finally, inspired by previously described studies, leptophilic species are considered with production of either a pure $e^+e^-$ annihilation final state (positronic line) or an equal production of charged leptons $e^\pm + \mu^\pm + \tau^\pm$. As mentioned before, a case for both scenarios can be made from the model-building perspective. Models featuring pure $b\bar{b}$ or $W^+W^-$ annihilation final state have been studied as well but are disregared since the required clump configurations are extremely unlikely ($p < 10^{-6}$).

The particle physics framework being set, fits to the PAMELA, ATIC and Fermi data are performed, which include a smooth DM component plus a contribution from a DM subhalo whose luminosity $L$ and distance $D$ are free parameters. For PAMELA, the positron fraction $\phi_{e^+}/\phi_{e^+} + \phi_{e^-}$ is computed, where $\phi_{e^-}$ is the observed cosmic ray electron flux measured by AMS [87] and HEAT [48] and parameterized in [88]. Again, better data are now available but the conclusions remain unchanged. Regarding from ATIC and Fermi, the total lepton flux $\phi_{e^+} + \phi_{e^-}$ is derived, assuming that the electron background $\phi_{e^-}^{\mathrm{back}}$ is given at high energy by a fit in [88] and adding a DM contribution equal to $\phi_{e^+}^{\mathrm{s}} + \phi_{e^+}^{\mathrm{c}}$. Solar modulation is implemented using the force field approximation [89] with a Fisk potential of 300 MV.

Fig. 1.14 illustrates the fit results in the case of $e^\pm$ direct production. For PAMELA, both 100 GeV and 1 TeV WIMPs can accommodate the excess. As far as ATIC is concerned, the observed feature can
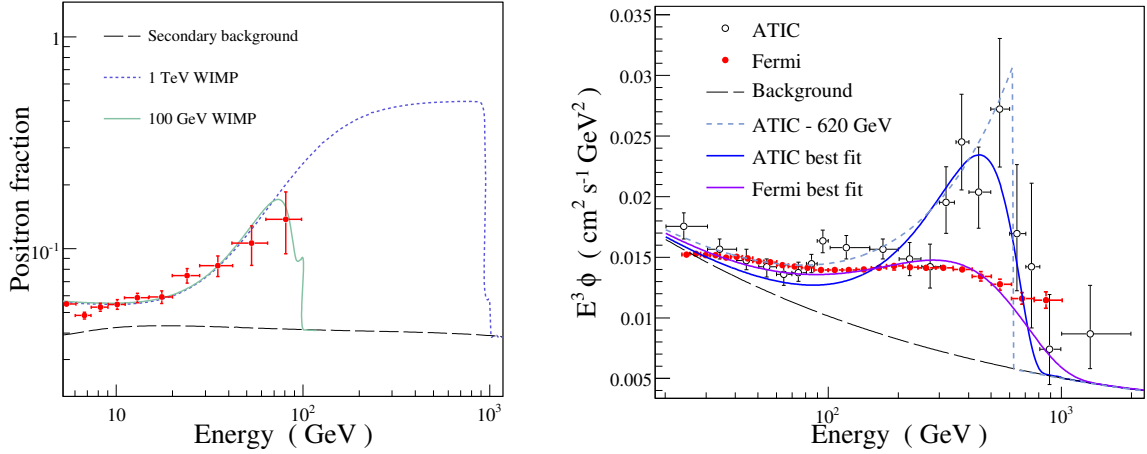
Figure 1.14: Best fits to the PAMELA data in the case of a positronic line (see the $e^+/e^-$ row of Tab. 1.2) (left panel) and fits to the ATIC and Fermi data (right panel). In both panel the dashed line is the expected conventional signal from secondary cosmic rays. Figure from [45].

be reproduced in the case of a 1 TeV WIMP assuming a DM clump with luminosity $2.98 \times 10^9$ $M_\odot^2$ $pc^{-3}$ lying at a distance of 1.52 kpc from the Earth. When the ATIC excess was reported, it was interpreted as evidence for a 620 GeV Kaluza-Klein species. That result holds for the case of a positronic line. In that case, no satisfying adjustment can be found without adding a nearby subhalo. If WIMP annihilations take place only inside a smooth Galactic DM distribution, the required cross-section is smaller than $\sim 10^{-24}$ $cm^3$ $s^{-1}$, i.e. two orders of magnitude above the canonical value. As we shall see in the following, the fit to the Fermi data points towards an incredibly bright clump. Indeed, the feature seen by Fermi is not very peaked and quite spread out and requires, because of propagation effects, both a very large mass for the DM particle and a quite far away clump. All parameters found in the best-fit cases are displayed in Tab. 1.2.

| | PAMELA | | ATIC | Fermi |
|---|---|---|---|---|
| $m_\chi$ (GeV) | 100 | 1 000 | 1 000 | 2500 |
| $e^+/e^-$ | $1.22 - 1.07 \cdot 10^7$ | $0.78 - 3.56 \cdot 10^9$ | $1.52 - 2.98 \cdot 10^9$ | $2.68 - 5.53 \cdot 10^{10}$ |
| $e^\pm + \mu^\pm + \tau^\pm$ | $0.44 - 2.51 \cdot 10^7$ | $0.27 - 9.84 \cdot 10^9$ | $0.25 - 8.78 \cdot 10^9$ | $2.81 - 2.17 \cdot 10^{11}$ |

Table 1.2: Best fit values of the $(D; L)$ couple in units of $(kpc; M_\odot^2 pc^{-3})$ for various DM particle masses and annihilation channels.

DM annihilations within these clumps should not only produce charged leptons but also gamma rays. A small $\bar{p}$ production might be possible as well. To estimate the authorized $\bar{p}$ yield, a small branching ratio $F_{\bar{p}}$ into antiprotons either through the $b\bar{b}$ channel when the WIMP is light or through the $W^+W^-$ channel for a 1 TeV species is considered.

The total antiproton flux $\phi_{\bar{p}} = \phi_{\bar{p}}^{sec} + \phi_{\bar{p}}^s + \phi_{\bar{p}}^c$ is computed with the same cosmic ray and DM models as for positrons. Requiring that the resulting signal does not exceed the PAMELA antiproton data [53] by more than $1\sigma$, upper limits on $F_{\bar{p}}$ are derived and are featured in Tab. 1.3. Antiprotons are not forbidden if they are produced together with leptons but their abundance in the annihilation debris is sufficiently suppressed.

Tab. 1.3 also presents conservative estimates for the detectability of the gamma-ray emission from the lepton-fitting clumps of Tab. 1.2. The gamma-ray flux at the Earth is expressed in units of Fermi $5\sigma$ sensitivity over 1 year of data taking for high-latitude, point-like sources [57]. In all cases the LAT would

have detected the clumps in their first catalog. Notice that one of the leptophilic 1 TeV PAMELA cases has a very large flux of $1.11 \times 10^{-6}$ $\gamma$ cm$^{-2}$ s$^{-1}$ and is already of the larger than the EGRET point-source sensitivity of $2 \times 10^{-7}$ $\gamma$ cm$^{-2}$ s$^{-1}$ [90], and should have been already detected by EGRET before Fermi.

| | | PAMELA | | ATIC |
|---|---|---|---|---|
| | $m_\chi$ (GeV) | 100 | 1 000 | 1 000 |
| Antiprotons | $e^+/e^-$ | 0.23 (b$\bar{\text{b}}$) | 0.066 (W$^+$W$^-$) | 0.13 (W$^+$W$^-$) |
| | $e^\pm + \mu^\pm + \tau^\pm$ | 0.063 (bb) | 0.0074 (W$^+$W$^-$) | 0.055 (W$^+$W$^-$) |
| Gamma rays | $e^+/e^-$ | 0.95 | 12.7 | 3.9 |
| | $e^\pm + \mu^\pm + \tau^\pm$ | 28.6 | 370 | 12.9 |

Table 1.3: Upper rows : maximal values of the branching ratio $F_{\bar{p}}$ of WIMP annihilation into b$\bar{\text{b}}$ (100 GeV) or W$^+$W$^-$ (1 TeV) pairs allowed by the PAMELA antiproton data [53]. Lower rows : the clump gamma-ray flux above 0.1 GeV is expressed in units of $3 \times 10^{-9}$ $\gamma$ cm$^{-2}$ s$^{-1}$ [57].

Fig. 1.15 shows the probability of having the nearest DM clump of luminosity $L$ within a distance $D$ from the Sun. The abundance of nearby clumps and their properties are taken directly from the *Via Lactea II* (VL-II) simulation [91]. The high performance of the simulation and associated numerical methods allow VL-II to resolve subhalos even in the dense environment near the solar circle. The mean separation of subhalos with peak circular velocities $V_{\max} > 5$ km/s is 9.6 kpc and their luminosities are

$$L = 7.91 \times 10^5 \text{ M}_\odot^2 \text{ pc}^{-3} \left(\frac{V_{\max}}{5 \text{ km/s}}\right)^3 \sqrt{\frac{c_V}{2 \times 10^6}} \ , \tag{1.5}$$

where $c_V$ is a dimensionless number describing the concentration of the subhalo, as defined in [91]. For comparison, the smooth VL-II main halo has a luminosity of $L = 3.4 \times 10^9$ M$_\odot^2$ pc$^{-3}$, while the total luminosity (*i.e.* including subhalos) is about 10 times higher [91]. At a given $V_{\max}$ we assume a log-normal distribution of luminosities with factor of 3 scatter, motivated by the substantial variance in the concentration $c_V$ found in the simulation in nearby subhalos [91]. In Fig. 1.15, the bold line gives the median distances calculated from a random sample of observer positions. The long-dashed, dashed and doted lines stand for the 10$^{\text{th}}$,1$^{\text{st}}$ and 0.1$^{\text{st}}$ percentiles, respectively. The points represent the locations of the best fits to the data in the $L - D$ plane while the surrounding contours display the 1$\sigma$ excursions around these best fit values (as well as 3$\sigma$ for ATIC and Fermi). It is found that clumps fitting the PAMELA, ATIC and Fermi data are far from the natural values indicated by VL-II. The most probable configuration is the PAMELA fit with a 100 GeV WIMP, which is inside the *Via Lactea* 3$\sigma$ contours. That configuration is found in 0.37% of all realizations. However, this scenario cannot accommodate ATIC data because $m_\chi$ is too small. Increasing the mass of the DM particle requires even brighter and less likely clumps at $D \simeq 1$ kpc. As illustrated by the different PAMELA fit contours of Fig. 1.15, the parameter degeneracy also increases as $m_\chi$ gets higher.

Basically, the PAMELA measurements do not constraint the spectral shape of the signal above 100 GeV and leave more lever-arm to the fits when WIMPs are heavy. For TeV WIMPs, there are clump properties which reproduce both the ATIC and PAMELA excesses (see Fig.1.15), and such a source would have been well within the reach of Fermi (Tab. 1.3). However it is very unlikely to exist in a standard CDM halo (probability $p \simeq 3 \times 10^{-5}$). A DM spike or a higher cross section would be required to get the needed luminosity from a smaller, more probable nearby subhalo. Concerning the best fit to the Fermi electron data, it points at the need for a clump that should be brighter than the whole Milky Way. We can therefore safely associate a zero probability to this configuration. Note finally that the Via Lactea II contours extrapolate at lower values of the distance and clump luminosity. The corresponding clumps are not of particular interest for this particular study as for mean Via Lactea clumps, the natural luminosity decreases faster than what we gain from placing the clump closer.

The investigation of the lepton anomalies in the presence of a nearby DM clump has finally led to discover a subtle interplay between the injection spectrum, the position of the substructure and the signal at the Earth. In particular, the commonly used criterion of a sharp cut-off as a smoking-gun signature of DM models producing leptons (*e.g.* in Universal Extra Dimension Kaluza-Klein models [92]) is misleading
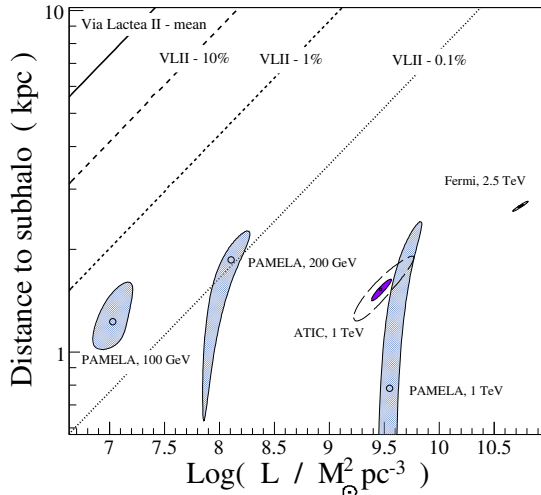
Figure 1.15: Best fit results in a clump luminosity-distance plane for different configurations, together with probabilities inferred from *Via Lactea II* results. Figure from [45].

if most of the DM signal stems from a highly clumpy halo. At TeV energies, leptons detected at the Earth are produced within a distance of $\sim 1$ kpc and a clump becomes less visible if it lies outside that region. The opposite case is also possible since one can obtain very peaked lepton spectra even with a soft injection spectrum, as long as the nearest clump is close enough. In general, as far as spectral shapes are concerned, it is important to bear in mind the spectral distortions induced by cosmic ray propagation.

As an illustration, Fig. 1.16 shows how the signal from DM can exhibit a double-bump feature if, in addition to the contribution from a smooth DM halo, two nearby clumps are taken into account (solid light-colored line). In this example, the subhalos lie at a distance of 0.9 and 4.3 kpc from the Earth and their luminosities are of order $10^8$ and $10^{10}$ $M_\odot^2$ pc$^{-3}$, respectively. Indeed, a specificity of lepton propagation is that regardless of the overall normalization, a feature observed at energy $E$ can always be produced by a source at distance $D$ with an injection energy $E_S$ as long as $D^2 \propto E^{-0.3} - E_S^{-0.3}$ [2]. However, without additional enhancements, having such bright nearby clumps is practically ruled out and we only use them here for pedagogical purpose. CDM subhalos with $L > 10^8$ $M_\odot^2$pc$^{-3}$ have $V_{\max} > 25$ km/s and host relatively bright dwarf galaxies [93]. If such dwarf galaxies existed nearby, they would have been observed. As for the short-dashed curve in Fig. 1.16, the sharp edge at 800 GeV is associated with a strong local DM annihilation and is produced by the VL-II smooth halo whereas the bump at $\sim 100$ GeV comes from a single nearby clump located at 3.2 kpc. The cross section has been increased up to a value of $10^{-23}$ cm$^3$ s$^{-1}$. This case seems somewhat more probable than the 2-clumps configuration. These examples illustrate how tricky boost factors are. Shifting upwards the DM cosmic ray fluxes turns out to be wrong especially in the light of the effects introduced by propagation.

As a final remark to this section, we point out that all the fitted spectra would have been obtained with significantly less luminous subhalos should the annihilation cross-section be directly enhanced. If the Sommerfeld effect [70] is at play, the enhancement of the cross section could be inversely proportional to the relative velocity (or some power of) in the collision. In that scenario, the signal from small clumps is further enhanced with respect to the contribution from larger substructures [94] since the velocity dispersion of DM particles decreases with the mass of the host subhalo. The blue contours of Fig. 1.15 are shifted towards smaller values of $L$ and get closer to the mean predictions of the VL-II simulation, with a much larger probability of occurrence (by simply assuming $L \to L \times c/V_{\max}$, the probability associated to the ATIC best fit case increases from $p \simeq 3 \times 10^{-5}$ to 14 percent!). Due to the lack of data at the time, we had to make some assumptions on the electron spectrum and propagation parameters. Therefore new data may lead to different confidence levels for the exclusions, but the conclusions should remain.

The main conclusion is that the different features that are observed in antimatter cosmic ray spectra are

---

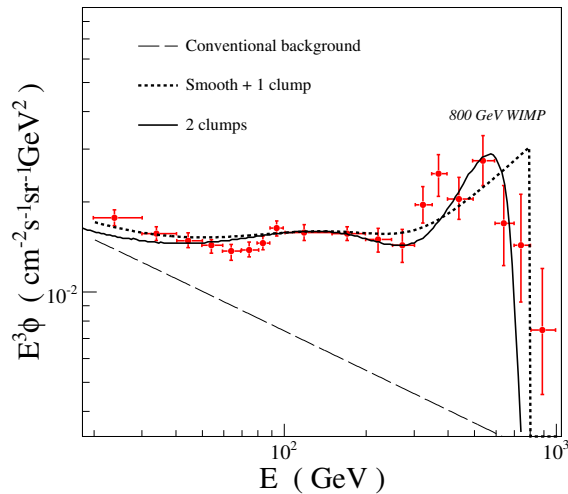[2]The 0.3 exponent depends on the cosmic ray propagation model.

Figure 1.16: Electron-positron spectra resulting from one (dotted line) or two (solid line) nearby subhalos. In the latter case, a 620 GeV DM species with thermal annihilation cross-section is considered. The dashed line is the expected conventional signal from secondary cosmic rays, the dotted line and solid line represent signals from one and two clumps respectively. Figure from [45].

most likely not due to dark matter annihilations. Decaying dark matter have been studied by independent groups [95, 96, 97], and they conclude on very restrictive regions for the DM parameters as well. The observed features are nonetheless impossible to reproduce without a primary component, which has to be something else than dark matter.

# 7   Conventional interpretations

The reason why DM has been a widely studied solution to the cosmic ray lepton puzzle is because it was previously thought to be a potential channel for discovery. However simpler explanations exist for the excesses, that been proposed even before they have been observed with precision (see for instance [98, 99, 100, 101]). It is actually suspected that a nearby source of electron and positrons significantly contributes to the observed flux. Some possibilities are briefly summarized in [102]. For conventional sources, one can consider two types: electromagnetic sources and non-electromagnetic sources. In the first case, pairs are produced via purely electromagnetic processes. These sources can be *e.g.* pulsars or gamma-ray binaries. For such sources, there could be counterparts in gamma rays. The second class of sources implies hadronic processes as well, it can be any type of astrophysical shock, like in supernova remnants. In that case, counterparts are expected in gamma rays and possibly in the antiproton channel as well.

Pulsars are good candidates for being the nearby source responsible for the excesses. They are rotating and strongly magnetized neutron star, within which $e^{\pm}$ pairs can be created in magnetic fields or by high-energy photon collisions. TeV-scale leptons can be produced and accelerated in the environment of the neutron star and released in the interstellar medium provided the matter is diluted enough. For that latter reason, mature pulsars located less than a few kpc away, such as Geminga, Loop I, Monogem (and others) are excellent candidates. All the measurements can be well fitted by adding pulsars to the conventional secondary flux. Fig 1.17 shows an example of such pulsar signals. It is provided by the Fermi collaboration [103] and shows the expected contributions to the fluxes from nearby mature pulsars. However, there is yet no obvious unique candidate as there are still free parameters in the models. In its first year of data taking, the Fermi satellite discovered numerous new pulsars showing that these objects seem to be ubiquitous in our Galactic environment. A discussion on production mechanisms of $e^{\pm}$ pairs

in pulsars can be found in [104]. However, in that case it is probable that no counterpart in gamma ray is observable, the reason being that the emission of photons and the acceleration of charged particles occur on very different time scales.
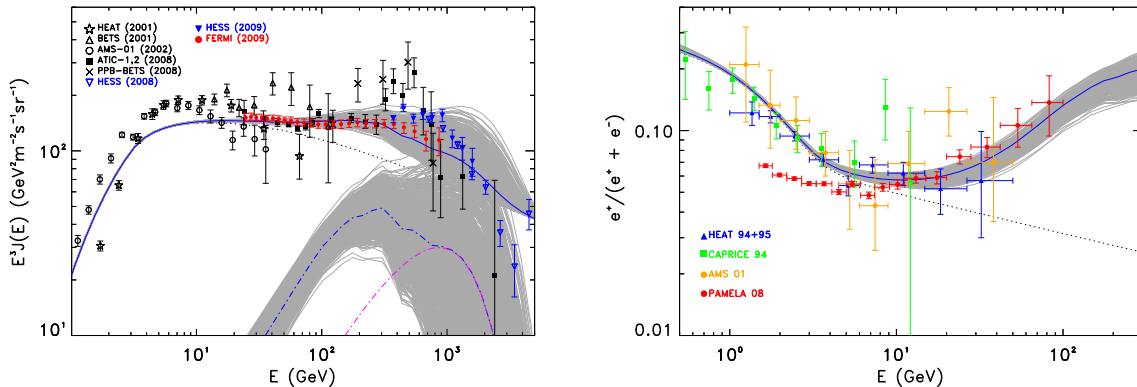


Figure 1.17: Left panel: $e^+ + e^-$ data, together with a secondary prediction (dotted line) to which are added expected contributions from all pulsars closer than 3 kpc (numerous grey lines). The purple dashed line represents the contribution of Monogem pulsar as an illustration. Right panel: same for the positron ratio. Figures from [103].

Concerning supernova remnants, another possibility would be that secondary particles directly produced at the source have not been previously accounted for properly. In the standard picture, remnant material from the exploding star constitutes a shock through which particles are accelerated. It is now suggested that secondary particles produced in the shock itself could significantly increase the escaping positron fraction [105]. Decent fits of the data are obtained within this scenario, which turns out to be falsifiable. This model predicts a rise in the B/C ratio, which is not favored by current observations [106], as well as a rise of the antiproton to proton ratio above 100 GeV. The PAMELA satellite has now precise results up to ∼100 GeV and it is foreseen to measure higher energy antiprotons. Therefore, it will be possible to test this scenario in the near future. Another conventional interpretation relies on the inhomogeneity of the cosmic ray sources. For instance, it is shown in [107] that the larger concentration of supernova remnants in the Galactic spiral arms and the contribution from a few known supernova remnants can reproduce the measurements.

A complete discussion of purely conventional solutions is beyond the scope of this manuscript. For more details see for example [108] and references therein. However, it clearly appears that there is no need for DM to explain the data.

## 8    Outlook

The origin of the cosmic lepton anomalies is still to be found. Most likely, the excesses are not caused by conventional secondary cosmic rays, meaning that a nearby source still to be identified contributes significantly to the local flux. To identify the origin of the anomaly will require new data, provided for example by AMS-02. This will allow measuring the effects more precisely and also all the other particle fluxes that serve as inputs to the propagation models. The improved identification capabilities of the apparatus might allow to measure the positron fraction up to higher energies and address questions such as: does the fraction rise up to 50%, or does it flatten as AMS-02 results seem to indicate? Is the excess in the $e^+ + e^-$ channel mostly due to electrons or positrons? Another important observable is the dipole anisotropy. An upper limit of 0.5% to 10% has been derived from Fermi data [109] for all leptons, and 2013 results from AMS-02 yield a limit of 3.6% for the positron fraction. In the future, even with larger

statistics AMS-02 might not be able to observe a privileged arrival direction for cosmic leptons. If a future experiment was able to do so, this would allow to narrow down the possibilities regarding astrophysical source candidates.

From the point of view of astrophysics, these observational results are very important as they offer a new channel to study sources of cosmic rays. From the point of view of DM searches though, these results are bad news. Indeed, they indicate a new background contribution that was not correctly accounted for previously. The consequence is that the potential of the corresponding channels are weakened, for both putting constraints and making possible discoveries. DM searches in these channels are not completely over but of course this source of background that was not previously accounted for will have to be understood before putting some constraints. It might therefore be wise to consider other channels more seriously. Two channels are particularly interesting. The first one is antideuterons. As $\bar{p}$ and $\bar{n}$ are expected to be produced in DM annihilation processes, a small yield in $\bar{D}$ is expected as well. Compared to antiprotons, the antideuteron channel has a nice advantage as $\bar{D}$ production is expected to be suppressed in the spallation processes at energies below 10 GeV. Actually the DM annihilation produce particles almost at rest, which increases the probability for $\bar{p}$ and $\bar{n}$ to merge. Alternatively $\bar{p}$ and $\bar{n}$ are produced with a large boost in cosmic ray collision processes, so that the secondary $\bar{D}$ is expected to be low for these low kinetic energies. The foreseen GAPS experiment [110] will specifically search for $\bar{D}$ from DM annihilations. The other channels that remain competitive are the neutral ones, neutrinos and gamma rays. The latter is discussed in the next chapter.

# Chapter 2

# Probing particle physics with gamma rays: WIMP dark matter and axion-like particles

*"I'm not normally a religious man, but if you're up there, save me, Superman!"*

– Homer (Simpson)

## 1   Introduction

In the previous chapter, the indirect search for WIMP dark matter has been presented through its possible channels in charged cosmic rays. Backgrounds related to a probable nearby source of e$^{\pm}$, and the absence of hints in the $\bar{\mathrm{p}}$ channel decreased their interest. After the studies presented in Chap. 1 were conducted, I spent more time on studying the possibility to search for WIMP dark matter with gamma rays. Gamma rays and neutrinos have the advantage of traveling straight from the sources and allow more dedicated searches. It is indeed potentially possible to reduce conventional signals by observing well-chosen regions where dark matter is thought to be more concentrated. Most of the research work presented here concerning DM searches with photons has been conducted within the HESS collaboration – where I was appointed co-convener of the *Astroparticle Working Group* in 2013–, or consider observations with ground-based gamma-ray telescopes. Some of the studies presented here take advantage of the previously formed collaborations. In particular we studied the possibility to search for DM clumps with Cherenkov telescopes [111], in collaboration with Jürg Diemand's group working on N-body simulations. Together with the group in Saclay we showed that dwarf galaxies might not be the best choice for searching for DM annihilations, as some conventional signals may appear. This fact was explicitly demonstrated in the case of the Sagittarius dwarf galaxy [112]. These studies have always been conducted with the aim to estimate what CTA could do in the future, and I joined the effort for CTA prospects in the field of dark matter and fundamental physics [113].

Besides the work on WIMP dark matter, I conducted prospective work concerning the search for exotic physics with ground-based Cherenkov telescopes, some of which will not appear in this report. This work focused mostly on observations of extragalactic sources. The large collection area of our telescopes, the high energies they grant access to, allow for deep observations of distant sources. In the past few years, extragalactic gamma-ray astronomy became relevant to the field of cosmology. For instance, gamma-ray observations allow to measure the density of the universe's background light, which is related to star formation and cosmological parameters. It also allows to search for cosmological-scale magnetic fields and could also be used to search for gamma-ray counterparts to GZK events, or gravitational lensing of gamma rays. On a more hypothetical ground, extragalactic observations in high energy can constraint Lorentz invariance violation, or allow searching for axion-like particles (ALPs). The wealth of areas that

are accessible to study with extragalactic observations led me to propose a project including these ideas to the ANR French national funding agency. In 2012, I received an ANR grant for the *CosmoTeV* project to conduct research in that direction. Before searching for exotic effects in the extragalactic sky, it is important to understand the conventional processes both at the source and during the propagation. Some studies that are not mentioned in details later include some modeling of the blazar emission [114, 115], and constraints on the gamma-ray opacity [115]. As we shall see at the end of this chapter, ALPs can modify the opacity of the intergalactic medium and/or of some regions within the source. In particular ALPs are sometimes invoked to explain the opacity of some class of extragalactic sources, namely flat-spectrum radio quasars (FSRQs). In [116] we propose a conventional model for the opacity of one such source. Over the last two years, I have been supervising the PhD work of Denis Wouters. We worked on extragalactic observations with HESS (he is the corresponding author of [115]) and we have investigated more specifically the possibility to detect ALPs using VHE gamma-ray sources. At first, we wanted to use results from the literature for the ALP signature but, as described in [117], we demonstrated that the signature that is usually sought is not actually observable for single source observations. We found out however a new possibility for a signature, that is magnetic turbulence-induced noise in the energy spectra. The derivation of the expected signal is published in [117]. This signature has then been used on X-ray data and gamma-ray data to derive constraints on the ALP coupling to photons. Those two studies led to publications in The Astrophysical Journal [118] and Physical Review D [119]. Still following the idea of inspecting the prospects for CTA, we are currently studying its sensitivity to ALPs through spectral irregularities [120]. In addition, we proposed a new method based on the opacity anomaly anisotropy to test for the anomalous transparency scenarios with CTA. The corresponding article has been submitted to JCAP [121]. Finally, I set up collaborations with the theory division in Saclay, for studying the large scale magnetic fields and modified gravity models in which axion-like particles appear. A study of the latter will soon be submitted [122].

This chapter presents some of the aforementioned studies and is organized as follows. First, a part is devoted to a quick description of the Cherenkov telescope techniques. Then, some pieces of work relative to WIMP searches are presented, with some perspective for the future, in particular with CTA. In a second part, examples of studies related to the search for ALPs with high energy photons, X rays and gamma rays, are presented.

# 2 Gamma-ray astronomy with Cherenkov telescopes

## 2.1 Principle

The basic idea of running ground-based telescopes to observe cosmic gamma rays is to use the atmosphere as a calorimeter. When a high-energy particle hits the top of the atmosphere, it induces a cascade of secondary particles. At energies of about 1 TeV, that cascade is fully contained in the atmosphere, and it produces a flash of Cherenkov photons. Hadronic and electromagnetic particles produce different types of cascades. While hadrons induce irregular particle showers, electrons, positrons and gamma rays produce more even showers. The Cherenkov flash is contained in a cone of $\sim 1°$ opening angle produced at $\sim 10$ km height. The projection of the cone on the ground is a disk of order 250 m diameter, and the flash lasts about 5 ns for a photon arriving at zenith. From any place inside this disk, the atmospheric shower is observable, should one use a sensitive enough instrument. Ground-based gamma-ray observatories use this principle to measure gamma-ray induced Cherenkov light, as sketched in Fig. 2.1. Large dishes are used to collect enough photons, those are focused on very sensitive cameras equipped with photomultiplier tubes. The cameras are able to integrate the signal very quickly and to resolve the image of the atmospheric showers, in order to fight against different types of backgrounds, as we shall see in the following. To gain in angular resolution, energy resolution and background subtraction, several telescopes are used simultaneously to observe the event, thus offering a stereoscopic view of the particle cascade.
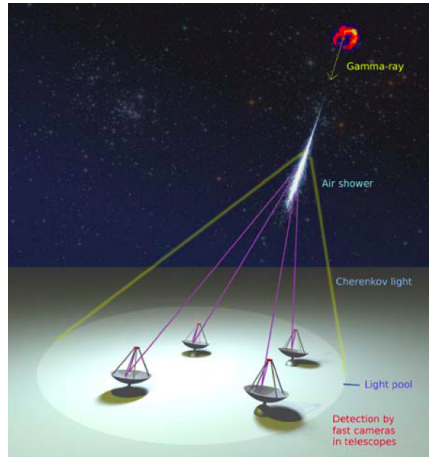
Figure 2.1: Principle of the Cherenkov telescopes, several telescopes measure the Cherenkov flash induced by the initial gamma ray (image from K. Bernlöhr [123])

.

## 2.2 Backgrounds, data analysis and caveats of the technique

As it can be inferred from the description of the technique in the previous subsection, the main backgrounds one has to fight against in order to have an image of a TeV source in the sky are:

- The night-sky background : diffuse light from stars, light pollution, the Moon, etc

- Cherenkov light induced by hadronic cosmic ray showers

- Cherenkov light from electron and positrons cosmic ray showers

- Diffuse gamma-ray emission that could overcome the signal from the source

Schematically, the image of the source is obtained when all these backgrounds are mastered, as shown on the sketch of Fig. 2.2. We shall now describe the basic principles that allow to suppress these backgrounds (see [124] for a pedagogical application).
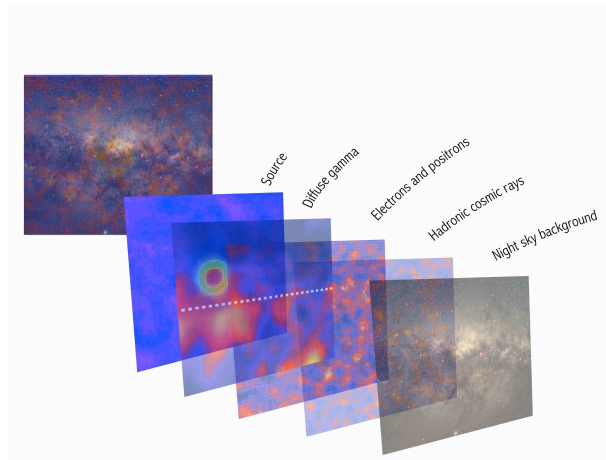


Figure 2.2: Schematic representation of the different layers of background that Cherenkov astronomers have to suppress to obtain an image of the TeV sources.

The night sky background (NSB) is fought against mainly using fast integration electronics. The closer the observation to the 5 ns of the actual shower flash, the less NSB is integrated. Fig. 2.3 shows simulations of images of an atmospheric event obtained in the camera of a Cherenkov telescope. Here the same simulated gamma-ray induced signal is integrated over 100 $\mu$s, 1 $\mu$s and 10 ns. For the longest integration times, the NSB signal dominates, whereas the electromagnetic shower appears clearly in the camera when the integration is done fast. Depending on the experiments, different techniques are used (flash ADCs, analog memories), and the actual integration of the signal is of order 10 ns at best. Another way to suppress NSB is to use a triggering strategy that favors signals that are clustered, as the NSB is expected to be fairly constant over the field of view of the cameras. Because of the NSB only moonless nights are proper to observations, leaving about 1000 h per year.



100 $\mu$s       1 $\mu$s       10 ns
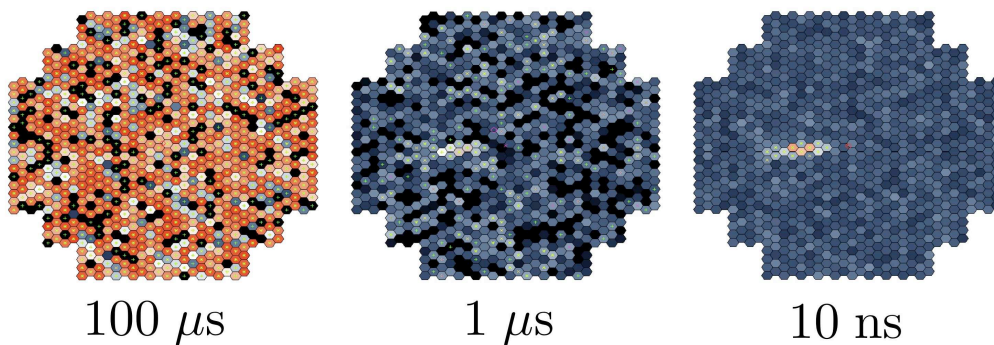
Figure 2.3: Three simulated image of a gamma-ray shower, obtained with different integration times: from left to right 100$\mu$s, 1$\mu$s and 10 ns (courtesy K. Bernlöhr).

Stereoscopy allows to reject a lot of hadronic background, in particular in case of the presence of muon rings, which appear in only one telescope. This suppression is done online, with a central trigger system [125]. Other types of background are suppressed during the offline analysis. First, one has to get rid of the images of cosmic ray induced showers. This is handled by the ability of the telescopes to resolve the atmospheric event. Showers produced by protons and heavier species are irregular because of the large transverse-momentum particles that are produced during its development, the presence of muons from hadronic decays, and electromagnetic sub-showers. A comparison between the total Cherenkov light produced by a 1 TeV gamma ray and a 1 TeV proton is shown in Fig. 2.4
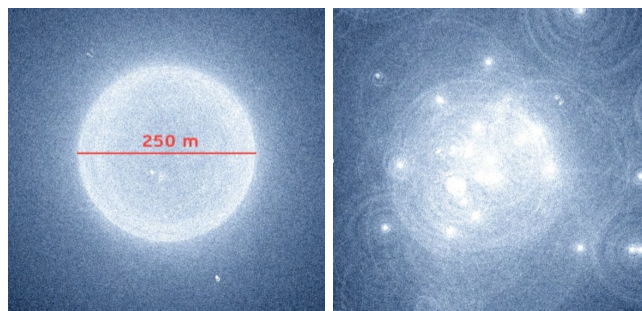


Figure 2.4: Ground projection of the Cherenkov light produced by a gamma ray of 1 TeV (left) and a proton of 1 TeV (right). The signal is integrated over 70 microseconds here (courtesy K. Bernlöhr).

Because heavy cosmic rays induce irregular showers, their images can be rejected during data analysis. In Fig. 2.5, different images obtained in the focal plane of a telescope are displayed. In this figure, the left panel shows an image of a hadronic shower, the central panel is the image of a single muon ring (from a

hadronic shower that is outside the telescope field of view), and the right panel is the image of a gamma-like event. The offline analysis tools are designed to reject the two first ones, and keep the last one, based on the topology of the image. To get an idea of the rejection power of the analysis, for a typical bright source, 10 h of observation yield $10^7$ recorded events, out of which $10^4$ are actual gamma rays. After the topology-based analysis procedure, $10^5$ events are selected, dubbed gamma-like events. At this point of the analysis, electron and positron cosmic rays are still present in the sample.



Hadronic shower      Isolated muon      Gamma-like event
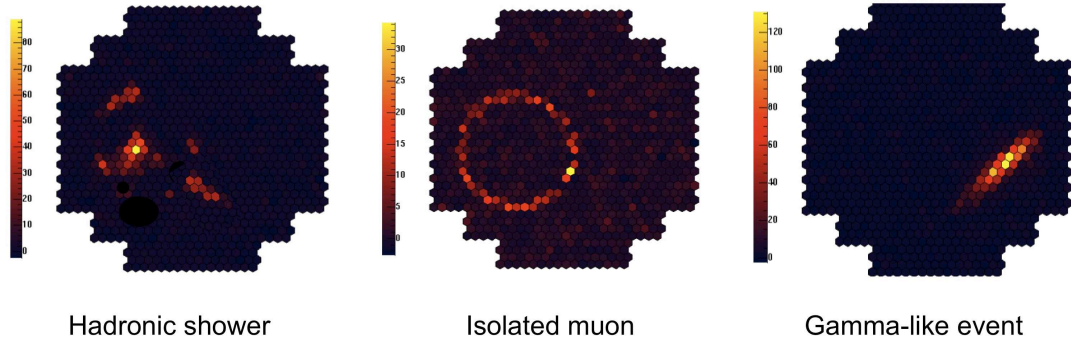
Figure 2.5: Simulated images of atmospheric events induced from cosmic particles, as observed in the focal plane of a Cherenkov telescope. From left to right: hadronic shower, isolated muon and gamma-like event (courtesy J. Hinton).

At fixed energy, electrons, positrons and gamma rays all induce identical electromagnetic showers, thus gamma-like events contain all these species. At the top of the atmosphere, the distribution of charged cosmic rays is isotropic. The background subtraction techniques are then based on the estimate of the isotropic part of the signal in a region of the sky where no gamma-ray signal is expected. This region is called the OFF region, and the corresponding event rate is subtracted where the source is expected to be (ON region). Most observations are taken in the so-called *wobble tracking* mode, for which the telescopes point slightly off the source; in HESS, this offset is usually $0.5°$. The acceptance being almost azimuth-symmetric in the field of view and flat on such an angular scale, this method allows to have OFF regions with the same acceptance as the ON region. Fig. 2.6 displays two possible choices for OFF regions, and a histogram showing the signal from the source and the background. In the first case (top), the source is on the left part of the figure (dark region) and the background is taken in a reflected region of same size. In the second case, to have a better estimate of the background, multiple same-size OFF regions are taken at a fixed offset with respect to the pointing direction. To build sky maps with extended sources of diffuse emission, another method is used where the background is measured in a ring. In that case one has to subtract the background with a correction corresponding to the effective exposure in each bin of the sky. The residual background is composed of electrons, positrons, residuals from misidentified hadronic showers. This residual background appears in the right panel of Fig. 2.6, for large values of $\theta^2$, $\theta$ being the angle from the source position Note that if an actual gamma-ray signal is diffuse all over the field of view with few variations, this technique will likely erase it. The general rule is that a diffuse signals is observable with Cherenkov telescopes provided its extension is smaller than the field of view of the experiment, which is about a few degrees. Observing larger scales diffuse emission requires less common techniques such as dedicated OFF runs, which have a significant cost in terms of observation time.

The energy of the initial gamma ray is deduced from the amount of collected Cherenkov photons, and comparison to Monte Carlo simulations matching the data taking conditions. Uncertainties lie in the knowledge of the atmospheric conditions, simulation uncertainties and intrinsic shower fluctuations. At the end, the energy resolution is about 10% [124].
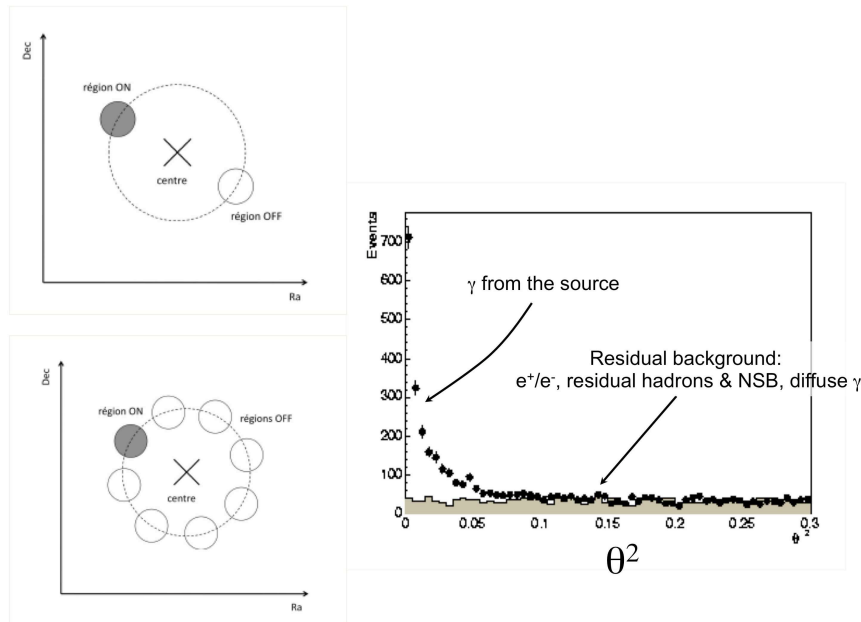
Figure 2.6: Illustration of the ON-OFF background suppression technique. In the left panels, the telescopes track a point in the sky represented by the cross in the center, while the source is offset by 0.5°, see text for details. In the right panel, the excess appears at low $\theta^2$ values, $\theta$ being the angle from the source position (figures from [126]).

## 2.3 Ongoing experiments

Current generation of Cherenkov telescopes all run in stereoscopic mode. In the northern hemisphere, MAGIC uses two large telescopes (17 m diameter) in the Canary islands, and VERITAS runs four telescopes of 12 m diameter. VERITAS is the successor of the Whipple telescope and is located in Arizona. In the southern hemisphere, the Cangaroo collaboration runs 4 10 m telescopes in Australia, and HESS consists of five telescopes in Namibia, four of 12 m and one of 28 m (see Fig. 2.7). The fifth telescope is running since 2012, so only four-telescope analyses are presented here. Fig. 2.8 shows the locations of these observatories on a map.

The Cherenkov technique is complementary to satellite-borne telescopes, such as Fermi. Fermi works between about 300 MeV and 300 GeV, has a full sky coverage with a large field of view, and a relatively small effective area, of the order of 1 m$^2$. Cherenkov telescopes have effective areas of the order of $10^5$ m$^2$. Whereas Cherenkov telescopes run only at night when the sky is clear, Fermi can record data all around the clock, that compensates for the smaller effective area. The basic features one has to keep in mind in order to understand the pros and cons of using Cherenkov telescopes to search for dark matter are the following:

- Large effective areas, of order $10^5$ m$^2$

- Relatively small fields of view, of the order of a few degrees

- Angular resolution of about 0.1°

- Energy Threshold between 50 GeV and 200 GeV

- 10% energy resolution

- A duty cycle allowing ~1000 h of data taking a year

Figure 2.7: The HESS array of Cherenkov telescopes in Namibia.



Figure 2.8: Current generation of Cherenkov telescopes observatories around the globe.

Figure 2.9: Artist's view of a possible layout for the CTA observatory: three classes of telescopes (large, medium and small) will allow to cover a wide energy range from 10 GeV to 200 TeV.

## 2.4 The future : the Cherenkov Telescope Array

The next step for gamma-ray astronomy will consist of the building of a larger array of Cherenkov telescopes –the Cherenkov Telescope Array (CTA) [127]. The observatory will take advantage of proven experimental techniques on HESS, MAGIC and VERITAS, and use 50 to 100 telescopes. One site in each hemisphere will allow a full sky coverage. On each site, the observatory will be composed of three groups of telescopes, from the center of the array to its outskirts: large 23 m telescopes, medium 12 m telescopes and small telescopes that could be a few meters in diameter. A possible sketch of the array is illustrated in Fig. 2.9. Some of the telescopes of CTA could be of a new kind, with a double-optics design. The use of different size telescopes is intended to cover a wider energy range from a few 10 GeV to 200 TeV. The sensitivity will be improved by a factor of ten compared to current generation arrays and the angular resolution will be improved by a factor of up to four. The energy resolution and the duty cycle will be similar to what exists now. The field of view will depend on the class of the telescope, from $\sim 3°$ for large ones to up to $8°$ for small ones. It is actually difficult to build Cherenkov telescopes with much larger field of view. This is because once the size of the reflecting dish is fixed, a larger field of view is obtained by a greater focal distance implying the requirement to hold a larger camera further away from the dish. This is challenging from a mechanical point of view. Double-optics telescopes might solve the problem as the focal plane is brought back closer to the primary mirror thanks to the secondary mirror. The layout of CTA will allow a flexible operation: deep observations of a region of the sky involving the whole array, larger surveys with subarrays pointing in different positions on the sky, regular observation with 3/4 of the array while the other quarter monitors variable sources, etc.

# 3 WIMP dark matter and its indirect search through gamma rays

## 3.1 Expected signals in Cherenkov telescopes and derivation of constraints

Within the Galactic halo, some of the dark matter (DM) particles happen to collide, producing standard model particles. Like for cosmic rays in Chap. 1, this exotic production of standard model particles is associated with the emission of gamma rays with energies of the order of the DM particle mass (here assumed to lie between 100 GeV and a few TeV). The gamma-ray emission associated with DM particle

annihilations provides a chance to detect DM particles. The expected energy-integrated gamma-ray flux from a region of volume $V$ at a distance $D$ with DM density $\rho$ is

$$\phi_\gamma \;=\; N_\gamma \, \frac{\langle \sigma v \rangle}{m^2} \, \frac{1}{4\pi D^2} \, \int_V \mathrm{d}V \, \frac{\rho^2}{2} \;\;, \tag{2.1}$$

where $N_\gamma$ is the number of gamma rays per collision, $m$ is the DM particle mass. The number $N_\gamma$ is strongly dependent on the energy threshold of the experiment, as it is the integral of all photons from its threshold to the DM mass. As the expected DM-induced photon energy spectra are quickly falling with energy, it is then always better to have a low energy threshold, in order to be sensitive to more photons. The defined volume $V$ can contain a whole DM structure (*e.g.* a in dwarf galaxy) or part of it (like for the Milky Way halo).

Up to now, no convincing DM signal has been observed, so the way to present the results is to draw a limit in the $\sigma v$-$m$ plane. The flux sensitivity of an experiment is determined by the characteristics of the corresponding observation: effective area, exposure time, data quality, zenith angle of the target etc. The experimental work consists precisely in determining the flux sensitivity. Then, for a fixed particle DM mass $m$, a limit on the cross section $\sigma v$ is computed for the expected signal not to be larger than the sensitivity. This can be performed provided the DM density within the observed region is properly modeled. This is the main source of uncertainty in this type of analysis. The constraints are usually compared to model predictions that are computed with codes such as DarkSUSY [128] or micrOMEGAs [44]. Depending on the particle physics model, the dependence of $N_\gamma$ on the mass of the DM particle is different. Some collaborations (Whipple, VERITAS, sometimes HESS) choose to use a generic parameterization for $N_\gamma(m)$ which is not exact but somehow gives the average value over a possible range of models. It is also possible to extract the value of $N_\gamma$ from the model and compute the constraint point by point. This is the way MAGIC presented some of its results and in that case the constraint is not a continuous line. Another approach is to show the constraints obtained with the two extreme final sates which are $\tau^+\tau^-$ and $b\bar{b}$.

As for the choice of the targets, the halos of galaxies and clusters of galaxies are assembled through the merging of a large number of smaller structures. Most mergers are incomplete and large cold dark matter (CDM) halos, *e.g.* the one around the Milky Way, harbor an enormous population of subhalos, which are a record of its assembly history. Some of these subhalos, for the most massive of them, contain baryonic matter and stars, making up the satellites of the Milky Way. A careful study of the kinematics of those stars allow obtaining constraints on the DM mass content of the satellite, which can help to reduce the uncertainty on the constraint. However, the presence of baryons in the center of halos can modify the density profile of the DM. Then, only subhalos that do not contain baryons are expected to have their primordial shape untouched. The interaction of the satellite or the subhalo with the gravitational potential of the Milky Way can also cause the profile to be significantly modified by tidal effects. In this chapter we shall see results from all types of sources: dwarf galaxies with strong tidal disruption or none of it, globular clusters for which baryons could have played a role, the Galactic center where there is a conventional gamma-ray source, and DM clumps, which are basically untouched subhalos. In all cases, the ideal signal one would expect from a dense DM region has the following features:

- Slightly extended, with an extension of order $1°$ and a halo-type morphology

- Steadiness: it should have strictly no time variability

- No high-energy counterpart

- No nearby conventional source

- Cutoff at electroweak-like scale in the energy spectrum

- A few alter-egos with the exact same properties in the sky

37

## 3.2 Searches towards known targets

A common strategy is to select targets where the WIMP annihilation process can occur efficiently, and observe them with a sufficient amount of time. Targets are selected thanks to the observation of stars and study of their kinematics. This allows to infer the DM mass content of the target, although usually with sizable uncertainties. The knowledge of their positions in the sky is very precious for Cherenkov telescopes, because of their relatively small fields of view and background subtraction techniques. The presence of baryons can have drawbacks too, they can alter the DM content of the target or induce conventional gamma-ray emissions.

The most dense region of our Galaxy is its center, located at 8.5 kpc. HESS dedicated almost 50h of observation to the source at the Galactic center [129] before 2006. Among all the targets discussed here, it is the only one for which a gamma-ray emission has actually been found. It has been shown that most of the emission cannot be due to DM annihilations. The reason is that the energy spectrum of the source does not fit a DM-like spectrum. One should note also that unlike some other targets mentioned here, several identified astrophysical objects that could be at the origin of the emission are indeed present in the same field of view. To infer constraints in the $\langle \sigma v \rangle$-m plane, the authors of [129] search for the maximal cross section for which the energy spectrum does not exclude the corresponding DM contribution. It was determined from these observations that the annihilation cross-section could not be larger than $\sim 5 \times 10^{-24}$ cm$^3$s$^{-1}$ for WIMP masses between 200 GeV and 30 TeV.

Other observations have been conducted by HESS, VERITAS, MAGIC and Whipple. All of them get their constraints from the fact that no signal has been found. From the knowledge of the observation conditions, and the measured level of background, it is possible to derive an upper limit at some confidence level $C.L.$ on the number of gamma rays in the signal region $N^{C.L.}$. Then Eq. 2.1 can be inverted to derive an upper limit on the annihilation cross section, given a WIMP mass $m_\chi$ and an annihilation spectrum $dN/dE$

$$\langle \sigma v \rangle^{C.L.} \;=\; \frac{8\pi}{J} \frac{N^{C.L.} m_\chi^2}{T_{obs} \int_0^{m_\chi} dE A_{eff} dN/dE} \;, \tag{2.2}$$

where $J$ is the integral of the squared DM density on the line of sight within the signal region, $T_{obs}$ is the observation time and $A_{eff}$ is the effective area of the telescope array.

Fig. 2.10 presents a summary of the observed targets, with their types, distances, the corresponding experiment and exposure used to set the constraint. The constraints on the annihilation cross section from these observations cover a wide range of values. These constraints are not equal in terms of associated uncertainties, in particular related to the modeling of the DM halo. The constraints vary when the DM content of the target is varied within the region that is compatible with star kinematics. Some results can thus be considered as optimistic, that includes observations of the Canis Major overdensity, Sagittarius dwarf galaxy (that experienced strong tidal stripping), the results from the Galactic center, as well as the results from M15, for which a very optimistic assumption has been made (adiabatic contraction around a hypothetical central black hole).

Concerning the Milky-Way satellites, the most sensitive analyses from HESS, MAGIC and VERITAS yield constraints that lie in the $10^{-23..21}$ cm$^3$s$^{-1}$ range. Those are displayed in Fig. 2.12, they correspond to the observations of the Sculptor dwarf galaxy by HESS [135], and observations of the Segue 1 dwarf galaxy by MAGIC [139] and VERITAS [140]. In the case of Sculptor dwarf galaxy, the band represents the uncertainty associated to the DM profile reconstructed from optical data. As explained in the previous section, the constraints have different shapes because of the parameterization of $N_\gamma$ and the different energy dependence of the effective area of the experiments. Another important parameter for the shape is the definition of the threshold for the experiments. In the same figure, the constraints obtained by Fermi are displayed. They are obtained with a combined analysis of ten dwarf galaxies [144, 145]. The width of the constraint corresponds to the uncertainty related to the DM content of the dwarf galaxies. One can note that the constraints are very complementary. The advantage of Fermi here is the much lower energy threshold (below 1 GeV) and the very long exposure.

Galaxy clusters have been observed by HESS (Fornax [135]), MAGIC (Perseus [138]) and VERITAS (Coma [141]). The constraints in that case benefit from analyses that integrate larger regions of the field
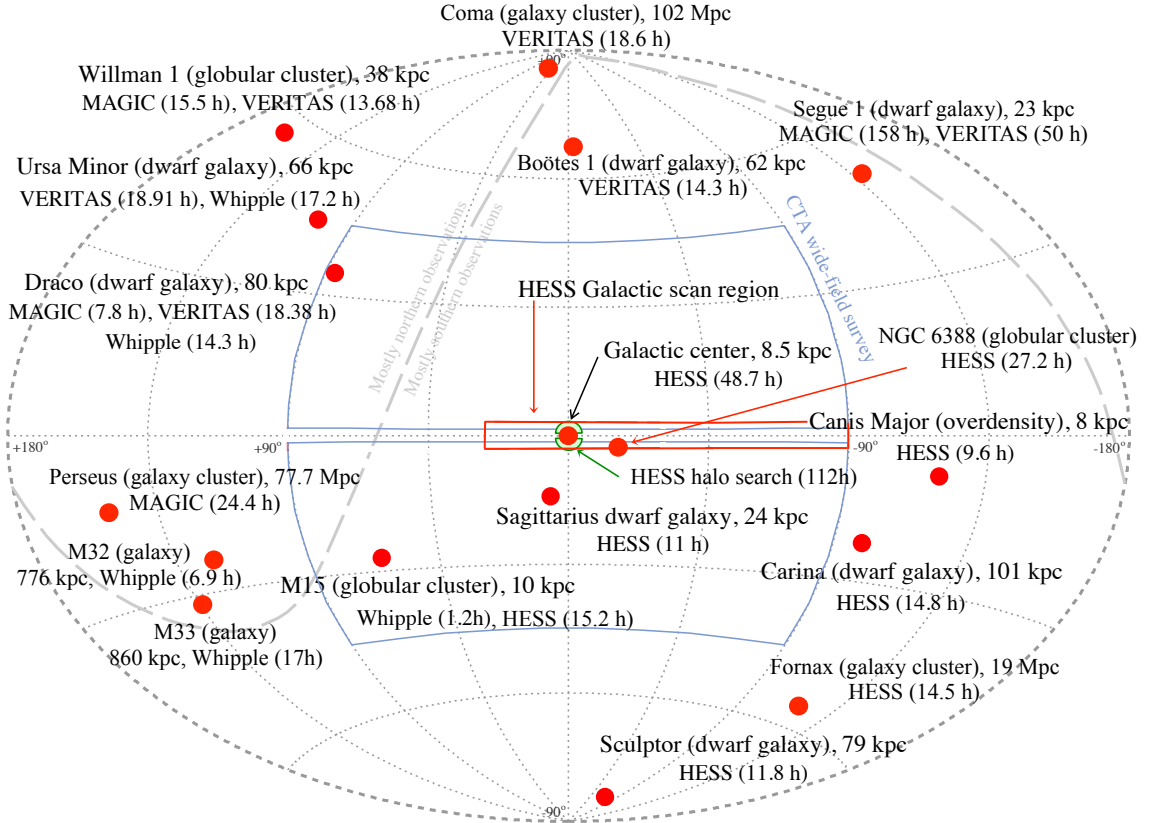
Figure 2.10: Galactic coordinates representation of the targets so far observed by IACTs, and their main characteristics: distance, type and experiments that observed them, with corresponding exposure. The displayed targets are the Galactic center (HESS [129]), Sagittarius dwarf (HESS [130]), Sculptor (HESS [131]), Carina (HESS [131]), Draco (MAGIC [132], VERITAS [133], Whipple [134]), Fornax (HESS [135]), Willman I (VERITAS [133], MAGIC [136]), Ursa Minor (VERITAS [133], Whipple [134]), Canis Major (HESS [137]) and M15 (Whipple [134]), Boötes [133], M33, M32 [134], Perseus [138], Segue 1 (MAGIC [139], VERITAS [140]), Coma (VERITAS [141]) and NGC 6388 [142]. Also shown are the regions of the HESS galactic scan, the HESS galactic halo search (not to scale) and the proposed CTA wide-field survey. Figure adapted from [143].

of view, due to the extension of these objects in the sky; on the other hand the large distance where they lie deteriorates the limits. For illustration, the constraints obtained from the Coma clusters are displayed in Fig. 2.12.

The Galactic center is different from the above mentioned targets because it harbors a strong gamma-ray source. An idea that has been developed and used in HESS is to search for a signal in the region of the Galactic center, that is associated to the smooth part of the halo in an annulus around the center [146]. The search region corresponds to a distance $r \sim 45 - 150$ pc from the center. The main interest of this type of search is that it excludes the most central part of the halo, which is subject to large uncertainties and of course contains the source. Therefore, unlike dwarf galaxy analyses, the obtained constraints do not depend much on the assumptions regarding the DM halo profile. The main difficulty in this type of analysis is to define the OFF regions where residual backgrounds are estimated. For each pointing direction, the background for each pixel of the map is chosen further away from the center, where the DM signal is expected to be less intense. For each considered ON pixel, the OFF pixel is chosen at the same radial distance from the pointing direction as the acceptance is approximatively symmetric. Some regions are excluded because they are known to contain conventional signals, like the Galactic plane and known sources. If no OFF pixel can be found, then the pixel is not used. The method is illustrated in Fig. 2.11 for a specific pointing direction, indicated by the star.
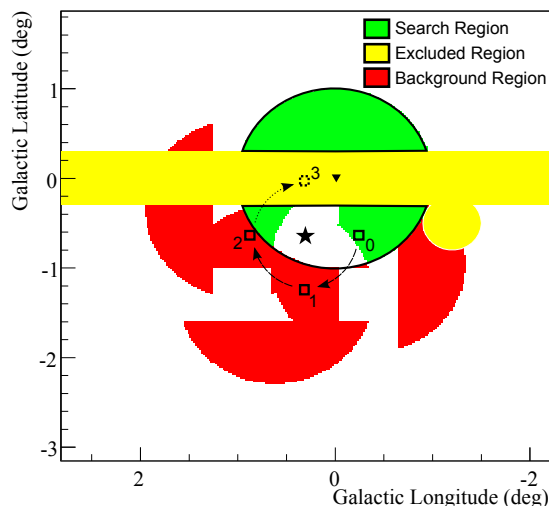


Figure 2.11: Illustration of the pixel-by-pixel background subtraction technique, for a given pointing direction indicated by the star (figure from [146]).

This method has been used to derive constraints on the WIMP annihilation cross section, using 112 h of data. The obtained constraints are shown in Fig. 2.12, they are the current best limits from Cherenkov telescopes.

## 3.3 Potential limitations of targeted searches : an example with Sagittarius dwarf

Dwarf galaxies are good candidates to search for DM signals. They are however detected and characterized on the basis of their baryonic content, which is obviously required to observe *e.g.* their stars in the optical band. The presence of this baryonic content has two potential effects regarding the search for DM signals: (i) it can modify the DM distribution with respect to estimates based on N-body simulations, and (ii) it can lead to the generation of conventional signals. The first point is handled by estimating the range of constraints that is obtained with different hypotheses, as done in the previous sections. The second

Figure 2.12: Compilation of constraints in the $\sigma v$–m plane, from HESS [146, 135], VERITAS [140, 141], MAGIC [139] and Fermi [144, 145]. All constraints are obtained assuming quark-antiquark fragmentation, and the bands stand for the astrophysical uncertainties.

point is illustrated here in the case of Sagittarius dwarf galaxy. Beside being a DM dominated object, this dwarf galaxy hosts a globular cluster in its center (M54). Globular clusters are known to be able to produce gamma rays, as in Terzan 5, which has been detected at TeV energies by HESS [147]. This emission 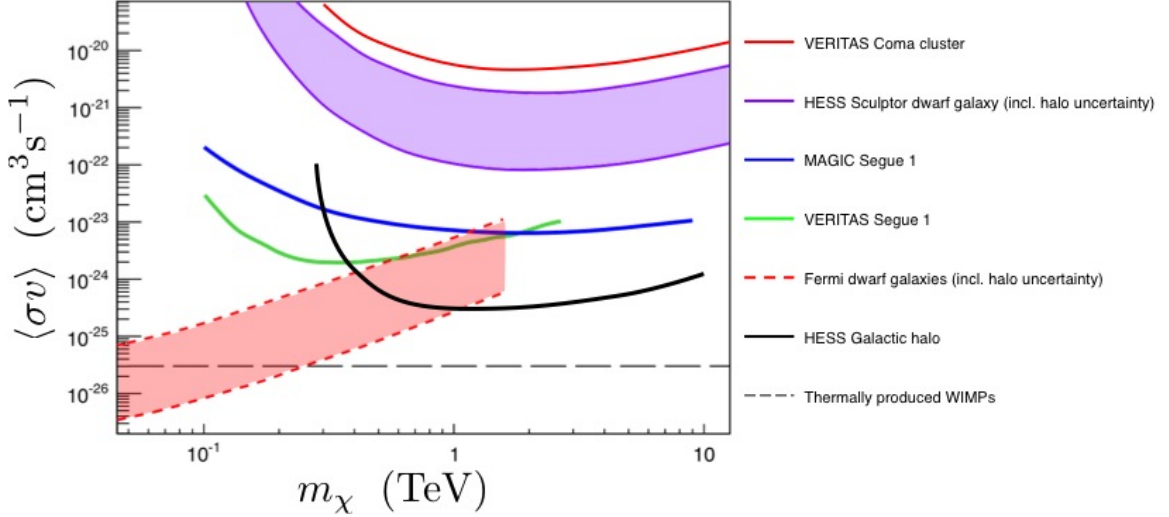is understood as a collective emission from a population of millisecond pulsars (MSPs) within the globular cluster. In [112], N-body simulations are used to infer the DM halo profile of the Sagittarius dwarf galaxy from the observation of its tidal stream as done in [148] and re-compute the constraints from the corresponding HESS observations. In addition, the CTA sensitivity is computed, and it is shown that the sensitivity to DM signals from Sagittarius dwarf galaxy is potentially limited in the future by two possible sources of conventional signals, that are related to the presence of M54. These signals can arise from a possible central intermediate-mass black hole, or a population of MSPs. It is shown that the latter would under common hypothesis prevent the detection of a DM signal with thermal annihilation cross section. Fig. 2.13 is adapted from [112] and displays the current constraints from HESS and the prospects for CTA under different hypotheses regarding the halo profile. The horizontal line shows the limit under which a DM signal would not be visible. Indeed below that line the MSP signal would overcome the DM signal.

It appears that targeted searches have some limitations. Assumptions based on N-body simulations may not be correct on scales as small as galaxies and in particular dwarf galaxies due to the presence of baryons. One strategy is to observe more massive targets such as galaxy clusters. This has been done with HESS with the observation of the Fornax galaxy cluster. In principle the predictions of the structure formation simulations are more accurate for such large scales but then one has to consider potential signals from cosmic rays and the effect of substructures which can be uncertain. Constraints obtained with HESS from the observation of Fornax are of the order of $\sigma v \sim 10^{-23}$ cm$^3$s$^{-1}$ [135]. Other strategies consider sky surveys or searches for object without baryonic content, as developed in next sections.

## 3.4 Blind searches for DM clumps

Although Cherenkov telescopes cannot perform wide-field surveys in a single shot, the maturity of this technique allows now to conduct scans of significant fractions of the sky, and make blind searches for new sources. This has been done with the HESS experiment, for scanning the Galactic plane [149]. This type
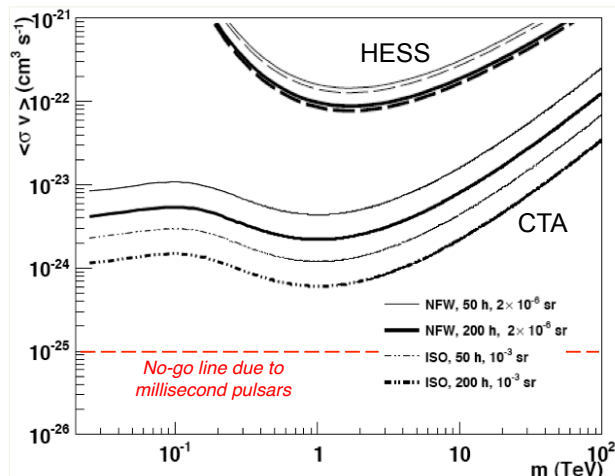
Figure 2.13: Current constraints from HESS observations of Sagittarius dwarf, future constraints with CTA and sensitivity limitation due to emission of pulsars.

of scan allows searching for DM clumps. Indeed the Milky Way halo is the result of the merging of a large number of smaller halos, some of which are in principle still present in the Milky Way, as predicted in the high resolution N-body simulations *Via Lactea II* [91]. In [150], data from the HESS survey has been used to build a sensitivity map used for the search of DM spikes around hypothetical intermediate-mass black holes. In [111] it is shown that in a more conventional scenario, a large number of subhalos are predicted to be in the scanned region (displayed in Fig. 2.10 as a red rectangle). The corresponding sensitivity map is displayed in Fig. 2.14. This map represents the maximal flux that an object could have in a certain region of the sky. Some parts of this map show a better sensitivity, due to a larger exposure, and some regions present smaller sensitivity due either to a small exposure or the presence of signal (source or diffuse emission).
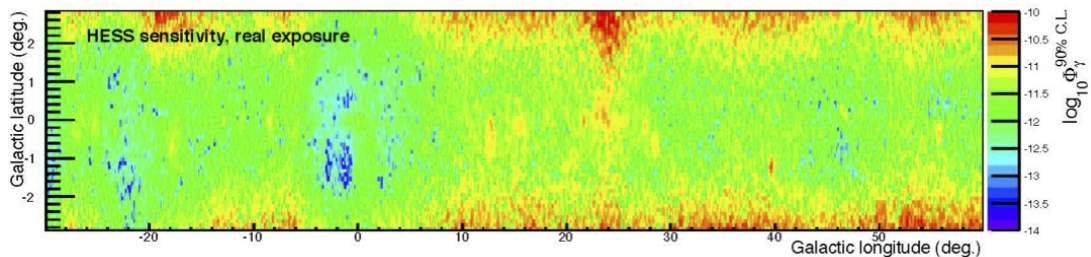


Figure 2.14: Sensitivity map for the HESS Galactic plane survey. The red regions where the sensitivity is lower are due either to a small exposure or the presence of signal (source or diffuse emission), figure from [111].

For given values of $\sigma v$ and $m$, annihilation within those objects could make a statistically significant number of them shine enough in gamma rays to be observable. From the observation perspective, none of the unidentified sources discovered in the HESS scan present the required characteristics to be DM clumps. Then, from the convolution of the sensitivity map with the prediction from DM clustering in numerical simulations, it is possible to get the constraints that are shown on Fig. 2.15. As shown on this figure, the results are again very complementary to Fermi wide field searches [151] although Fermi has a full sky coverage. The drawback from a much smaller scanned regions is compensated in the case of Cherenkov telescopes by a better flux sensitivity. The obtained constraints are of the same order of magnitude as

42

for targeted searches. Note however that the systematic errors on the DM distribution –although still present– are very different in the two cases.
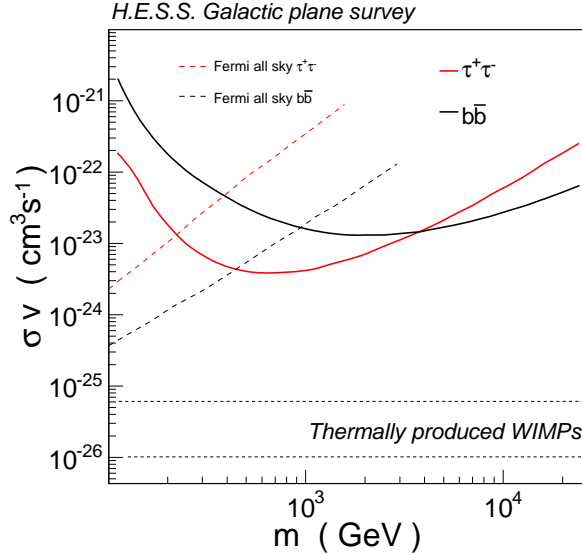


Figure 2.15: Constraints obtained from the search for DM clumps with HESS Galactic plane survey for different annihilation channels (solid lines). The results are compared to a similar search with Fermi, full sky (short-dashed lines), figure from [111]

Prospects for blind searches for DM subhalos take advantage of the fact that large surveys will be conducted by CTA independently of the search for DM. At least two large scans can be foreseen: a Galactic plane survey and a wider survey of one fourth of the sky. In [111], constraints on DM models are computed assuming no DM subhalo candidate is found. In the case of a HESS-like survey, constraints are computed with the same exposure, leading to the sensitivity map shown in Fig. 2.16. To build this map, a population of sources has been simulated, appearing in the map where the sensitivity decreases (red spots in Fig. 2.16). It is assumed here that no significant diffuse emission is discovered over that observed by HESS. Such an analysis would allow for an improvement of the HESS constraints by a factor of ten (see the dashed lines in Fig. 2.17).
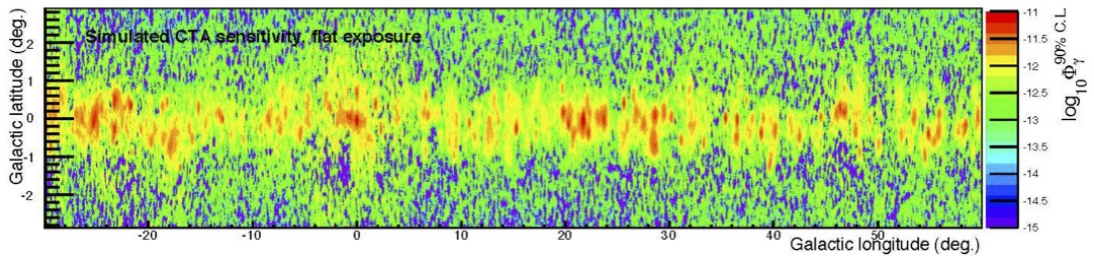


Figure 2.16: Simulated sensitivity map for a CTA Galactic plane survey. The regions with less sensitivity are due to the presence of sources, no diffuse emission is included in the simulation (figure from [111]).

To go further, the 1/4 sky survey will have to be used. In that case, in [111] the scan regions have been optimized: centered on the Galactic center, with the exclusion of latitudes between $\pm 1.5°$, (blue region in Fig. 2.10). In that case the sensitivity is considered assuming no diffuse gamma-ray background or extended sources are present in the observed fields. The presence of point-like sources does not deteriorates

the sensitivity to clumps. With these assumptions, and within 6 years of data taking, this allows to reach the thermally produced WIMPs region, as shown in Fig. 2.17.
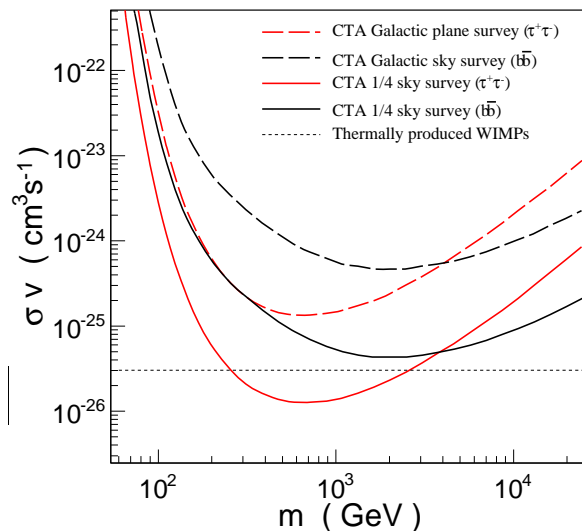


Figure 2.17: Expected DM constraints with CTA in the case of a galactic plane survey (dashed lines) and a survey of one fourth of the sky (solid lines), both for two distinct annihilation channels (figure from [111]).

## 3.5    Complementarity with other channels

Dark matter particles such as WIMPs are searched not only indirectly but also directly. They can be produced in high-energy particle colliders like the Large Hadron Collider at CERN. Dedicated detectors are also operated in the low-background environments that are underground labs. The comparison between the exclusion limits obtained by these different methods is not straightforward and can only be done within a model.

From an astroparticle perspective, it is important to note that neutrino telescopes provide an excellent way to perform dark matter searches, in a very complementary way to gamma-ray searches. Neutrino telescopes, such as IceCube at the South pole, can search for neutrinos from the annihilation of WIMPs in the Galactic halo, just the same way HESS does. With this method, they reach exclusions on the annihilation cross section at the level of $\langle \sigma v \rangle \simeq 10^{-22}$ cm$^3$/s above 1 TeV [152]. A more sensitive method is to search for neutrinos induced by WIMP annihilation in the Sun. In that case the quantity that limits the expected rate is the WIMP capture rate in the Sun. This quantity depends essentially on the WIMP-proton diffusion cross section. In that sense, this method is more comparable to direct searches as it constraints the same parameter. The constraint that is obtained depends on whether one assumes the WIMP interacts with a spin-dependent or spin-independent cross section. Such method showed to be more sensitive than laboratory experiments in the case of the spin-dependent WIMP-proton cross section [153].

## 3.6    The future of astrophysical WIMP searches

Indirect search is not the only way to search for WIMP signals, as hints or discoveries could come from direct searches or from the LHC. It is however essential if one want to prove that new particles actually hold together the large structures of the universe. Indirect searches are the only link between laboratory experiments and cosmology, they are inevitable in that sense. One nice thing about it is that it is not bottomless. A natural value for the annihilation cross section is provided by cosmology and such searches are worth doing until the sensitivity to this value is attained. In the near future, the fifth telescope of

HESS will probe even deeper the dense regions like the Galactic center halo. There has been some recent claims of observation of a gamma-ray line at the Galactic center, [154] and this second phase of HESS will allow testing that. After that, CTA will very likely allow to reach the natural scale for large-mass WIMPs for the first time. As an illustration Fig. 2.18 shows the sensitivity of CTA to WIMP annihilation using the search for clumps and a Galactic-halo type of analysis.
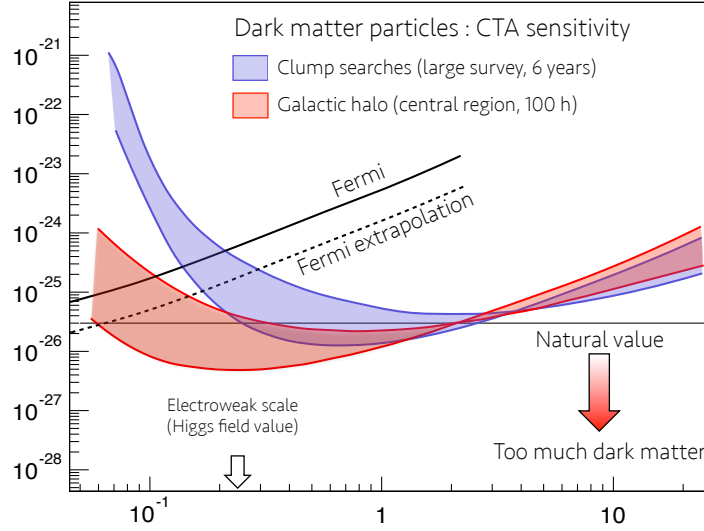


Figure 2.18: Sensitivity of CTA to WIMP annihilations, using blind searches for clumps (blue) and Galactic halo analysis (red). The Fermi results from dwarf galaxies and its extrapolation are shown, the colored areas correspond to the different possible annihilation channels.

# 4 Searches for axion-like particles

## 4.1 Strategy for searches for axion-like particles

As discussed in the preamble section, axions are light pseudo-scalar particles that are introduced to explain the absence of CP violation in strong interactions. They are good candidates to form the cold dark matter of the universe if their mass is below $1\mu eV$. Axion-like particles (ALPs) are hypothetical pseudo-scalar particles which phenomenology is similar to that of axions, except that unlike axions, their coupling to photons is not proportional to their mass. Axions and ALPs are experimentally searched through their coupling to photons, electrons or quarks. Here we focus on the coupling to photons. For the general ALP case, the interaction term with the electromagnetic field writes

$$\mathcal{L} \;=\; -\frac{1}{4} g_{\gamma a} F_{\mu\nu} \tilde{F}^{\mu\nu} a \;\;, \tag{2.3}$$

where $g_{\gamma a}$ is the dimensionful coupling between photons and ALPs, $F$ is the electromagnetic tensor and $a$ is the ALP field. The $F\tilde{F}$ term can be expressed as a scalar product of the photon electric field and the magnetic field, revealing the fact that ALPs can couple to photons in the presence of an external magnetic field. The interaction term between photons and ALPs can be written in terms of the electric field $\vec{E}$ and the magnetic field $\vec{B}$ as

$$\mathcal{L}_{\gamma a} \;=\; g_{\gamma a} \, \vec{E} \cdot \vec{B} \, a \;\;. \tag{2.4}$$

This coupling opens up the possibility of oscillations between photon and ALP states in an external magnetic field [155] and allows experimental searches for ALPs. There are four types of experiments

45

that are sensitive to ALPs (see [28] for a comprehensive review). The photon-ALP coupling is used to search for ALPs supposedly thermally produced in the Sun, as done with the CAST experiment [156]. In CAST, a magnet is pointed towards the Sun and it is intended to detect X-rays from the conversion of ALPs into photons inside the apparatus. Another search strategy assumes that ALPs make up the cold dark matter and use resonant microwave cavities, like in the ADMX experiment [157]. ADMX is sensitive to QCD axion dark matter and cover also a range of ALP parameters provided they form the Galactic dark matter. High-intensity laser beams in magnetic fields are used to performed light-shining-through-a-wall type of experiments, as done for example in the ALPS experiment [158]. As a general rule, the efficiency of the photon-ALP oscillation mechanism in an external magnetic field is maximized for large values of the magnetic field and long propagation baselines, as both these parameters increase the probability of conversion from one state to another. Astrophysical environments can offer bright sources of photons, strong magnetic fields and very long baselines. It is then natural to try using astrophysics to search for ALPs. Each of these search strategies probe different regions of the parameter space, as summarized in [28].The very high energy gamma-ray sky is a promising place to search for ALPs. A widely discussed observable is the opacity of the universe to gamma rays, due to pair production on photons of the extragalactic background light (EBL, see [159, 160, 161]).

In the present section, the use of natural environments to search for ALPs is emphasized, such as the propagation of very high energy gamma rays over cosmological distances and the effect of astrophysical magnetic turbulence on high-energy photon source spectra. First the conventional view of the problem of the opacity of the universe to gamma rays is presented, with possible indications for an anomalously transparent universe. Although the possible tensions can be solved in a conventional way, they can also be released by invoking ALPs mixing with photons. Then it is shown that this observable could be used as a signature when one tries to make a discovery, but that some uncertainties prevent from using it to derive robust constraints. It is then shown that constraints can be obtained by considering the effect of magnetic turbulence around the sources and finally some examples of constraints are given, as well as some prospects.

## 4.2 The transparency of the universe and ALPs

### The conventional view of the universe's opacity to gamma rays

Very high energy photons (with ∼TeV energies) traveling through the intergalactic medium encounter different populations of background radiations. The most numerous type of background photons belong to the Cosmic Microwave Background (CMB) and a second population is the extragalactic background light (EBL). The latter has a double bump structure, that comes from direct starlight and emission re-processed by interstellar dust in the infrared band as sketched in Fig. 2.19. Direct measurement of the EBL is very difficult because of foregrounds and infrared radiation by the instruments.

TeV gamma-ray astronomy is sensitive to the EBL density and spectrum as it is responsible for the attenuation of extragalactic source fluxes at high energy. The reason for that is the pair production process $\gamma_{\mathrm{TeV}}\gamma_{\mathrm{EBL}} \to e^+e^-$, for which the threshold lies at TeV energies in the terrestrial frame. For instance considering $E_{\mathrm{EBL}} \sim 0.1$ eV, the threshold energy satisfying $E_{\mathrm{th}}E_{\mathrm{EBL}} > m_e^2$ (where $m_e$ is the mass of the electron) yields $E_{\mathrm{th}} \sim 2.6$ TeV. In Fig. 2.19 the typical range of the TeV absorption range is indicated by the horizontal arrow. Because of the pair production process, the highest energy photons have a larger optical depth. Before 2006 it was commonly admitted that is was very unlikely to detect TeV photons from sources above $z \sim 0.2$. The situation changed after HESS observations of two active galactic nuclei (AGNs) at $z = 0.186$ and $z = 0.165$. As reported in [163], when unfolded from the EBL effect, the intrinsic spectra of these sources were found to be in tension with the source models. Spectral indices for the intrinsic spectra were actually reconstructed at lower values than 1.5, which was considered to be hardly reproduced by models of acceleration in relativistic jets. This was the first indication for a universe slightly more transparent than expected at high energy. Later, AGNs were observed at redshifts as high as 0.536 by MAGIC [164], $> 0.6$ by VERITAS [165] and possibly 0.61 by HESS [166]. The universe is indeed more transparent to gamma rays than expected. That puzzle has conventional solutions, it could be for instance that spectra are actually harder, this can be realized for instance including hadronic components
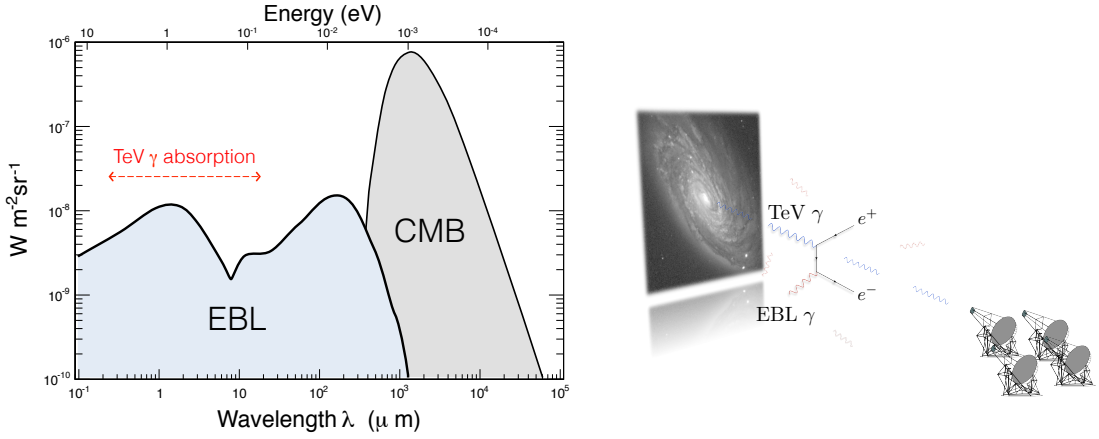
Figure 2.19: Left: Spectral energy density of the cosmic background photons including the CMB and the EBL (inspired from [162], with permission of the authors). Right: Illustration of the pair production process.

in the AGN jets or in relativistic shock acceleration models. The tension can be removed as well with a revision of the EBL models, mainly with a lower density as for instance in the model of [167] which is compatible with all observations. TeV observations are now even used to provide not only upper limits on the EBL density but actual measurements [168]. The current situation is illustrated in Fig. 2.20, extracted from [169, 115]. It represents the energy above which the absorption becomes significant (defined by a optical depth $\tau(E) = 1$) as a function of the redshift of the source. The lines correspond to models or lower limits for the EBL density and redshift evolution from [167, 170, 171]. Constraints from the spectral indices of different sources are shown as arrows, and the HESS measurement corresponds to the blue band. One source seems to be in tension with the measurement. However the methods that lead to the constraint and the measurements are different as the constraints rely on spectral slope measurements and the measurement comes from the observation of features in the spectra that can be related to the EBL spectral density. A more unified approach might be necessary to get a definite answer on how strong the tension is. Note also that the Fermi collaboration did the same measurement at higher redshifts and found a good compatibility with EBL models [172].

At this point it is important to realize that EBL measurements presents no strong anomalies and do not require ALPs. Some studies however still claim for an anomaly, even with the lower EBL limits from [171]. It is the case in [173], where the authors claim for an anomaly, with the caveat that their claim requires to leave out some error bars.

**How ALPs come into play**

The lack of opacity of the universe to gamma rays gave rise to the idea that ALPs could be responsible for this effect. The basic idea is that if mixing between ALPs and photons occur, the beam could travel in the form of ALPs on a significant fraction of way, not producing pairs, as sketched in Fig. 2.21. If ALPs are converted back to photons before observations, this could lead to a more transparent universe.

To get an idea of the relevant masses and couplings for the ALPs that are invoked here, let us consider the most simple formalism for describing the photon-ALP mixing. The system propagation is described by a Schrödinger-like equation:

$$(E - i\partial_z - \mathcal{M})\begin{pmatrix} A \\ a \end{pmatrix} = 0 \text{ with } \mathcal{M} = \begin{pmatrix} -i\frac{\tau}{2z} & \Delta_B \\ \Delta_B & \Delta_a \end{pmatrix}, \tag{2.5}$$

where $\Delta_B = g_{\gamma a} B_t/2$ describes the photon-ALP coupling ($B_t$ is the transverse projection of the magnetic field), $\tau$ is the optical depth related to EBL absorption and $\Delta_a = -m_a^2/2E$ accounts for the ALP mass.
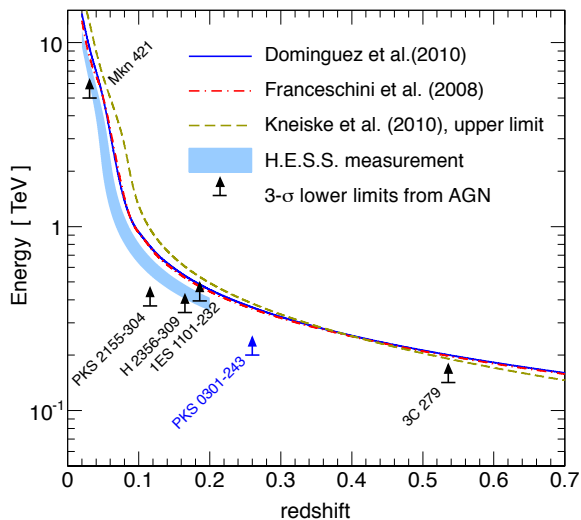
Figure 2.20: Energies corresponding to $\tau = 1$ for different EBL models, constraints from very high energy gamma-ray astronomy and 1-$\sigma$ measurements from HESS (figure from [169, 115]).
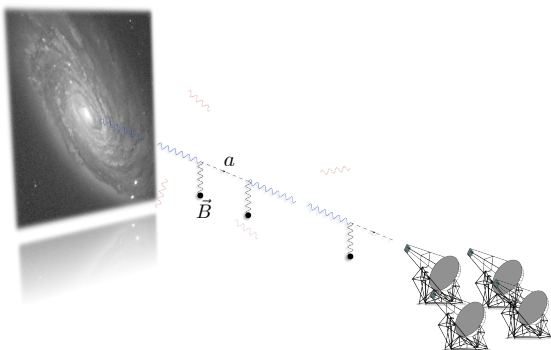


Figure 2.21: Illustration of the photon-ALP oscillations in a magnetic field
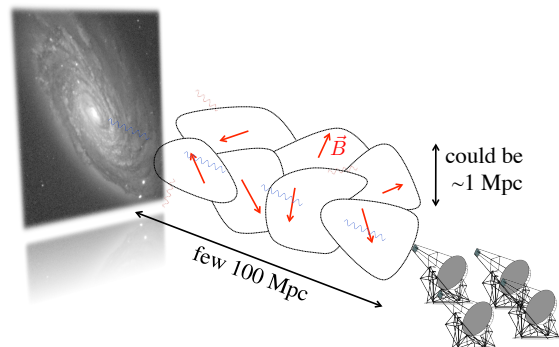


Figure 2.22: Illustration of the modeling of the extragalactic magnetic field

The fact that the imaginary coefficient only applies to the photon part of the wavefunction leads to the change in the overall transparency. In the case of no absorption, the mixing matrix is diagonalized with a rotation angle $\theta$ such that $\tan 2\theta = -2\Delta_B/\Delta_a$. The resolution of the propagation equation in the propagation state basis leads to the probability of transition

$$P_{\gamma \to a} = \frac{1}{2} \frac{1}{1 + (E_c/E)^2} \sin^2 \left( \frac{g_{\gamma a} B_t \, z}{2} \sqrt{1 + \left( \frac{E_c}{E} \right)^2} \right), \text{ with } E_c = \frac{m_a^2}{2g_{\gamma a} B_t} \ . \tag{2.6}$$

The overall 1/2 coefficient in $P_{\gamma \to a}$ accounts for the two polarizations of the photon. A critical energy $E_c$ appears, that defines the energy scale at which strong mixing occurs. From the expression of $E_c$, with cosmological magnetic fields $B \sim 1$ nG, an ALP mass $m_a \sim$ neV and a coupling $g_{\gamma a} \sim 10^{-11}$ GeV$^{-1}$, the critical energy lies at the TeV scale. It follows that the type of ALPs that are concerned by the so-called transparency hint will fall in a region of low masses and with couplings larger than those of same-mass QCD axions.

The full treatment of the transparency problem in the presence of ALPs requires a $3 \times 3$ mixing matrix

48

to account for the two polarization states for the photon, and a description of the magnetic field on the path from the source to the observatory. The extragalactic magnetic field is usually described as patches of coherent domains of 1 Mpc size [174]. The magnetic field strength is the same in all domains but from one domain to the next its orientation changes in a random way (see the sketch of Fig. 2.22). It can be shown (see [175]) that for random orientations and a large number $N$ of domains, the transition probability is reduced to

$$P_{\gamma \to a} \;=\; \frac{1}{3} \left(1 - \exp\left(-3NP_0\right)\right) \;\;,$$ (2.7)

where $P_0$ is the transition probability in one domain. From this expression one would expect to have a $1/3$ drop in the energy spectrum above $E_c$ in the limit $NP_0 \gg 1$, and a flux that is boosted at high energy (typically above the pair-production related cutoff) as described in [176].

At least two facts lead to revise the above statements. First, in practice the limit $NP_0 \gg 1$ is hardly realized. Second, due to the unknown nature of the magnetic field configuration, the prediction on the transmission has an intrinsic variance. Indeed it can happen that the ALPs do not convert back into photons before reaching the Earth, leading in that case to an even more opaque universe. This is nicely illustrated in Fig. 2.23 extracted from [177]. Here the red dot-dashed line corresponds to the conventional opacity in the absence of ALPs and the solid black line is the average prediction with ALPs. It appears that the average transparency is indeed higher than the conventional case at high energy. However, the associated uncertainty on the prediction, in other words the variance related to the randomness of the magnetic field is such that the envelope includes the conventional case. Because of that fact, if observed without ambiguity in the future, such an effect might be seen as an indication for ALP detection but could hardly serve as a firm argument for discovery.
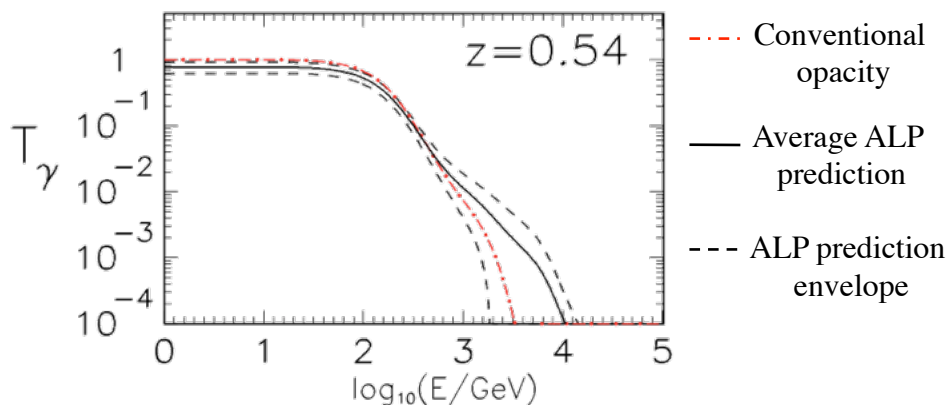


Figure 2.23: Transmission of photons with and without ALPs, the ALP case is ploted with the envelope corresponding to the variance on the prediction of the transparency effect (figure from [177], with permission of the authors).

Another limitation comes from the use of a very optimistic value for the extragalactic magnetic field. For the ALP effect to significantly affect the opacity, magnetic fields of nG strength with Mpc coherence length have to be present in the intergalactic medium. It is actually possible to generate such magnetic fields from inflation or QCD phase transition for instance, but the required strength is very close to current upper limits. This is illustrated in Fig. 2.24 (from [178]), where the different observational constraints on large scale magnetic field appear together with predictions from models (orange thin lines). There the red cross corresponds to the typical parameters used in the ALP analyses. It lies in a region that can be seen as fine-tuned given the size of the still open parameter space. At the moment it seems invoking such a strong magnetic field would be acceptable if the tension in the TeV observations was stronger.

A clever way to avoid using intergalactic magnetic fields is to remark that if the source is magnetized or embedded in a cluster, then the mixing to ALPs could occur essentially around the source. Then,
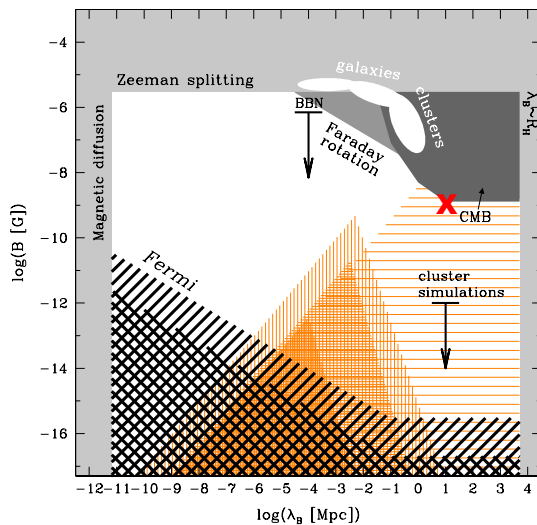
Figure 2.24: Constraints on large scale magnetic fields and prediction of the models. The red cross corresponds to the parameters used for the ALP solution to the transparency "hint" (figure adapted from [178], with permission of the authors). Note that the Fermi limits are seriously questionable, as shown in [179].

the magnetic field of the Milky Way can serve as a target magnetic field to convert back the ALPs into photons. In that case as well, a strong boost can be expected at high energy, as first proposed in [180] and then again in [181]. This effect is used in [161] to estimate possible lower limits on the $g_{\gamma a}$ coupling, but again assuming the tension is real between observations and models for the transparency. Finally it appears that the transparency observable could be used in the future for indication or discovery, if a clear tension was observed. To do so, one might wait for the next generation of gamma-ray telescopes such as CTA to have a significantly larger sample of sources.

The problem of having only a few sources can be circumvented by using an energy band for which detections are numerous. This has been proposed in [182], where the authors remark that if the strong mixing regime is realized, the statistical properties of the observed fluxes from X-ray sources could display features distinctive of ALP effects. In that case, sources would be seen with fluxes reduced by a factor of 1/3 on average. Of course having no access to the absolute intrinsic fluxes, this overall factor is not observable. However because of the random nature of the mixing process in astrophysical magnetic fields, the first and second momentum distribution should have different shapes compared to the conventional case. In [182] the authors claim the observation of anomalous features in the momenta distributions. That result has however shown to be questionable in [183] where the effect is claimed to be caused by outliers. Because in that case the detection would rely on shapes of distributions, it is difficult to infer a constraint without a deeper analysis and this effect is again used to propose a hint. Nevertheless, it illustrates one possible use of the stochastic nature of the mixing in astrophysical environments, which is no more a limitation but becomes a tool for identifying possible ALP effects. In the following, it is shown that a careful study of this randomness can lead to observable effects that are used to set constraints on the ALP parameters.

## 4.3 Constraints on ALP parameters from observations of the high-energy sky

### Effect of the magnetic turbulence

One peculiar effect of photon-ALP mixing is the fact that the magnetic field turbulence can directly imprint features in the energy spectra from high-energy sources. The exact spectral shape one gets at the end is unpredictable, but as shown in [117] the statistical properties of the induced irregularities are a prediction of the ALP model. The authors of [184] and [177] already noticed that in principle the observed spectra should be very irregular in case of strong photon-ALP mixing, without considering the use of the irregularity as an observable.

To account quantitatively for the irregularity, the 2 polarizations of the photon must be considered, so

50

that the evolution of the system after $n$ domains is given by

$$|\psi_n\rangle \ = \ \prod_k \left(P_k^{-1} \ \exp\left[-i\left(E + \mathcal{M}_k^\star\right)s_k\right] \ P_k\right) \ |\psi_0\rangle \ , \quad \text{with} \ \mathcal{M}_k^\star = P_k \mathcal{M}_k P_k^{-1} \tag{2.8}$$

and

$$\mathcal{M}_k \ = \ \begin{pmatrix} -\frac{m_\gamma^2}{2E} - i\frac{\tau}{2z} & 0 & \frac{1}{2}g_{\gamma a}B_t^{(k)}\cos\phi^{(k)} \\ 0 & -\frac{m_\gamma^2}{2E} - i\frac{\tau}{2z} & \frac{1}{2}g_{\gamma a}B_t^{(k)}\sin\phi^{(k)} \\ \frac{1}{2}g_{\gamma a}B_t^{(k)}\cos\phi^{(k)} & \frac{1}{2}g_{\gamma a}B_t^{(k)}\sin\phi^{(k)} & \frac{-m_a^2}{2E} \end{pmatrix} \ . \tag{2.9}$$

$k$ stands for the $k^{\text{th}}$ domain, of size $s_k$, $P_k$ is the rotation matrix between the interaction eigenstates and the propagation eigenstates and the matrix $\mathcal{M}_k$ describes the mixing. The indexes $k$ are there to recall that from one magnetic domain to the next, the corresponding parameters change due to the different orientations of the magnetic field ($B_t$ is the projection of the magnetic field on the polarization plane and $\phi$ is the angle that projection makes with one of the two photon polarization). $m_\gamma = 4\pi\alpha n_e/m_e$ is the effective mass of the photon propagating in a plasma with electron density $n_e$. Examples of spectral oscillation patterns in one domain are given in Fig. 2.25 for different values of $\delta = g_{\gamma a}B_t s/2$, $s$ being the size of the coherent domain. When several domains are considered, the spectrum ends up being very irregular as shown in Fig. 2.26 in the case of an unpolarized beam. For that example, an extragalactic source is considered and the magnetic field is typical of that of a galaxy cluster. The top panel of Fig. 2.26 is the raw signal and the bottom panel is the same signal smoothed by the energy resolution of HESS ($\sim$15%). In that case the critical energy is of order 1 TeV and the effective photon mass is negligible.
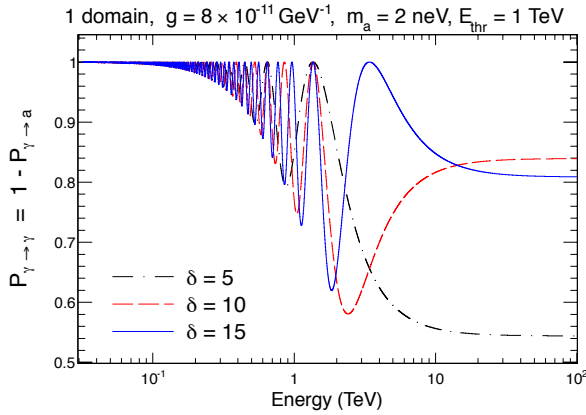


Figure 2.25: Spectral oscillation patterns in domains with coherent magnetic field and different ALP parameters (figure from [117]).
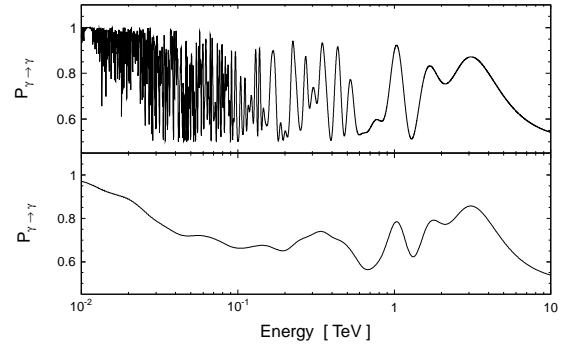


Figure 2.26: Example of ALP induced irregularity in the TeV range (top panel: Raw signal, bottom panel: Signal smeared with HESS resolution, figure from [185, 119]).

Whereas in the case of the extragalactic magnetic field the naive description of the turbulence might be sufficient (essentially because its properties are very poorly known), galaxy cluster magnetic fields may deserve a better treatment. The magnetic field in that case is modeled by a Gaussian field with zero mean and a distribution of modes that is described by a Kolmogorov-like spectrum as in Eq. 2.10:

$$(\delta B)^2 \propto \sigma^2 \frac{k^2}{1 + (kL_c)^\gamma} \ . \tag{2.10}$$

The corresponding power spectrum is modeled by a function resembling that of Fig. 2.27. In galaxy clusters, the typical coherence length of the magnetic field is 10 kpc and the strength of the field is 1 to 10 $\mu$G.
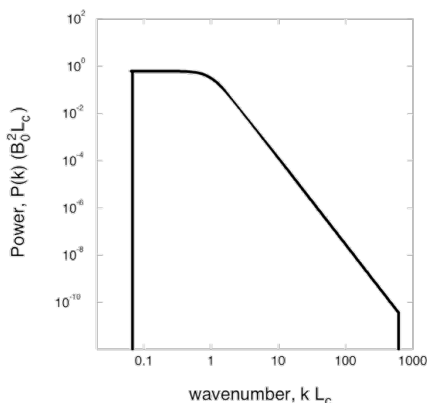
Figure 2.27: Typical power spectrum used for modeling the magnetic turbulence in galaxy clusters.

**Examples of constraints**

The first example of constraints is from the HESS analysis of PKS 2155-304 [185, 119], which is an AGN located at $z = 0.116$. For that source, both the extragalactic magnetic field and the cluster magnetic field can be considered. In the first case, as previously, one has to assume optimistic values of the magnetic field strength for the irregularity signal to be significant. A galaxy cluster is observed around the source, but no magnetic field measurements are available. So in the case of the galaxy cluster magnetic field, conservative values for the strength and the coherence length are assumed (1 $\mu$G and 10 kpc respectively). As HESS observation ranges from hundreds of GeV to a few TeV, from the expression of the critical energy $E_c$ it is straightforward to see that the typical ALP masses that are probed are of the order of $10^{-8}$ eV. In [185, 119], it is shown that the observed energy spectrum does not exhibit strong irregularities. Then an estimator of the irregularity is proposed and numerical simulations are used to exclude sets of parameters that lead to significantly too strong irregular behavior. This exclusion has to be done on a statistical basis as each realization of the magnetic field turbulence is different. The results of the analysis are presented in Fig. 2.28. The method allows to improve the CAST limits in a limited energy range around 20 neV.

Another possibility is to use a source that lies at the center of a well studied galaxy cluster. In that case, the magnetic field properties are derived observationally. This is done by studying the Faraday rotation maps of the polarized radio emission from the cluster (see [186] for a review). These studies allow in principle a determination of the full turbulence power spectrum, yielding the intensity of the magnetic field, its coherence scale and the slope of the turbulence spectrum. A very well studied cluster is Hydra, for which a strong X-ray source is present at the center (Hydra A) [187] . In [188], X-ray data from the Chandra satellite are analyzed in order to derive constraints on ALP parameters. In the case of X-rays from Hydra, the diagonal terms in the matrix of Eq. 2.9 can be simplified. Indeed the pair production related opacity is irrelevant in the case of X-rays (so $\tau = 0$), and the trace of the matrix is dominated by the effective photon mass for $m_a \lesssim 10^{-11}$ eV. So the constraints are expected to extend to arbitrarily low ALP masses below that value. In [188], the irregularity is estimated by performing $\chi^2$ tests when deriving the energy spectrum with a forward folding method. ALP parameters yielding a too high level of irregularity compared to the data are excluded. The corresponding exclusion curve is displayed in Fig. 2.29. It turns out this analysis improves the previous constraints in that mass range from the non-observation of gamma rays associated with SN 1987 A [189].

## 4.4 The transparency effect and prospects for CTA

In Sec. 4.2, the problem of the transparency of the universe is introduced. In the present section, we focus on the results of some studies that claim for an anomaly in the universe opacity [173]. Assuming the problem is real, one scenario that could explain it involves ALPs, which implies the Galactic magnetic field [180, 181]. In this scenario, ALP-photon mixing occur in the source, then the beam propagates towards the Galaxy. When it enters the Galalactic magnetic field (GMF), ALPs can convert back to
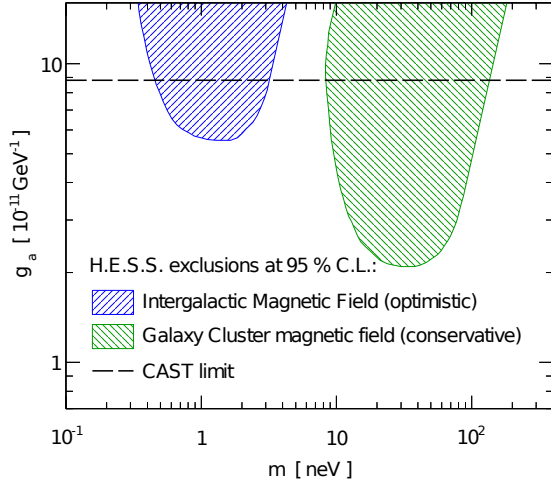
Figure 2.28: HESS exclusion contours from the analysis of PKS 2155-304 energy spectrum (Figure from [185, 119]).
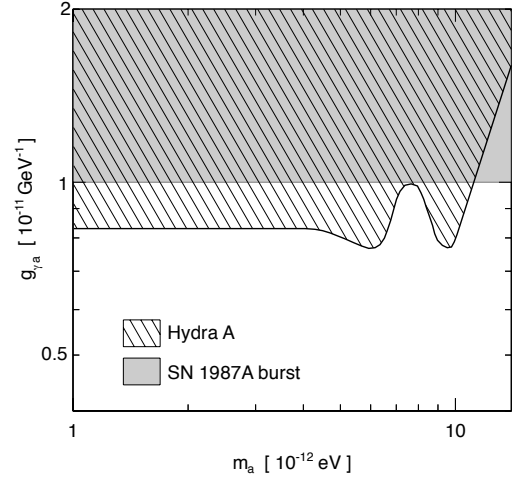
Figure 2.29: Exclusion contours from the analysis of X-ray data from Hydra A (Figure from [188]).

photons. This scenario is particularly interesting because it can lead to large boosts of the flux at high energy. Indeed at energies where the optical depth for extragalactic photons is large, the photonic part of the beam is absorbed on the EBL whereas the ALP part is untouched. In the GMF, ALPs can convert back to photons and lead to anomalies. The anomaly can be measured by comparing the spectral indices in two bands $\Delta\Gamma = \Gamma_{VHE} - \Gamma_{HE}$. $\Delta\Gamma$ is a positive number that is too small in case of an anomaly. As stated in the previous sections, the anomaly, if any, can only be highlighted on a statistical basis, because of the unknown nature of the magnetic fields. In [121], it is argued that CTA will measure enough sources to test this scenario.

It is assumed that the photon-ALP system is in the strong mixing regime and that conversions occur in the source region (as proposed in [180]). The critical energy is chosen to be below 1 GeV, such that the irregularities are below the observational threshold. No IGMF is considered, so the beam exits the source with a certain mix of photons and APLs and the next conversions occur in the Galactic magnetic field. A particular model for the GMF is presented here, other models are considered in [121]. Figure 2.30 shows the probability of conversion from ALP to photons in different regions of the sky. An example of how an extragalactic source spectrum can be affected in shown in Fig. 2.31. In this figure, the red curve is the conventional transfer function, with the EBL-induced cut off. The blue band corresponds to the transfer function when ALPs are considered. The width of the blue band corresponds to the different possible realizations of the mixing conditions in the source, and the back conversion in the GMF. Notice that the blue band includes the conventional prediction, showing that it is in principle impossible to conclude about the anomaly on the basis of a single such source only. Still in Fig. 2.31, the solid black line is the prediction for a single realization of the magnetic field configurations. From this figure one can see that the differences between spectral indices at low energy and high energy is affected by the ALP effects.

An interesting feature of this scenario is related to the scales over which the conversion probability like the one displayed in Fig. 2.30 varies. Based on this map, it is predicted that the $\Delta\Gamma$ anomalies are correlated on small scales and anti-correlated on large scales. A test for this scenario thus consists in measuring the values of $\Delta\Gamma$ for all the sources and build the angular autocorrelation on different scales. If the anomaly is unrelated to the GMF, for instance due to the EBL or to intrinsic source effects, the autocorrelation pattern will be flat, with a null value on all scales. If in turn the anomaly has something to do with the GMF, as in the ALP scenario, then the autocorrelation pattern would peak at small scales. The complete derivation of the statistical variables is described in [121]. The current sample of
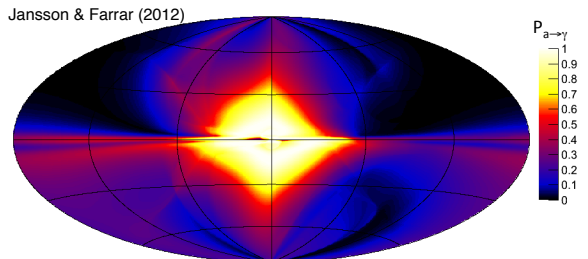
Figure 2.30: Map of probability of conversion from ALPs to photons in the galactic magnetic fields for the model of [190], assuming $g_{\gamma a} = 5 \times 10^{-11}$ GeV$^{-1}$ (figure from [121]).
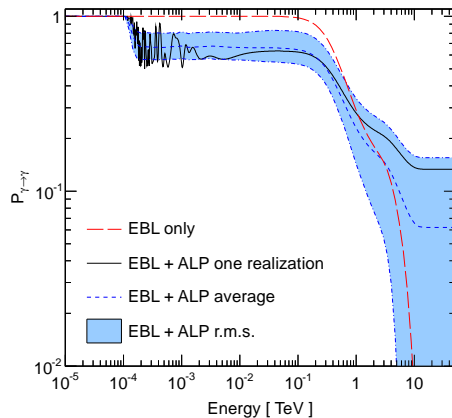
Figure 2.31: Survival probability as a function of the energy. The dashed red line shows the conventional attenuation expected without ALPs. The dashed blue line shows the average over all realizations of the magnetic field while the blue band shows its variance. The solid black line is an example of one realization. An ALP with $g_{\gamma a} = 5 \times 10^{-11}$ GeV$^{-1}$ and $m_a = 1$ neV is considered (figure from [121]).

extragalactic sources is not large enough to base conclusions on. Indeed the constructed autocorrelation pattern is compatible with zero. However, CTA should observe a large number of sources, between 370 and 500 depending on the array configuration [191]. From this sample it will be possible to measure an autocorrelation of the $\Delta\Gamma$ anomaly. This is shown in Fig. 2.32. In this figure, the no-ALP hypothesis corresponds to the horizontal dashed line, and the ALP case is the solid black line. The measurement of the anomaly autocorrelation from the CTA sample of sources are the data points. They clearly indicate that the autocorrelation signal is observable for the used set of ALP parameters, even when the look-elsewhere effect is taken into account (blue boxes).

Other GMF models and possible sources of systematic uncertainties are studied in details in [121]. By varying the ALP coupling strength it is possible to compute the sensitivity of CTA to this observable. This is shown in Fig. 2.33, with this method CTA will be sensitive to ALP couplings to gamma rays of the order of $3 \times 10^{-11}$ GeV$^{-1}$ for ALP masses below $10^{-8}$ eV. In Fig. 2.33, the region of the parameter space that is supposed to explain the transparency anomaly is drawn. Part of this region is excluded by the above mentioned HESS analysis based on irregularities, and part of it will be covered as well by CTA with this method. It is interesting to note that the search for an autocorrelation signal is complementary to other searches and largely independent in terms of potential systematic uncertainties.

Studies of the sensitivity of CTA to the irregularity signal are also conducted [192]. The irregularity signal in that case is stacked over several sources, and it can be shown that five or six sources are enough to obtain the best possible sensitivity. The preliminary results of this study appear in Fig. 2.33, and show that the whole region of the so-called transparency hint will be probed with this method. In the same figure, the expected sensitivity of the planned laboratory experiments ALPS-II [193] and IAXO [194] are also displayed.
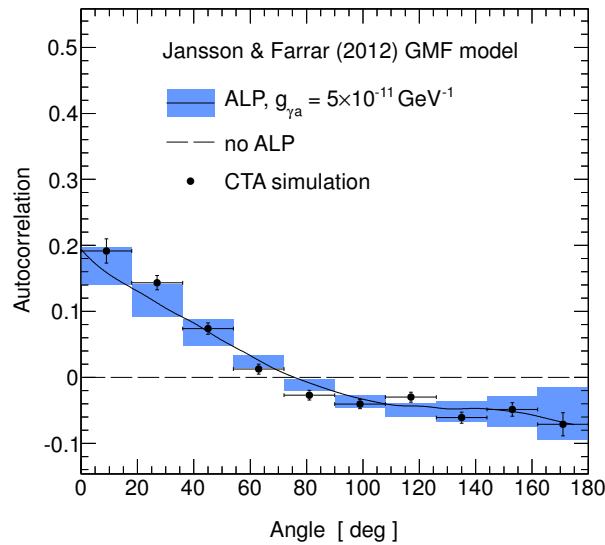
Figure 2.32: Autocorrelation measured on a simulated sample of 500 sources that could be detected by CTA with $g_{\gamma a} = 5 \times 10^{-11}$ GeV$^{-1}$ and the GMF of [190]. The plain black curve shows the ALP prediction for the same coupling strength and GMF model. The blue boxes stand for the uncertainty on the model from the look-elsewhere effect and possible realizations of the magnetic field (figure from [121]).

## 4.5 Conclusions and outlook on the search for ALPs

The study of the high-energy universe is potentially a nice way to search for axion-like particles. The problem of the transparency of the universe to gamma rays can provide an interesting observable, that requires nevertheless the observation of a large number of TeV sources to be robust. This can be achieved with the next generation of Cherenkov telescopes such as CTA. The photon-ALP mixing in astrophysical sources is intrinsically a stochastic process. That fact makes difficult the use of the transparency observations to derive constraints on the ALP parameters. It is noted however that the turbulence of the astrophysical magnetic fields has the effect of inducing irregularities in the energy spectra of sources. The statistical properties of the induced irregularity can be predicted and are used to set limits on the ALP coupling to photons. Because the method is insensitive to the polarization, these constraints go beyond classic ALPs and apply to both $F\tilde{F}$ and $F^2$ types of couplings. In parallel to these astrophysical searches, laboratory experiments like ALPS-II [193] and IAXO [194], the successor of CAST, may provide competitive constraints as well for these low-mass ALPs.
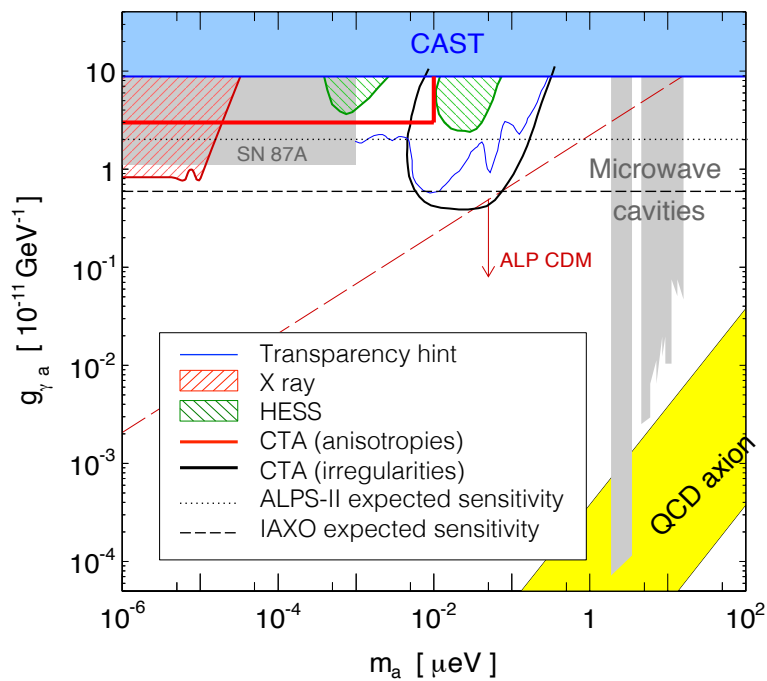
Figure 2.33: ALP parameter space showing the sensitivity of CTA with different analysis methods. Also shown are various constraints in the same mass range from CAST, HESS, observation of SN 1987A and X-ray data. The range of ALP parameters that could explained the opacity anomaly is also shown as "transparency hint". The dotted and dashed horizontal lines are the expected sensitivities of future laboratory experiments (see text).

# Chapter 3

# Development of mirrors for next-generation Cherenkov telescopes

*"I can't see my forehead"*
–Patrick, to Spongebob

## 1 Introduction

In this chapter, the practical problem of how to build instruments that will potentially lead to breakthroughs in the domain is addressed. Since the setup of the CTA consortium I have been involved in working groups where the specifications of the telescopes were defined. Together with the engineers in Saclay we proposed new telescope structures, in particular for the mechanics of the dishes and the arms that hold the camera. Over the years, some of these ideas became less interesting as cost estimates got more precise. Our ideas showed to be less efficient than those of other groups. One remaining of these studies is the quadrupod of the MST prototype in Zeuthen, which was designed in Saclay. I have also been involved in studies based around the idea of using solar energy to run the observatory. Together with engineers, we estimated the power consumption of the facility and the possible means of storage [195]. Later we worked with final-year students from Ecole Centrale Paris and Ecole Supélec who produced a summary document concerning the production and storage of solar energy on CTA site [196]. Whether these studies will be used for the actual facility will depend on the details regarding the final site that will be selected for CTA. We also worked on the development of composite mirrors for MSTs. We built numerous small-size prototypes of all types, using different materials and structures. Such work allowed us to learn a lot about the techniques and the various constraints to take into account. At the end of 2009 we were able to produce small mirrors with fine optical reflectivity. We invested in a nominal size mould and by the Summer 2010 our group was the first to present nominal size CTA mirrors. After that I obtained a funding from ASPERA for a 2-year postdoctoral position. Clementina Medina joined the group and I supervised her work for the building of an optical test bench, which is now considered a reference within the consortium. She has been the corresponding author of a NIM paper in which the mirror design as well as the tests were presented [197]. The following chapter is essentially based on that paper. In addition, we worked in close relation with an industrial company, as mentioned in the last sections of the chapter.

Figure 3.1: Telescopes of the VERITAS array (left) and the MAGIC array (right). The reflectors of these telescopes are composed by small mirror facets.

## 2 General considerations about single-reflector Cherenkov telescopes

As explained in Chap. 2, gamma-ray telescopes are built to image $\gamma$-ray induced particle showers in the atmosphere. The telescopes are deployed in arrays in order to obtain a stereoscopic view of the atmospheric event, which allow efficient off-line background subtraction and a better determination of the $\gamma$-ray arrival direction. Moreover, to gain significantly in sensitivity, the next generation of Cherenkov telescopes requires a very large reflective surface area compared with current instruments.

The next generation of VHE $\gamma$-ray telescope array is CTA, which is currently in the development phase [198]. Two sites, one in the North and one in the South are planned to provide full-sky coverage. In each of these sites an array of telescopes of multiple sizes will be installed; at minimum there will be small (few meters), medium ($\sim$12 m) and large ($\sim$20 m) diameter telescopes (called from now on, Small Size Telescope or SST, Middle Size Telescope or MST and Large Size Telescope or LST, respectively), each optimized for different energy ranges. The final configurations of these arrays are not yet completely defined but the southern site of CTA will be composed of at least 50 telescopes of 3 different sizes and a total of $\sim$5,000 m$^2$ of mirrors will be necessary. The northern site, which is intended to be smaller, will require of the order of 3,500 m$^2$ of mirrors. Such a massive production of mirrors has never been conducted for Cherenkov telescopes so far. The mirror areas used by the currently running observatories is shown in Tab. 3.1 .

Table 3.1: Currently running observatories mirrors characteristics.

| Instrument | Mirror area [m$^2$] | Mirror type |
|---|---|---|
| H.E.S.S. | 1046 | solid glass |
| VERITAS | 440 | solid glass |
| MAGIC | 480 | AlMgSi plates - Al honeycomb |

To achieve such large dish sizes, the reflector of a Cherenkov telescope is composed of many mirror facets, as shown in Fig. 3.1. For CTA mirrors, the glass solution, as used by HESS or VERITAS (see Table 3.1) is too expensive due to the large surface area to be covered. Aside from optical requirements, four aspects drive the choice of mirrors for a large telescope array: 1) cost, 2) weight, which limits the amount of power needed to move the telescopes as well as the construction of the support structure, 3) ease of installation, and 4) longevity or durability, which limits the number of times the mirrors need to be resurfaced or replaced within the lifetime of the instrument. One solution then, is to develop composite mirrors, as in the MAGIC experiment [199].

The mirrors that are described here are developed for the single-reflector version of MST, they are

described in [197]. However, this technique could also be suited for Large-Scale Telescopes (LST). MST and SST could also be built in a different way, using a secondary mirror, as described in Sec. 10. Note that all specifications discussed in this chapter only apply to single-reflector designs. Single-mirror MSTs are 12 m diameter telescopes with Davies-Cotton mount [200], meaning that all facets are identical with spherical shape. A telescope would comprise 84 facets, all of which should focus Cherenkov light onto the focal plane located at a distance of the order of 16 m. Therefore, the individual facets are segments of a ∼30 m diameter reflecting spherical cap. For CTA MSTs, the baseline idea is to use hexagonal mirrors of 1.2 m diameter (flat to flat), with a spherical shape of about 32 m radius of curvature (precise values are given in the following).

# 3  Optical specifications for single-reflector CTA mirror facets

The specifications for CTA MST facets rely on the experience of running experiments and Monte-Carlo simulations [198]. The required sensitivity to observe the dim Cherenkov radiation from an air shower is obtained with the use of a large reflective area that focuses the light onto a sensitive camera. For a given dish design, the focal distance is fixed by the desired field of view of a single telescope (mostly driven by the seeked maximum impact parameter for which one wants to detect an atmospheric shower). Once the focal distance is fixed, the pixel size in the focal plane is chosen in order to optimize the sampling of the atmospheric shower image and not to integrate too much night sky background. This pixel size defines the point spread function (PSF) of a mirror facet, which must focus light from a point-like source onto a single camera pixel. From the work of specifying the telescope parameters conducted within the CTA consortium, the main requirements of MST mirror facets were obtained: a 12 m diameter dish with a focal length of 16.07 m, field of view of ∼6°, and pixel diameter of 5 cm (*i.e.* 3.1 mrad). In comparison to typical requirements for optical astronomy mirrors, the focusing is about 2 orders of magnitude less strict. Optical mirrors typically work at a fraction of $\lambda$ where here the relevant scale is $\sim 100\lambda$. This implies in turn a modest tolerance on the distance of the mirror facets to the focal plane. If the focusing capability of the mirrors is good enough, a difference of few centimeters on their focal lengths would be still acceptable. The mirrors should have good reflectivity in the wavelength range of 300 nm – 600 nm, inferred from the spectrum of Cherenkov light after attenuation in the atmosphere. Each mirror facet should be able to focus at least 85% of distant parallel incident light into 2/3 of a pixel. Out of this light, 80% should end up within 1/3 of a pixel. These requirements translate into the following optical specifications:

- Focal distance: 16.07 m

- On-focus reflectance: ≥85% of an incident parallel beam should be reflected into 2 mrad

- Point spread function: ≥80% of the above mentioned 85% should be focused into 1 mrad

# 4  Mechanical specifications and durability

The mirror facets for CTA should be designed to keep the best optical and mechanical performance for more than a decade in operation conditions on site. To meet the longevity requirements for the CTA instrument, one must define the capacity of the mirror to keep its shape and endurance of the reflective coating. Here, durability refers to the mechanical properties of the mirrors. The support structure on the telescope dish is designed with the assumption that mirror facets should weight less than 30 kg each, and the thickness of the facets should be 80 mm at most. The stiffness of the mirrors should be such that the optical properties are maintained whatever the orientation of the mirror facet and when submitted to a 50 km/h wind load. They shall also be able to withstand a certain degree of physical impact without a reduction of the overall optical quality.

The temperature of operation, inferred from current Cherenkov telescopes sites, would be in the range from -10°C to +30°C, meaning that the optical performance should be maintained within this range. Moreover, the mirrors should not suffer any irreversible change after being submitted to extreme weather conditions as temperatures in the range from -25°C to +60°C and a 200 km/h wind load.

# 5 Composite mirror technology

The choice for a composite design is dictated by the need to have simultaneously a smooth surface on which to deposit reflecting coating, and a stiff and lightweight body. The idea is to hold a glass sheet that has adequate surface roughness to a support structure made of aluminum honeycomb and glass fiber [201]. The mirrors are produced following a cold slumping technique where the structure is shaped against a spherical mold at room temperature. The construction is a two-steps process, shown in Fig. 3.2. In the first step, the back panel is assembled and glued against the mold. The obtained structure is a spherical shell. The RMS deviation from the nominal sphere at this stage is about 12 $\mu$m. As a second step, two glass sheets are glued to each face of the shell. After this stage, the mirror is ready to receive its reflective layer. The gluing of the front glass sheet has the effect of smoothing out the defects, so that the RMS deviation from the nominal sphere after gluing the glass is less than 5 $\mu$m. This value is to be compared to the corresponding value on the mold, which is 7 $\mu$m (the glass sheet somehow flattens out the defects of the mold). In the process, thick aluminum walls are added to each of the six sides. This helps constraining the edges of the front surface to bend correctly. Fig. 3.3 shows an exploded view as well as an actual cutaway view of the mirrors. In Fig. 3.2 and Fig. 3.3, the layers of glue are not displayed. Different types of glue were tested and standard room-temperature polymerizing Araldite resin provides the required stiffness and stability. On the right panel of Fig. 3.3 one can see all components of the mirrors:
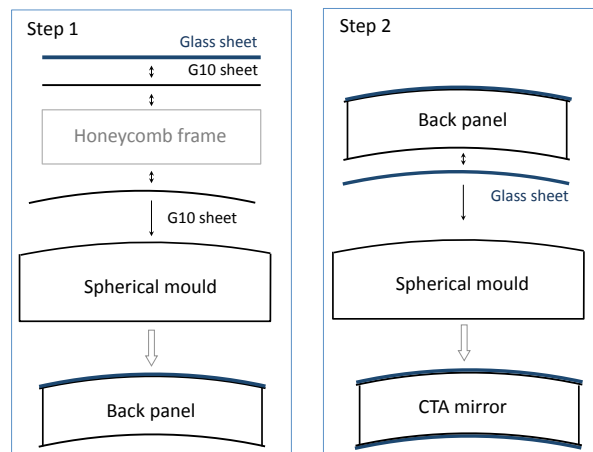


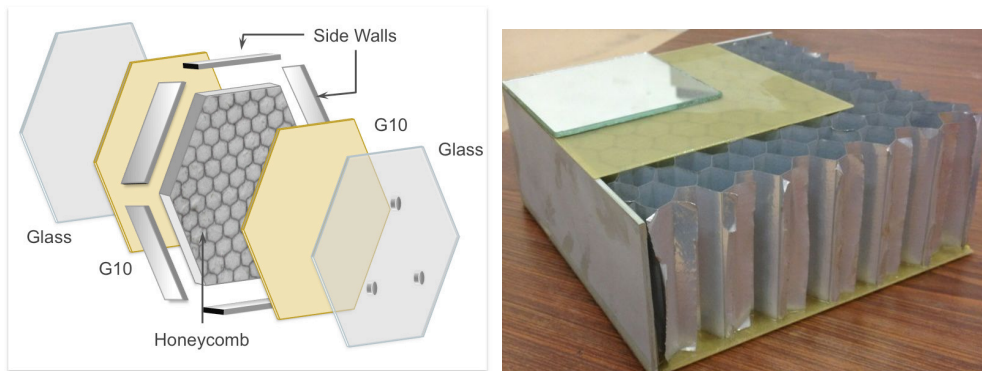Figure 3.2: Mirror assembly process steps.



Figure 3.3: Exploded view of the mirrors (left panel), and real exploded model (right panel).

- 2 glass sheets (2 mm)

- 2 glass fiber (G10) sheets (2 mm)

- The aluminum honeycomb, 80 mm height, with hexagonal cells of 19 mm diameter

- Aluminum side walls (3 mm).

The aluminum foils of the honeycomb are 50 $\mu$m thick and are micro-perforated. That is important when the mirror is held against the mold using vacuum suction. Thanks to these micro holes, the pressure in the cells during this process is everywhere the same. The fact that the honeycomb foils are thin (50 $\mu$m) makes the raw structure (before gluing the G10 sheets) rather flexible in spite of the honeycomb thickness. It is then possible to enforce a spherical shape without the need to have it milled.

The fact that the structure is front-back symmetric (made with the same components) is very important for its thermal behavior. Some earlier prototypes built without the rear glass sheet showed strong variations of their effective focal distance with changes of temperature, due to the differential thermal dilation between the front and the back. In the design presented here, the fully symmetric structure prevents this behavior, such that no significant change of focal distance has been measured when the ambient temperature changed between 10°C and 20°C. Temperature cycles over wider temperature ranges require dedicated climate chambers, these tests have been conducted and are presented in the following.

The mirrors weight 25 kg and are 85 mm thick (note that more recent versions are 60 mm thick). On the rear face, 3 pads are glued on a 640 mm radius circle for the mirrors to be held through the standard CTA 3-point supports. At the end of the fabrication process, the mirror is sealed to make it air tight. Even if air is trapped inside the mirror, it has been checked that a difference of pressure up to $\pm$ 50 mbar between the inside of the outside has no influence on its optical properties.

# 6   Front face coating

The coatings of the mirrors have been performed by an industrial partner, Kerdry Thin Film technologies[1]. The coating is applied using a standard process where material is vaporized in a large vacuum chamber in which the mirror is affixed face-back at the top and spun. At an early stage of the mirror development, back-coating has also been considered. Using thin glass sheets allows to minimize the attenuation in the glass and to protect the reflective layer. However, that solution has been abandoned as it has been shown that it enhances the formation of ice and dew on the mirror surface, making it unusable in cold weather periods.

The coating that is used on the present mirrors is made of an aluminum layer plus three additional layers for protection: $SiO_2$, $HfO_2$, $SiO_2$. Two layers thickness were tested, 120 nm and 240 nm, to determine the effect on durability. The locally measured reflectivity of the mirrors is displayed in Fig. 3.4 in the 200 nm to 700 nm wavelength range in the case of 120 nm 3-layers protection.

# 7   Optical tests

## 7.1   Test bench setup

In order to characterize the prototype mirrors and evaluate them according to the CTA Consortium optical specifications, a "2f" dedicated test bench has been built in an underground room at Irfu Saclay. This facility allows the measurement of three important parameters of the mirrors: the point spread function (PSF), the overall reflectivity ($\rho$) and the effective focal length (f). The principle of a "2f" setup is the following: the mirror is uniformly illuminated by a light source placed at twice the mirror focal length (2f) and close to its optical axis. The light source should be point-like; in practice it is much smaller than the mirror PSF. The 2f method assumes a uniform illumination of the reflective surface, which has to be
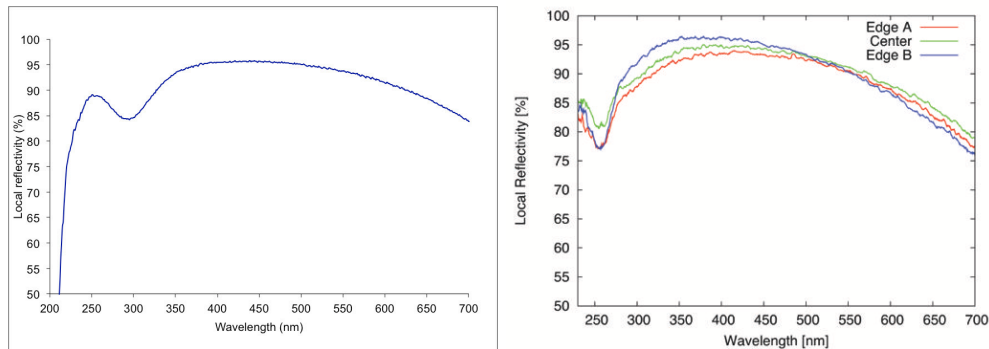
---

[1] www.kerdry.com

Figure 3.4: *Left*: Local reflectivity of the coating between 200 nm and 700 nm measured on a small mirror sample aluminized together with the prototype mirrors. *Right*: Local reflectivity of the coating of the nominal size mirror measured at three different positions. From this it is possible to see that coating properties are uniform within 5 %.

controlled. The light reflected by the mirror will ideally produce at 2f an inverted 1:1 scale image of the source. The spread of this image is twice the mirror PSF.

This image is formed on a screen placed next to the light source and it is captured by a CCD camera. A standard image reduction procedure is performed, and the images are normalized by the individual pixel response using the flat fielding technique. The electronic noise offset and ambient background are subtracted based on dedicated dark observations. From the analysis of the corrected CCD images (intensity and morphology of the spot) one can derive the PSF of the mirror. This is defined as the diameter of the circle containing 80 % ("d80") of the incident light in an circle of 2 mrad diameter (see specifications defined in section 3). Fig. 3.5 shows the schematics of the experimental setup. The mirrors are held by a support attached to the wall. The fine adjustment of the mirror alignment is done remotely in order to place the reflected light spot at the right position on the screen. A movable optical table containing the light sources, the screen, the CCD camera and the photodiode can be displaced along the optical axis allowing a scan of the mirror radius of curvature between 30 m and 37 m. Fig. 3.7 shows the actual setup with its principal components. In order to avoid parasitic reflections, the wall behind the mirror has been covered with a black non-reflective material. The main technical characteristics of the test bench are summarized in Tab. 3.2.

For the determination of the overall reflectivity of the mirrors, the light flux concentrated at the image position is measured with a large surface photodiode (27.9 mm diameter or 1.9 mrad for MST focal distance) and this value is compared to the total light flux illuminating the mirror. This light flux is compared to the flux of four similar photodiodes placed at the sides of the mirror to the total surface of the mirror. The crucial point on the determination of the overall reflectivity is the uniformity of the mirror illumination and the stability of the light source during the acquisition. The uniformity of the light pool at the mirror position is checked regularly and it is found to be within ~3%. The light sources are monitored constantly even though the acquisition time is short enough ($< 1$ min) to avoid any temporal instability. The response of photodiodes placed near the mirror are normalized with respect to the one at the focusing position for each wavelength. There are two limitations for this measurement: one comes from the low sensitivity of the photodiodes at short wavelengths ($<400$ nm) and the other from the reduced size of their effective area with respect to the focused spot size defined on the specifications (the photodiode covers a radius of 0.87 mrad, instead of 1 mrad). The first point could be solved by using a more intense UV light source and increasing the exposure time. For the second point, a solution could be to use the screen image to derive the global reflectivity. This means a precise characterization of the absolute response of the screen and a cross-calibration between the photodiode and the CCD response. This could be done in a future upgrade of the test bench.

A wheel containing four LED sources is connected to a tube which collimates the light towards the
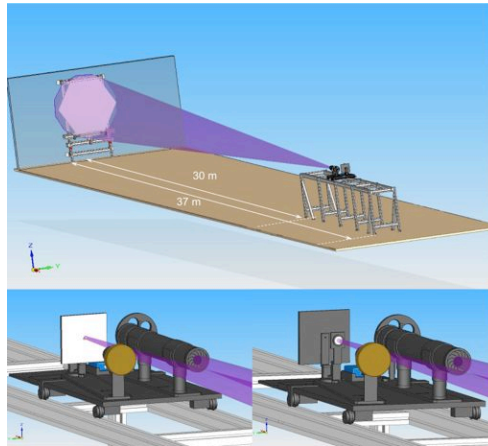
Figure 3.5: *Top*: 2f test bench setup. *Bottom, left*: The movable optical table with the screen in place to record the image with the CCD camera. *Bottom, right* The screen is replaced by a photodiode when the reflectivity of the mirror is measured.

mirror, avoiding spurious light (parasitic reflections, etc) contamination. The four sources have narrow spectra peaked at 365 nm, 400 nm, 460 nm and 523 nm. The LED emitters are 1.5 mm large, which can be safely considered as point like compared to the PSF of the mirror, which is on the order of 1 cm at twice the focal distance. Fig. 3.6 shows the four LED spectra measured with a standard spectrometer.
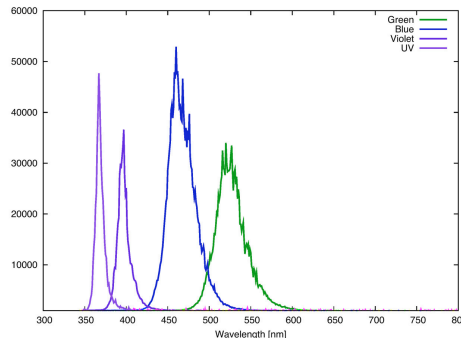


Figure 3.6: Spectra of the four different LED-type sources used for the optical characterization of the mirrors.

| 2f test bench characteristics | |
|---|---|
| corridor length | 37 m |
| mirror mounting | 3 points support |
| alignement of mirrors | remotely controlled |
| optical table | movable |
| screen | 20 cm × 20 cm Alucore (95% of reflectivity from 400 nm) |
| light source type | LED + 1.5 mm pinhole |
| CCD camera | ATIK 4000, sensor Kodak KAI 04022, 1024 × 1024 pixels |
| photodiodes | Active area of 611 mm$^2$ |
| data taking | Windows PC (CCD and photodiodes acquisition) |

Table 3.2: Main characteristics of the optical test bench.

Figure 3.7: *Left*: Optical table. *Center:* Mirror support. *Right:* Photodiodes attached to the mirror support (5 of them are behind the mirror for background monitoring and for light pool uniformity measurement.).

For the determination of the effective focal length, the 80%-containment diameter (d80) is determined at different distances between the mirror and the plane in which the light source and the screen are located. The distance at which the d80 is minimal is defined to be the effective focal length of the mirror. The precision on the determination of the distances is of 1 cm.

## 7.2 Results: optical performance of prototype mirrors

The use of this test bench has been central for evaluating the optical performance of the first pre-series of prototype mirrors. These mirrors were produced using the technique described in Sec. 5. Here we present the results of the most representative prototypes concerning their focusing capability, their global reflectivity and their effective focal length. In the left panel of Fig. 3.8 the CCD image of the spot at the screen produced by the mirror of a light source at 2f is shown. The circle defined by CTA specifications for MST facets (green) and the one corresponding to the photodiode effective area (dashed white) are also shown. In the right panel of Fig. 3.8 the radial distribution of the integrated flux from which the d80 is obtained.
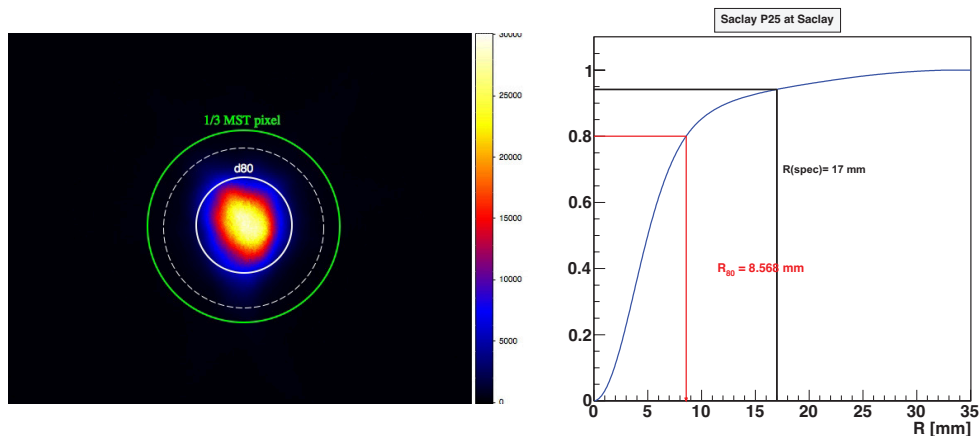


Figure 3.8: *Left*: Image of a LED-type source at twice the nominal focal distance for a prototype mirror. The green circle corresponds to the spot size limit imposed by CTA specification for the MST facets. The white dashed circle represents the surface covered by the photodiode used to measure the focused light flux. The white solid circle represents the 80% containment diameter d80. *Right*: Determination of the radius of the circle containing 80% of the total light focused on a 2/3 of a MST pixel.

The global reflectivity of this mirror for the four available wavelengths is given in Tab. 3.3. It is

measured to be 80% ± 3%. This value fulfills the CTA specifications. In addition one has to notice that the photodiode used here is smaller than the nominal 1 mrad corresponding to 1/3 pixel. It is actually 0.87 mrad diameter at the nominal 2f position. This means that the value obtained for this particular mirror with this method represents only a lower limit for the global reflectivity of the mirrors.

The quoted error includes the systematics related to background contamination, detection efficiency, non-uniformity of illumination and dark currents of the photodiodes and the statistical deviation from 10 successive measurements. This mirror was coated with an Aluminum layer and 3 protective layers ($SiO_2$ + $HfO_2$ + $SiO_2$) with a total thickness of 120 $\mu$m.

Fig. 3.9 shows the parabola fit to the spot size, defined as the d80, measured at different distances from the mirror. The minimum of this parabola is positioned at twice the effective focal length of the mirror. Here it can be seen that for this mirror, it corresponds to its nominal value of 32.14 m.

| Wavelength [nm] | Global Reflectivity [%] |
|:---:|:---:|
| 523 | 81 ± 3 |
| 460 | 83 ± 3 |
| 400 | 80 ± 3 |
| 365 | 83 ± 3 |

Table 3.3: Measured values of the reflectivity for one prototype mirror for the four wavelengths used.
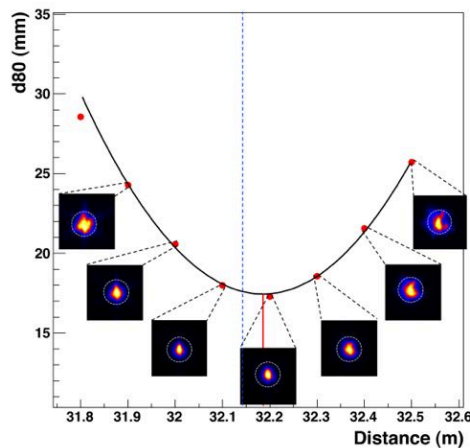


Figure 3.9: Determination of the effective focal length of the mirror facet. The focused spot size is determined at different distances from the mirror and the minimum corresponds to twice the effective focal length. The minimum of a parabola fitted to the measured d80 at different distances is in agreement with the nominal radius of curvature of the mirror. The vertical blue dotted line is the nominal radius of curvature.

# 8 Environmental testing

One of the key issues concerning the composite mirrors presented here is their mechanical stability under quite extreme weather conditions present at many astronomical sites. The telescopes will not be protected by domes and the mirrors will be continuously in contact with the environment. Their optical performance should not be degraded after being exposed to large temperature gradients, heavy wind loads, sun irradiation, sandy and salty atmospheres or impacts such as bird beak impacts. In order to determine the behavior of the mirrors under such conditions we performed a series of tests, designed to reproduce some of the expected environmental conditions, which are presented in the following sections.

## 8.1 Water tightness and stability test

In order to test water tightness and stability of the mirrors design under realistic weather conditions, one of the prototype mirrors has been equipped with internal probes for temperature and humidity. One set of probes was installed on the back G10 layer and a second one on the front side. This mirror was placed outdoor on Saclay site during winter time and data has been recorded for about two months, several times per day. Similar temperature and humidity probes were also installed outside the mirror. In Fig. 3.10 are displayed the locations of the probes in the mirror, and a picture of the mirror standing outdoors.
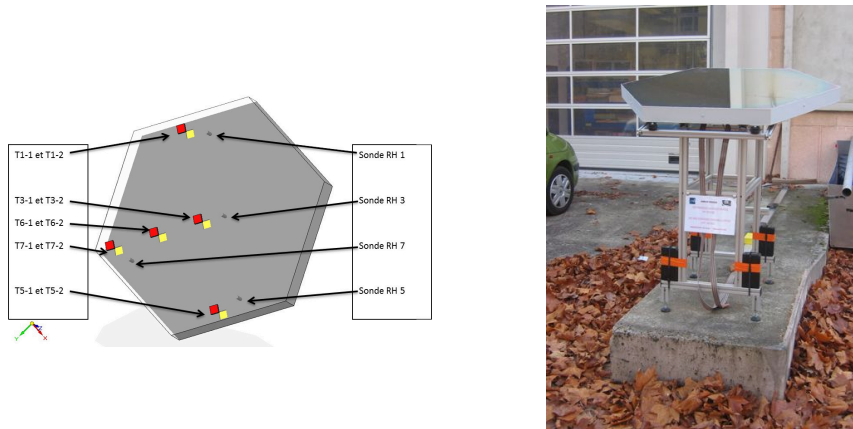


Figure 3.10: *Left*: Scheme of the probe positions inside the mirror. *Right*: Mirror with internal sensors placed outdoor and exposed to severe weather conditions.

After this test, it has been checked that the amount of humidity inside the mirror stayed very small and stable even though the mirror was exposed to highly humid weather conditions. The air stayed dry inside the cells, where relative humidity was always less than 25% and uncorrelated with external conditions. These observations make us confident that humidity does not enter the cells. Note that the mirror used for these tests had holes in the sidewalls whereas mirrors are completely sealed in the baseline design, making them even less subject to water entering.

For the whole duration of the tests, the temperature difference between the two sides of the mirror (back and aluminized front) was always less than 2°C, indicating that no stress is introduced in the materials by a large temperature gradient.

## 8.2 Temperature cycling

**Small Samples**

A set of 25 small, curved (R = 30 m) samples of 100 mm by 50 mm by 80 mm were built following the same procedure as for the full-size mirror and were submitted to a series of thermal cycles in order to study statistically the behavior of such structures after periodic weather condition changes. Note that these samples are not at all representative of the full-size mirrors, as no sidewalls were added to the samples and the curvature was only in one dimension. This test was intended to detect potential problems related to the behavior of the glue used on the mirrors structure or with the G10 itself.

A small climate chamber capable of accommodating a fraction of these samples was used (see Fig. 3.11). Cycles between -20°C to +60°C have been performed for about 38 days, accounting for a total of 150 cycles of 6 hours each. At the end of the cycling, the whole sample survived the temperature variation without any crack or ungluing effect. Moreover, the same resistance to mechanical ripping was observed after the cycles. This indicates that the glue most likely did not degrade and it kept its adherence power.

Figure 3.11: *Left*: Small samples of of 100 mm by 50 mm by 80 mm with a curvature radius of 30 m. *Right*: Samples inside the climate chamber.

**Nominal size prototype mirror**

In order to test the long-term stability of the PSF and the durability of the materials and gluing, a prototype mirror has been submitted to temperature cycling between -25°C and +60°C going through different temperature gradients several times. These tests have been conducted by an external company, as no large enough thermally-controlled room is available at IRFU. The scheme followed for the cycling is shown in Tab. 3.4. The rise and fall time of the temperature in each cycle is 2 hours and the mirrors stay at constant temperature for 1 hour each time.

| Number of cycles | Duration [hours] | Temperature range [°C] |
|---|---|---|
| 4 | 6 | +30 to -5 |
| 4 | 6 | +30 to -10 |
| 4 | 6 | +30 to -15 |
| 4 | 6 | +30 to -20 |
| 4 | 6 | +60 to -25 |

Table 3.4: Temperature cycles applied to one of the MST prototype mirrors.

The optical properties of the mirror were measured before and after the mirror underwent the temperature cycles described above. The mirror survived the test without any crack or ungluing effect. The radius of curvature of the mirror did not show significant change ($\sim 2\%$) and the PSF shows a degradation of about 20%, still fulfilling the CTA requirements. These results are shown in Fig. 3.12. An important point here is that the structure is stabilized after this thermal cycle, meaning that subsequent cycles do not further degrade the PSF.

Further thermal tests will be conducted in the future, in particular with the possibility of following the shift of the focal distance during the cycles themselves using a facility in DESY Zeuthen.

## 8.3   Impact tests

In order to perform the mechanical test simulating impacts, steel balls have been repeatedly dropped on the mirror. The mirror was placed with the coated side upwards. The ball was always released from the same place with no initial velocity. The location of the impacts was analyzed by looking at a deformation on the reflection of a grid placed nearby (see Fig. 3.13). The test was repeated a total of 10 times for each ball diameter and height. The degrees of severity of the tests are defined by the amount of energy deposited during the impact, which depends on these two variables. Three degrees of severity have been tested during these tests (see Tab. 3.5).

The mirror subject to these tests survived without any deformation for the severity levels 1 and 2, fulfilling the CTA specifications. Only after the level 3 severity test the mirror showed visible deformation
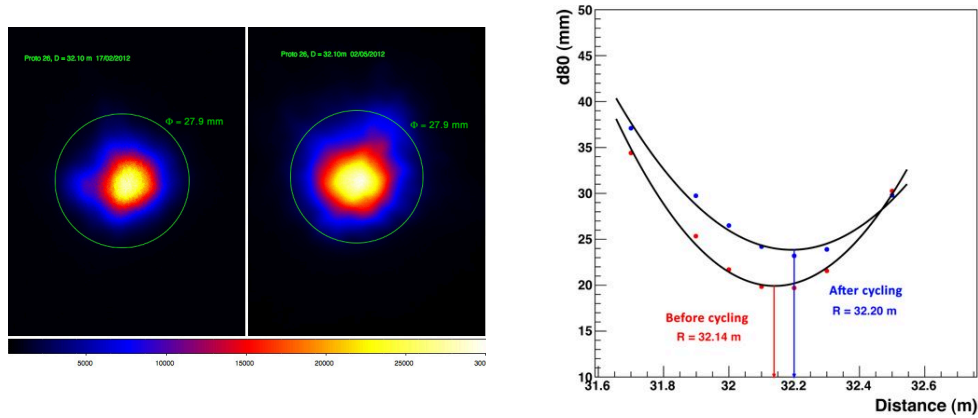
Figure 3.12: *Left*: Images produced at twice the focal distance of the mirror before (left) and after (right) it underwent temperature variations from -25° and +60°. *Right*: Effective focal length before and after the cycling.

| Degree of severity | Diameter [mm] | Height [cm] |
|:---:|:---:|:---:|
| 1 | 20 | 50 |
| 2 | 20 | 100 |
| 3 | 30 | 50 |

Table 3.5: Impact tests severity levels.
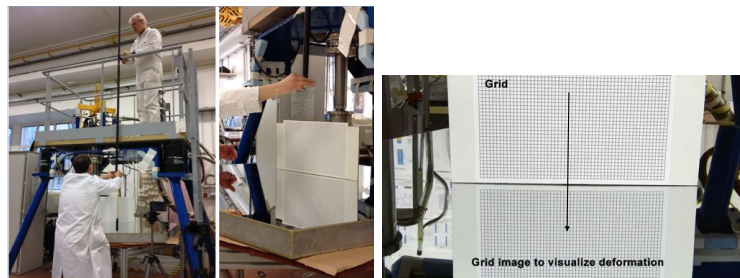


Figure 3.13: Impact test setup.

which can be seen in Fig. 3.14.

## 9 Towards industrialization

Next generation of Cherenkov telescopes will require an enormous amount of mirrors, at least of the order of 5,000 units of the above described facets. Such a massive production cannot be handled in laboratories and rather require the help of the industry. The current design has been thought from the beginning to potentially be efficiently applied to industrial production. To assess the feasibility of such a massive production, a series of 20 mirrors has been produced in industry. The industrial partner that produced the mirrors prototyped at Irfu Saclay is *Kerdry thin films technologies*, who signed a knowledge transfer agreement with Irfu in 2011.
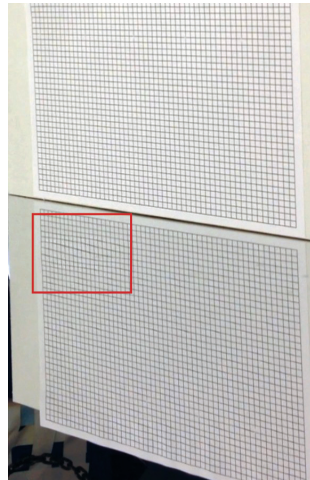
Figure 3.14: Deformation produced on the mirror surface by a 30 mm diameter steel ball dropped 10 times from 50 cm height.
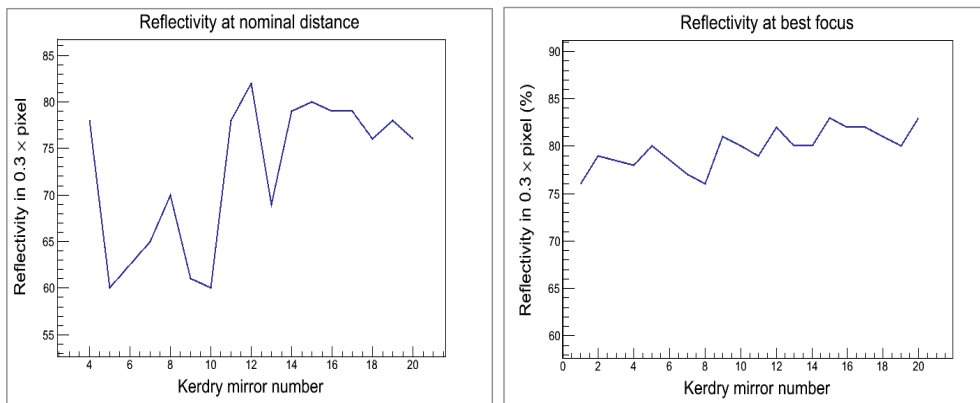


Figure 3.15: Reflectivity versus mirror number, at the nominal distance (left) and at best focus (right), figures from [202].
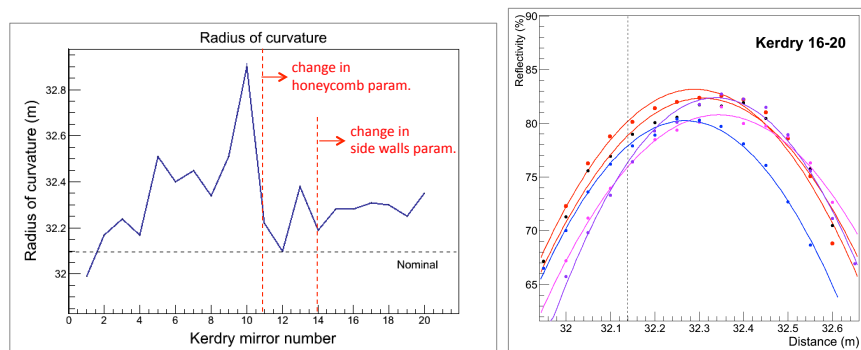


Figure 3.16: Radius of curvature and variation of the reflectivity with distance, figures from [202].

The 20 mirrors have been tested in the underground lab in Saclay. The results for the reflectivity at

69

the nominal distance are shown on the left panel of Fig. 3.15. On the right panel of Fig. 3.15, the results are shown for the same measurement at best focus. It appears that the mirror quality is increasing with their series production number, when measured at their best focus. The conclusion one can draw out of Fig. 3.15 is that some mirrors have good focusing properties but shifts exist in their focal lengths. This is verified with the left panel of Fig. 3.16, here one can see that it took a dozen mirror to stabilize the production in terms of focal length. In the right panel of Fig. 3.16, the reflectivity at different distances is displayed for the last 5 mirrors of the production. These results show a systematic shift of the order of 14 cm on the radius of curvature of the mirrors compared to the nominal value defined by the mould (7 cm in focal length). This shift will have to be taken into account in future productions.

The production of 20 mirrors for ground-based Cherenkov telescopes in the industry showed that it is indeed possible to consider a mass production of these mirrors for the need of future observatories such as CTA. The price of 2,500 euros per mirror facet make them competitive, as it can be further reduced in case of a more massive production.

## 10 Two-reflector designs

This chapter mainly discussed the Davies-Cotton mount for MST facets so far. An alternative design is under study for both MST and SST. The principle is to use a secondary mirror to allow placing the focal plane closer to the primary dish. Doing so, one can use smaller pixels while obtaining larger fields of view. It is also simpler from a mechanical perspective as the camera weight is closer to the center of the whole apparatus. Basically the primary mirrors can act as if the focal plane was behind the secondary mirror. The main difficulty comes from the shape of the secondary mirror, which has to be aspherical. Two-reflector telescopes have never been used for Cherenkov astronomy and there are now two projects of SST. One of them -SST-Gate- is proposed by a consortium of labs in the Paris area that includes Saclay, and already has a prototype (see Fig. 3.17), and the other one is proposed by Italian collaborators. The US part of CTA proposes a two-reflector designs for MST as well, as shown in Fig. 3.17.
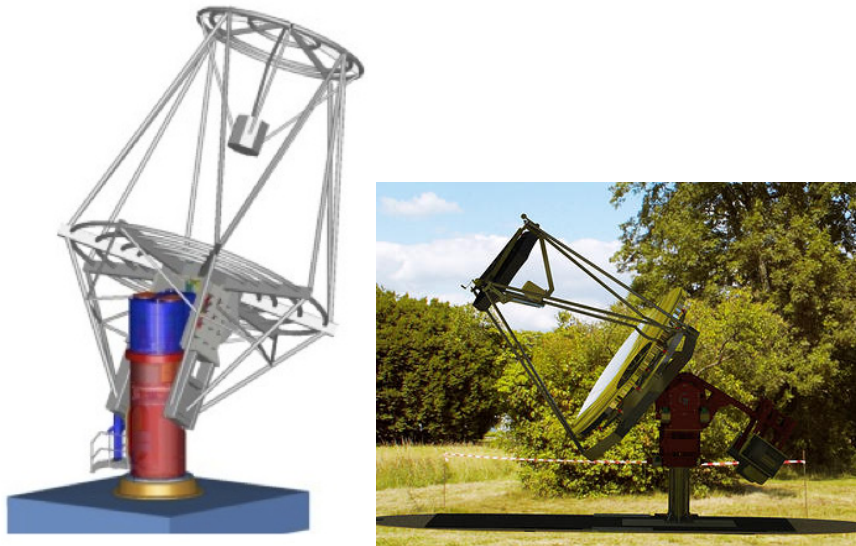


Figure 3.17: Two-reflector telescopes, MST drawing (left) and SST prototype for the Gate project in Paris (right).

It has been attempted to apply the replication method to the construction of the secondary mirror facets of the Gate telescope. The hope was to use large curvature aspherical mould with aspherical shape. Because of the large curvature, when a glass sheet is applied to such a mould, cuts have to be made in

the glass to avoid ripples. It has been shown that it is very difficult to obtain decent shapes, even after a subsequent polishing of the glass, and the method is now abandoned. In the Gate project, both primary and secondary mirror facets will be built by a conventional and more expensive way, making use of polished aluminum pieces.

# 11  Outlook

The Irfu composite mirror facets fulfill the need for CTA MSTs. Beyond the tests presented here, a lot of effort has been put into the definition of common test procedures within the CTA consortium. Mirror samples from all competing groups went through all test benches across Europe. Some tests are not available in Saclay, this is the case of the accelerated aging tests, performed in Durham and Zeuthen, A determination of the surface shape can be performed with a phase measurement deflectometry (PMD) device. It allows a quick measurement of the shape, the focal length and the PSF can then be determined from simulations. It is foreseen that in production, each mirror undergo a PMD test, and a fraction of the order of one tenth of the mirrors undergo a full qualification measurement. It is shown in this chapter that industrialization is feasible. Out of the sample of 20 mirrors produced in Kerdry, the last units present reflectivities in the 80-85% range. Competitor designs show similar performance. Other prototypes have been built in Saclay after the pre-series was finished, and even better performance was obtained, in particular in terms of building efficiency, with a method that allows a one-step gluing. Further prototypes are necessary. It is foreseen to product a larger sample of mirrors, between 50 and 100 units, in order to test for potential failures of the production chain, test the reliability of the mirrors more precisely, and investigate possible changes in the building procedure.

# Outlook

This document presents some key elements of my research activities in the past few years that have followed a coordinated and cohesive approach to tackle fundamental issues at the border of particle physics and astrophysics. In the first part, studies about the origin of high-energy cosmic rays were presented and in particular the hypothetical possibility that some of the observed features in their energy spectra are caused by dark matter. While astrophysical explanations have always been preferred, these new findings were a good pretext at that time to reconsider these search channels. I contributed to quantitative comparisons between observations in different channels, showing in particular that if dark matter particles were at the origin of the cosmic-ray features, they should either have very specific couplings to normal matter, or generate the signal from very dense and nearby regions of our Galaxy called dark matter clumps. These analyses made use of codes for which I participated to the development, such as micrOMEGAs. Dark matter clumps are not observed and are predicted by the structure formation models. Using large numerical simulations, I was able to compute the odds in favor of the presence of such an object, and showed this is very unlikely to be at the origin of the cosmic-ray signals. All together, these studies contributed to ruling out the charged cosmic-ray channels as good observables for DM searches.

This led to considering neutral messengers, such as gamma rays and neutrinos, as better ways to perform indirect searches for dark matter particles. As a member of the HESS collaboration, I have been involved in searches through gamma rays. The second part of this document described some of the work done in this respect. These searches are essential to confirm our current view of the universe's structures, where galaxies form in potential wells induced by dark matter particles. They are the only way to link the microscopic description of dark matter to the dynamics of largest object of the universe. Such searches have been conducted with Fermi and the running Cherenkov telescope arrays. Some of the best constraints on the dark matter particle annihilation cross section reach the cosmologically natural value (Fermi, < 30 GeV), and some are just one order of magnitude above (HESS). My contributions were related in particular to dark matter searches towards dwarf galaxies, from both experimental and phenomenological perspectives. I participated to the HESS analyses and to a study focused on Sagittarius dwarf galaxy. We showed in particular that due to the expected conventional signals, the sensitivity to dark matter in this object is intrinsically limited. Another strategy that I adopted is the blind search for dark matter clumps; in that case it is necessary to use surveys, and to rely on numerical simulations to determine the expected signals. I showed that HESS was already sensitive to clumps with its Galactic survey, and that the future gamma-ray instrument CTA will be sensitive to the cosmologically natural value for the dark matter annihilation cross section.

I investigated other possibilities to conduct fundamental physics research with high-energy gamma rays, and in particular using extragalactic sources. One example developed in this document is the search for hypothetical new particles called axion-like particles. These particles are of interest in the field of high-energy astrophysics for their inclination to modify the opacity of astrophysical media. I conducted in particular a study in which specific opacity properties of the universe are predicted, that can be tested with next-generation Cherenkov telescope arrays. Some computations presented in this manuscript led to the first demonstration that an axion-like particle signal could take the form of irregularities in the energy spectrum of astrophysical high-energy photon sources. This new effect has been used to constrain

the axion-like particle's properties using HESS data and X-ray data, and led to set some of the best constraints to date in some axion-like particle mass ranges. The use of extragalactic sources offers nice perspectives that will be studied in detail, in particular in the framework of the ANR-funded *CosmoTeV* project that I lead.

On the instrumental side, the fifth telescope of the HESS array is now in operation and will improve the sensitivity of the instrument, especially at low energy, a critical range for extragalactic observations and dark matter searches. The next-generation instrument is CTA, to which preparation I participate actively. Most likely, CTA will lead to a significant leap in the field. A very large observatory such as CTA requires to invest a lot of resources in the development of new experimental techniques. An example has been shown in this manuscript with the telescope mirrors. The development of mirrors started in 2008 with a team of physicists and engineers who initially only had limited knowledge of optics for IACTs. I led the Saclay group through the prototyping phase, where some designs were proven more efficient. We converged towards a composite structure that is both cost-efficient and lightweight. I set up a comprehensive test lab in Saclay intended to characterize the optical properties of the mirrors, and built up collaborations to assess their reliability and in particular understand their aging. I participated to the industrial transfer of the concept and we now have a process that is validated at an industrial level. Next steps include the final validation of the process, the running of further tests ensuring the reliability of the mirrors for years, and hopefully the acceptance of our design by the consortium.

All these studies show that the high-energy universe is indeed a unique laboratory to conduct particle physics experiments. Although the experimental conditions are less controlled than in an actual laboratory, some examples presented here show that better sensitivities can sometimes be achieved. These investigations are far from being over and a lot of interesting studies related to fundamental problems can still be addressed using the high-energy universe.

# Bibliography

[1] A. A. Penzias and R. W. Wilson. A Measurement of Excess Antenna Temperature at 4080 Mc/s. *Astrohys. J.*, 142:419–421, July 1965.

[2] G. F. Smoot et al. Structure in the COBE differential microwave radiometer first-year maps. *Astrophys. J. Lett.*, 396:L1–L5, September 1992.

[3] D. Larson et al. Seven-year Wilkinson Microwave Anisotropy Probe (WMAP) Observations: Power Spectra and WMAP-derived Parameters. *Astrophys. J. Supp.*, 192:16, February 2011.

[4] P.A.R. Ade et al. Planck 2013 results. XVI. Cosmological parameters. *Submitted to Astron. Astrophys.*

[5] http://lambda.gsfc.nasa.gov/toolbox/tb_cmbfast_ov.cfm.

[6] Matias Zaldarriaga and Uros Seljak. Cmbfast for spatially closed universes. *Astrophys.J.Suppl.*, 129:431–434, 2000.

[7] http://www.mpa-garching.mpg.de/ volker/gadget/hydrosims/index.html.

[8] Volker Springel and Lars Hernquist. Cosmological SPH simulations: A Hybrid multi-phase model for star formation. *Mon.Not.Roy.Astron.Soc.*, 339:289, 2003.

[9] F. Zwicky. Die Rotverschiebung von extragalaktischen Nebeln. *Helv.Phys.Acta*, 6:110–127, 1933.

[10] F. Zwicky. On the Masses of Nebulae and of Clusters of Nebulae. *Astrophys.J.*, 86:217–246, 1937.

[11] Douglas Clowe, Marusa Bradac, Anthony H. Gonzalez, Maxim Markevitch, Scott W. Randall, et al. A direct empirical proof of the existence of dark matter. *Astrophys.J.*, 648:L109–L113, 2006.

[12] V. C. Rubin, N. Thonnard, and W. K. Ford, Jr. Extended rotation curves of high-luminosity spiral galaxies. IV - Systematic dynamical properties, SA through SC. *Astrophys.J.Lett.*, 225:L107–L111, November 1978.

[13] D. P. Clemens. Massachusetts-Stony Brook Galactic plane CO survey - The Galactic disk rotation curve. *Astrophys.J.*, 295:422–428, August 1985.

[14] C. Alcock et al. The MACHO project: Microlensing results from 5.7 years of LMC observations. *Astrophys.J.*, 542:281–307, 2000.

[15] P. Tisserand et al. Limits on the Macho Content of the Galactic Halo from the EROS-2 Survey of the Magellanic Clouds. *Astron.Astrophys.*, 469:387–404, 2007.

[16] Matthew G. Walker, Mario Mateo, Edward W. Olszewski, Oleg Y. Gnedin, Xiao Wang, et al. Velocity Dispersion Profiles of Seven Dwarf Spheroidal Galaxies. 2007.

[17] Jurg Diemand, Michael Kuhlen, and Piero Madau. Dark matter substructure and gamma-ray annihilation in the Milky Way halo. *Astrophys.J.*, 657:262–270, 2007.

[18] Michael Boylan-Kolchin, James S. Bullock, and Manoj Kaplinghat. Too big to fail? The puzzling darkness of massive Milky Way subhaloes. *Mon.Not.Roy.Astron.Soc.*, 415:L40, 2011.

[19] Anatoly A. Klypin, Andrey V. Kravtsov, Octavio Valenzuela, and Francisco Prada. Where are the missing Galactic satellites? *Astrophys.J.*, 522:82–92, 1999.

[20] James S. Bullock, Kyle R. Stewart, Manoj Kaplinghat, and Erik J. Tollerud. Stealth Galaxies in the Halo of the Milky Way. *Astrophys.J.*, 717:1043–1053, 2010.

[21] Julio F. Navarro, Vincent R. Eke, and Carlos S. Frenk. The cores of dwarf galaxy halos. 1996.

[22] D. Martizzi, R. Teyssier, and B. Moore. Cusp-core transformations induced by AGN feedback in the progenitors of cluster galaxies. 2012.

[23] Shea Garrison-Kimmel, Miguel Rocha, Michael Boylan-Kolchin, James Bullock, and Jaspreet Lally. Can Feedback Solve the Too Big to Fail Problem? 2013.

[24] David N. Spergel and Paul J. Steinhardt. Observational evidence for selfinteracting cold dark matter. *Phys.Rev.Lett.*, 84:3760–3763, 2000.

[25] David Harvey, Eric Tittley, Richard Massey, Thomas D. Kitching, Andy Taylor, et al. On the cross-section of Dark Matter using substructure infall into galaxy clusters. 2013.

[26] Georges Aad et al. Observation of a new particle in the search for the Standard Model Higgs boson with the ATLAS detector at the LHC. *Phys.Lett.*, B716:1–29, 2012.

[27] Serguei Chatrchyan et al. Observation of a new boson at a mass of 125 GeV with the CMS experiment at the LHC. *Phys.Lett.*, B716:30–61, 2012.

[28] J. Beringer et al. Review of Particle Physics (RPP). *Phys.Rev.*, D86:010001, 2012.

[29] Hitoshi Murayama. Impact of neutrino oscillation measurements on theory. *AIP Conf.Proc.*, 721:122–129, 2004.

[30] Gianfranco Bertone, Dan Hooper, and Joseph Silk. Particle dark matter: Evidence, candidates and constraints. *Phys.Rept.*, 405:279–390, 2005.

[31] C.A. Baker, D.D. Doyle, P. Geltenbort, K. Green, M.G.D. van der Grinten, et al. An Improved experimental limit on the electric dipole moment of the neutron. *Phys.Rev.Lett.*, 97:131801, 2006.

[32] R. D. Peccei and Helen R. Quinn. CP Conservation in the Presence of Instantons. *Phys. Rev. Lett.*, 38:1440–1443, 1977.

[33] Frank Wilczek. Problem of Strong p and t Invariance in the Presence of Instantons. *Phys.Rev.Lett.*, 40:279–282, 1978.

[34] Steven Weinberg. A New Light Boson? *Phys.Rev.Lett.*, 40:223–226, 1978.

[35] Jihn E. Kim. Light Pseudoscalars, Particle Physics and Cosmology. *Phys.Rept.*, 150:1–177, 1987.

[36] Andreas Ringwald. Exploring the Role of Axions and Other WISPs in the Dark Universe. *Phys.Dark Univ.*, 1:116–135, 2012.

[37] P. Sikivie and Q. Yang. Bose-Einstein Condensation of Dark Matter Axions. *Phys.Rev.Lett.*, 103:111301, 2009.

[38] Kiwoon Choi. Axions and the strong CP problem in M theory. *Phys.Rev.*, D56:6588–6600, 1997.

[39] Peter Svrcek and Edward Witten. Axions In String Theory. *JHEP*, 0606:051, 2006.

[40] Asimina Arvanitaki, Savas Dimopoulos, Sergei Dubovsky, Nemanja Kaloper, and John March-Russell. String Axiverse. *Phys.Rev.*, D81:123530, 2010.

[41] Andreas Ringwald. Searching for axions and ALPs from string theory. *Plenary talk at PASCOS 2012, Merida, Mexico, June 3-8.*

[42] Paola Arias, Davide Cadamuro, Mark Goodsell, Joerg Jaeckel, Javier Redondo, et al. WISPy Cold Dark Matter. *JCAP*, 1206:013, 2012.

[43] F. Donato, D. Maurin, P. Brun, T. Delahaye, and P. Salati. Constraints on WIMP Dark Matter from the High Energy PAMELA $\bar{p}/p$ data. *Phys.Rev.Lett.*, 102:071301, 2009.

[44] G. Belanger, F. Boudjema, P. Brun, A. Pukhov, S. Rosier-Lees, et al. Indirect search for dark matter with micrOMEGAs2.4. *Comput.Phys.Commun.*, 182:842–856, 2011.

[45] Pierre Brun, Timur Delahaye, Jurg Diemand, Stefano Profumo, and Pierre Salati. The cosmic ray lepton puzzle in the light of cosmological N-body simulations. *Phys.Rev.*, D80:035023, 2009.

[46] O. Adriani et al. PAMELA Measurements of Cosmic-Ray Proton and Helium Spectra. *Science*, 332:69–, April 2011.

[47] O. Adriani et al. The cosmic-ray electron flux measured by the PAMELA experiment between 1 and 625 GeV. *Phys.Rev.Lett.*, 106:201101, 2011.

[48] J.J. Beatty, A. Bhattacharyya, C. Bower, S. Coutu, M.A. DuVernois, et al. New measurement of the cosmic-ray positron fraction from 5 to 15-GeV. *Phys.Rev.Lett.*, 93:241102, 2004.

[49] M. Aguilar et al. Cosmic-ray positron fraction measurement from 1 to 30-GeV with AMS-01. *Phys.Lett.*, B646:145–154, 2007.

[50] Oscar Adriani et al. An anomalous positron abundance in cosmic rays with energies 1.5-100 GeV. *Nature*, 458:607–609, 2009.

[51] M. Ackermann et al. Measurement of separate cosmic-ray electron and positron spectra with the Fermi Large Area Telescope. *Phys.Rev.Lett.*, 108:011103, 2012.

[52] M. Aguilar et al. First result from the alpha magnetic spectrometer on the international space station: Precision measurement of the positron fraction in primary cosmic rays of 0.5˘350 gev. *Phys. Rev. Lett.*, 110:141102, Apr 2013.

[53] O. Adriani et al. PAMELA results on the cosmic-ray antiproton flux from 60 MeV to 180 GeV in kinetic energy. *Phys.Rev.Lett.*, 105:121101, 2010.

[54] P. Picozza, A.M. Galper, G. Castellini, O. Adriani, F. Altamura, et al. PAMELA: A Payload for Antimatter Matter Exploration and Light-nuclei Astrophysics. *Astropart.Phys.*, 27:296–315, 2007.

[55] T. G. Guzik et al. The ATIC long duration balloon project. *Advances in Space Research*, 33:1763–1770, January 2004.

[56] J. Chang, J.H. Adams, H.S. Ahn, G.L. Bashindzhagyan, M. Christl, et al. An excess of cosmic ray electrons at energies of 300-800 GeV. *Nature*, 456:362–365, 2008.

[57] W.B. Atwood et al. The Large Area Telescope on the Fermi Gamma-ray Space Telescope Mission. *Astrophys.J.*, 697:1071–1102, 2009.

[58] M. Ackermann et al. Fermi LAT observations of cosmic-ray electrons from 7 GeV to 1 TeV. *Phys.Rev.*, D82:092004, 2010.

[59] www.mpi-hd.mpg.de/hfm/hess.

[60] F. Aharonian et al. The energy spectrum of cosmic-ray electrons at TeV energies. *Phys.Rev.Lett.*, 101:261104, 2008.

[61] F. Aharonian et al. Probing the ATIC peak in the cosmic-ray electron spectrum with H.E.S.S. *Astron.Astrophys.*, 508:561, 2009.

[62] D.C. Ellison, Luke O.C. Drury, and J.P. Meyer. Galactic cosmic rays from supernova remnants. II: Shock acceleration of gas and dust. *Astrophys.J.*, 487:197–217, 1997.

[63] F. Aharonian et al. A detailed spectral and morphological study of the gamma-ray supernova remnant rx j1713.7-3946 with h.e.s.s. *Astron.Astrophys.*, 449:223–242, 2006.

[64] A.A. Abdo, M. Ackermann, M. Ajello, L. Baldini, J. Ballet, et al. Gamma-Ray emission from the shell of supernova remnant W44 revealed by the Fermi LAT. *Science*, 327:1103–1106, 2009.

[65] V.A. Acciari et al. Observation of Extended VHE Emission from the Supernova Remnant IC 443 with VERITAS. *Astrophys.J.*, 698:L133–L137, 2009.

[66] V.A. Acciari, E. Aliu, T. Arlen, T. Aune, M. Beilicke, et al. Discovery of TeV Gamma Ray Emission from Tycho's Supernova Remnant. *Astrophys.J.*, 730:L20, 2011.

[67] A.W. Strong and I.V. Moskalenko. Propagation of cosmic-ray nucleons in the galaxy. *Astrophys.J.*, 509:212–228, 1998.

[68] Pierre Brun and Timur Delahaye. Cosmic leptons challenge dark-matter detection. *CERN courier*, 49:16–18, 2009.

[69] Lars Bergstrom. RADIATIVE PROCESSES IN DARK MATTER PHOTINO ANNIHILATION. *Phys.Lett.*, B225:372, 1989.

[70] Junji Hisano, Shigeki Matsumoto, and Mihoko M. Nojiri. Explosive dark matter annihilation. *Phys.Rev.Lett.*, 92:031303, 2004.

[71] F. Donato, D. Maurin, P. Salati, A. Barrau, G. Boudoul, et al. Anti-protons from spallations of cosmic rays on interstellar matter. *Astrophys.J.*, 563:172–184, 2001.

[72] R. Duperray, B. Baret, D. Maurin, G. Boudoul, A. Barrau, et al. Flux of light antimatter nuclei near Earth, induced by cosmic rays in the Galaxy and in the atmosphere. *Phys.Rev.*, D71:083013, 2005.

[73] D. Maurin, F. Donato, R. Taillet, and P. Salati. Cosmic rays below z=30 in a diffusion model: new constraints on propagation parameters. *Astrophys.J.*, 555:585–596, 2001.

[74] John W. Bieber, R.A. Burger, Ralph Engel, Thomas K. Gaisser, Stefan Roesler, et al. Anti-protons at solar maximum. *Phys.Rev.Lett.*, 83:674–677, 1999.

[75] Timur Delahaye, Pierre Brun, Fiorenza Donato, Nicolao Fornengo, Julien Lavalle, et al. Anti-Matter in Cosmic Rays: Backgrounds and Signals. *Proc. of XLIVth rencontres de Moriond.*

[76] Pierre Brun. On the Dark Matter Solutions to the Cosmic Ray Lepton Puzzle. *AIP Conf.Proc.*, 1241:343–350, 2010.

[77] Gianfranco Bertone, Marco Cirelli, Alessandro Strumia, and Marco Taoso. Gamma-ray and radio tests of the e+e- excess from DM annihilations. *JCAP*, 0903:009, 2009.

[78] Gert Huetsi, Andi Hektor, and Martti Raidal. Constraints on leptonically annihilating Dark Matter from reionization and extragalactic gamma background. *Astron.Astrophys.*, 505:999–1005, 2009.

[79] Silvia Galli, Fabio Iocco, Gianfranco Bertone, and Alessandro Melchiorri. Updated CMB constraints on Dark Matter annihilation cross-sections. *Phys.Rev.*, D84:027302, 2011.

[80] Julien Lavalle, Jonathan Pochon, Pierre Salati, and Richard Taillet. Clumpiness of dark matter and positron annihilation signal: computing the odds of the galactic lottery. *Astron.Astrophys.*, 462:827–848, 2007.

[81] P. Brun, G. Bertone, Julien Lavalle, Pierre Salati, and Richard Taillet. Antiproton and Positron Signal Enhancement in Dark Matter Mini-Spikes Scenarios. *Phys.Rev.*, D76:083506, 2007.

[82] J. Lavalle, Q. Yuan, D. Maurin, and X.J. Bi. Full Calculation of Clumpiness Boost factors for Antimatter Cosmic Rays in the light of Lambda-CDM N-body simulation results. Abandoning hope in clumpiness enhancement? *Astron.Astrophys.*, 479:427–452, 2008.

[83] Daniel T. Cumberbatch and Joseph Silk. Local dark matter clumps and the positron excess. *Mon.Not.Roy.Astron.Soc.*, 374:455–465, 2007.

[84] Dan Hooper, Albert Stebbins, and Kathryn M. Zurek. Excesses in cosmic ray positron and electron spectra from a nearby clump of neutralino dark matter. *Phys.Rev.*, D79:103513, 2009.

[85] Torsten Bringmann, Julien Lavalle, and Pierre Salati. Intermediate Mass Black Holes and Nearby Dark Matter Point Sources: A Myth-Buster. *Phys.Rev.Lett.*, 103:161301, 2009.

[86] T. Delahaye, F. Donato, N. Fornengo, J. Lavalle, R. Lineros, et al. Galactic secondary positron flux at the Earth. *Astron.Astrophys.*, 501:821–833, 2009.

[87] J. Alcaraz et al. Leptons in near earth orbit. *Phys.Lett.*, B484:10–22, 2000.

[88] Diego Casadei and Veronica Bindi. The local interstellar spectrum of cosmic ray electrons. Direct measurements. *Astrophys.J.*, 612:262–267, 2004.

[89] J. S. Perko. Solar modulation of galactic antiprotons. *Astron. & Astrophys.*, 184:119–121, October 1987.

[90] R. C. Hartman et al. Third EGRET catalog (3EG) (Hartman+, 1999). *VizieR Online Data Catalog*, 212:30079–+, August 1999.

[91] J. Diemand et al. Clumps and streams in the local dark matter distribution. *Nature*, 454:735–738, 2008.

[92] Dan Hooper and Stefano Profumo. Dark matter and collider phenomenology of universal extra dimensions. *Phys.Rept.*, 453:29–115, 2007.

[93] M. Kuhlen, J. Diemand, and P. Madau. The Shapes, Orientation, and Alignment of Galactic Dark Matter Subhalos. *Astrophys. J.*, 671:1135–1146, December 2007.

[94] Massimiliano Lattanzi and Joseph I. Silk. Can the WIMP annihilation boost factor be boosted by the Sommerfeld enhancement? 2008.

[95] Alejandro Ibarra and David Tran. Decaying Dark Matter and the PAMELA Anomaly. *JCAP*, 0902:021, 2009.

[96] Alejandro Ibarra, David Tran, and Christoph Weniger. Decaying Dark Matter in Light of the PAMELA and Fermi LAT Data. *JCAP*, 1001:009, 2010.

[97] Ilias Cholis. New Constraints from PAMELA anti-proton data on Annihilating and Decaying Dark Matter. *JCAP*, 1109:007, 2011.

[98] A. C. Cummings, E. C. Stone, and R. E. Vogt. Evidence for Primary Interstellar Cosmic-Ray Electrons. *International Cosmic Ray Conference*, 1:340, 1973.

[99] R. J. Protheroe. On the nature of the cosmic ray positron spectrum. *Astrophys.J.*, 254:391–397, March 1982.

[100] A.M. Atoian, F.A. Aharonian, and H.J. Volk. Electrons and positrons in the galactic cosmic rays. *Phys.Rev.*, D52:3265–3275, 1995.

[101] F.A. Aharonian, A.M. Atoyan, and H.J. Volk. High energy electrons and positrons in cosmic rays as an indicator of the existence of a nearby cosmic tevatron. *Astron.Astrophys.*, 294:L41–L44, 1995.

[102] Pierre Brun, Gianfranco Bertone, Marco Cirelli, Emmanuel Moulin, Jean-Francois Glicenstein, et al. The Cosmic Ray Lepton Puzzle. 2010.

[103] D. Grasso et al. On possible interpretations of the high energy electron-positron spectrum measured by the Fermi Large Area Telescope. *Astropart.Phys.*, 32:140–151, 2009.

[104] Stefano Profumo. Dissecting cosmic-ray electron-positron data with Occam's Razor: the role of known Pulsars. *Central Eur.J.Phys.*, 10:1–31, 2011.

[105] Pasquale Blasi. The origin of the positron excess in cosmic rays. *Phys.Rev.Lett.*, 103:051104, 2009.

[106] Ilias Cholis and Dan Hooper. Constraining the origin of the rising cosmic ray positron fraction with the boron-to-carbon ratio. *Submitted to Phys. Rev. D*, 2013.

[107] Nir J. Shaviv, Ehud Nakar, and Tsvi Piran. Natural explanation for the anomalous positron to electron ratio with supernova remnants as the sole cosmic ray source. *Phys.Rev.Lett.*, 103:111302, 2009.

[108] Pasquale D. Serpico. Astrophysical models for the origin of the positron 'excess'. *Astropart.Phys.*, 39-40:2–11, 2012.

[109] M. Ackermann et al. Searches for Cosmic-Ray Electron Anisotropies with the Fermi Large Area Telescope. *Phys.Rev.*, D82:092003, 2010.

[110] Ph. von Doetinchem, S. Boggs, T. Aramaki, Ch. Hailey, J. Koglin, et al. The General Antiparticle Spectrometer (GAPS) - Hunt for dark matter using low-energy antideuterons. *PoS*, IDM2010:063, 2011.

[111] Pierre Brun, Emmanuel Moulin, Jürg Diemand, and Jean-François Glicenstein. Searches for dark matter subhaloes with wide-field cherenkov telescope surveys. *Phys. Rev. D*, 83(1):015003, Jan 2011.

[112] A. Viana, M.C. Medina, J. Penarrubia, P. Brun, J.F. Glicenstein, et al. Prospects for a dark matter annihilation signal toward the Sagittarius dwarf galaxy with ground-based Cherenkov telescopes. *Astrophys.J.*, 746:77, 2012.

[113] M. Doro et al. Dark Matter and Fundamental Physics with the Cherenkov Telescope Array. *Astropart.Phys.*, 43:189–214, 2013.

[114] Matias M. Reynoso, Gustavo E. Romero, Maria C. Medina, and Pierre Brun. A model for the high-energy emission from blazars. *Int.J.Mod.Phys.Conf.Ser.*, 08:388–391, 2012.

[115] A. Abramowski et al. Discovery of very high energy gamma-ray emission from the BL Lac object PKS 0301-243 with H.E.S.S. 2013.

[116] A. Barnacka, R. Moderski, B. Behera, P. Brun, and S. Wagner. PKS 1510-089 - a rare example of a flat spectrum radio quasar with very high energy emission. 2013.

[117] Denis Wouters and Pierre Brun. Irregularity in gamma ray source spectra as a signature of axionlike particles. *Phys.Rev.*, D86:043005, 2012.

[118] Denis Wouters and Pierre Brun. Constraints on Axion-like Particles from X-Ray Observations of the Hydra Galaxy Cluster. *Astrophys.J.*, 772:44, 2013.

[119] A. Abramowski, F. Acero, F. Aharonian, F. Ait Benkhali, A. G. Akhperjanian, E. Angüner, G. Anton, S. Balenderan, A. Balzer, A. Barnacka, and et al. Constraints on axionlike particles with H.E.S.S. from the irregularity of the PKS 2155-304 energy spectrum. *Phys. Rev. D*, 88(10):102003, November 2013.

[120] D. Wouters and P. Brun. Prospects for axion-like particle searches through spectral irregularities with CTA. *In preparation*, 2013.

[121] D. Wouters and P. Brun. Anisotropy test of the axion-like particle Universe opacity effect: a case for the Cherenkov Telescope Array. *JCAP*, 1:16, January 2014.

[122] P. Brax, P. Brun, and D. Wouters. High-energy gamma ray and X ray tests of modified gravity. *In preparation*, 2013.

[123] Heinrich Völk and Konrad Bernlöhr. Imaging very high energy gamma-ray telescopes. *Experimental Astronomy*, 25:173–191, 2009.

[124] F. Aharonian et al. Observations of the Crab Nebula with H.E.S.S. *Astron. Astrophys.*, 457:899–915, 2006.

[125] Stefan Funk, G. Hermann, J. Hinton, D. Berge, K. Bernlohr, et al. The Trigger system of the H.E.S.S. Telescope array. *Astropart.Phys.*, 22:285–296, 2004.

[126] M Vivier. *PhD thesis*, IRFU-09-04-T, 2009.

[127] CTA-consortium. Design Concepts for the Cherenkov Telescope Array. 2010.

[128] P. Gondolo et al. DarkSUSY: Computing supersymmetric dark matter properties numerically. *JCAP*, 0407:008, 2004.

[129] F. Aharonian et al. HESS observations of the galactic center region and their possible dark matter interpretation. *Phys. Rev. Lett.*, 97:221102, 2006.

[130] F. Aharonian et al. Observations of the Sagittarius Dwarf galaxy by the H.E.S.S. experiment and search for a Dark Matter signal. *Astropart. Phys.*, 29:55–62, 2008. Erratum-ibid.33:274,2010.

[131] A. Abramowski et al. H.E.S.S. constraints on Dark Matter annihilations towards the Sculptor and Carina Dwarf Galaxies. 2010. Accepted in Astropart. Phys.

[132] J. Albert et al. Upper limit for gamma-ray emission above 140 GeV from the dwarf spheroidal galaxy Draco. *Astrophys. J.*, 679:428–431, 2008.

[133] A.C. Acciari et al. VERITAS Search for VHE Gamma-ray Emission from Dwarf Spheroidal Galaxies. *Astrophys. J.*, 720:1174–1180, 2010.

[134] M. Wood et al. A Search for Dark Matter Annihilation with the Whipple 10m Telescope. 2008.

[135] A. Abramowski et al. Search for Dark Matter Annihilation Signals from the Fornax Galaxy Cluster with H.E.S.S. *Astrophys.J.*, 750:123, 2012.

[136] E. Aliu et al. MAGIC upper limits on the VHE gamma-ray emission from the satellite galaxy Willman 1. *Astrophys. J.*, 697:1299–1304, 2009.

[137] F. Aharonian et al. A Search for a Dark Matter Annihilation Signal Toward the Canis Major Overdensity with H.E.S.S. *Astrophys. J.*, 691:175–181, January 2009.

[138] J. Aleksic et al. MAGIC Gamma-Ray Telescope Observation of the Perseus Cluster of Galaxies: Implications for Cosmic Rays, Dark Matter and NGC 1275. *Astrophys.J.*, 710:634–647, 2010.

[139] Jelena Aleksic. Deep survey of the Segue 1 dwarf spheroidal galaxy with the MAGIC telescopes. *To appear in the 33rd ICRC proceedings*, 2013.

[140] Benjamin Zitzer. Dark Matter Annihilation Limits from Dwarf Galaxies using VERITAS. *To appear in the 33rd ICRC proceedings*, 2013.

[141] T. Arlen et al. Constraints on Cosmic Rays, Magnetic Fields, and Dark Matter from Gamma-Ray Observations of the Coma Cluster of Galaxies with VERITAS and Fermi. *Astrophys.J.*, 757:123, 2012.

[142] A. Abramowski et al. H.E.S.S. observations of the globular clusters NGC 6388 and M 15 and search for a Dark Matter signal. *Astrophys.J.*, 735:12, 2011.

[143] Pierre Brun. Seeking particle dark matter in the TeV sky. *AIP Conf.Proc.*, 1446:268–280, 2010.

[144] M. Ackermann et al. Constraining Dark Matter Models from a Combined Analysis of Milky Way Satellites with the Fermi Large Area Telescope. *Phys.Rev.Lett.*, 107:241302, 2011.

[145] Alex Geringer-Sameth and Savvas M. Koushiappas. Exclusion of canonical WIMPs by the joint analysis of Milky Way dwarfs with Fermi. *Phys.Rev.Lett.*, 107:241303, 2011.

[146] A. Abramowski et al. Search for a Dark Matter annihilation signal from the Galactic Center halo with H.E.S.S. *Phys.Rev.Lett.*, 106:161301, 2011.

[147] H.E.S.S. Collaboration, A. Abramowski, et al. Very-high-energy gamma-ray emission from the direction of the Galactic globular cluster Terzan 5. *Astron. Astrophys.*, 531:L18, July 2011.

[148] M. Niederste-Ostholt, V. Belokurov, N.W. Evans, and J. Penarrubia. Re-Assembling the Sagittarius Dwarf Galaxy. *Astrophys.J.*, 712:516–526, 2010.

[149] F. Aharonian et al. The H.E.S.S. survey of the inner galaxy in very high-energy gamma-rays. *Astrophys.J.*, 636:777–797, 2006.

[150] F. Aharonian et al. Search for Gamma-rays from Dark Matter annihilations around Intermediate Mass Black Holes with the H.E.S.S. experiment. *Phys. Rev.*, D78:072008, 2008.

[151] Matthew R. Buckley and Dan Hooper. Dark Matter Subhalos In the Fermi First Source Catalog. *Phys. Rev.*, D82:063501, 2010.

[152] R. Abbasi et al. Search for Dark Matter from the Galactic Halo with the IceCube Neutrino Observatory. *Phys.Rev.*, D84:022004, 2011.

[153] M.G. Aartsen et al. Search for dark matter annihilations in the Sun with the 79-string IceCube detector. *Phys.Rev.Lett.*, 110:131302, 2013.

[154] Christoph Weniger. A Tentative Gamma-Ray Line from Dark Matter Annihilation at the Fermi Large Area Telescope. *JCAP*, 1208:007, 2012.

[155] G. Raffelt and L. Stodolsky. Mixing of the photon with low-mass particles. *Phys. Rev. D*, 37:1237–1249, March 1988.

[156] S. Aune et al. Search for Sub-eV Mass Solar Axions by the CERN Axion Solar Telescope with He3 Buffer Gas. *Physical Review Letters*, 107(26):261302, December 2011.

[157] S.J. Asztalos et al. A SQUID-based microwave cavity search for dark-matter axions. *Phys.Rev.Lett.*, 104:041301, 2010.

[158] Klaus Ehret et al. New ALPS Results on Hidden-Sector Lightweights. *Phys.Lett.*, B689:149–155, 2010.

[159] R. J. Gould and G. P. Schréder. Opacity of the Universe to High-Energy Photons. *Physical Review*, 155:1408–1411, March 1967.

[160] M. G. Hauser and E. Dwek. The Cosmic Infrared Background: Measurements and Implications. *Annu. Rev. Astron. Astrophys.*, 39:249–307, 2001.

[161] M. Meyer, D. Horns, and M. Raue. First lower limits on the photon-axion-like particle coupling from very high energy gamma-ray observations. *Phys.Rev.D*, 87(3):035027, February 2013.

[162] Herve Dole, Guilaine Lagache, Jean-Loup Puget, Karina I. Caputi, Nestor Fernandez-Conde, et al. The cosmic infrared background resolved by spitzer. contributions of mid-infrared galaxies to the far-infrared background. *Astron.Astrophys.*, 451:417–429, 2006.

[163] F. Aharonian et al. A Low level of extragalactic background light as revealed by gamma-rays from blazars. *Nature*, 440:1018–1021, 2006.

[164] E. Aliu et al. Very-High-Energy Gamma Rays from a Distant Quasar: How Transparent Is the Universe? *Science*, 320:1752, 2008.

[165] V.A. Acciari et al. Discovery of very high energy gamma rays from PKS 1424+240 and multiwavelength constraints on its redshift. *Accepted in Astrophys. J.*

[166] Y. Becherini, C. Boisson, and M. Cerruti. Discovery of VHE gamma-ray emission from the very distant BL lac KUV 00311-1938 by H.E.S.S. *AIP Conf.Proc.*, 1505:490–493, 2012.

[167] Alberto Franceschini, Giulia Rodighiero, and Mattia Vaccari. The extragalactic optical-infrared background radiations, their time evolution and the cosmic photon-photon opacity. *Astron.Astrophys.*, 487:837, 2008.

[168] H.E.S.S. Collaboration et al. Measurement of the extragalactic background light imprint on the spectra of the brightest blazars observed with H.E.S.S. *Astron. Astrophys.*, 550:A4, February 2013.

[169] Denis Wouters et al. H.E.S.S. observations of the distant BL Lac PKS 0301-243. *AIP Conf.Proc.*, 1505:498–501, 2012.

[170] A. Domínguez, J. R. Primack, D. J. Rosario, F. Prada, Gilmore, et al. Extragalactic background light inferred from AEGIS galaxy-SED-type fractions. *MNRAS*, 410:2556–2578, February 2011.

[171] T. M. Kneiske and H. Dole. A lower-limit flux for the extragalactic background light. *Astron. Astrophys.*, 515:A19, June 2010.

[172] M. Ackermann et al. The Imprint of The Extragalactic Background Light in the Gamma-Ray Spectra of Blazars. *Science*, 338:1190–1192, 2012.

[173] D. Horns and M. Meyer. Indications for a pair-production anomaly from the propagation of VHE gamma-rays. *JCAP*, 1202:033, 2012.

[174] Lawrence M. Widrow. Origin of galactic and extragalactic magnetic fields. *Rev.Mod.Phys.*, 74:775–823, 2002.

[175] Yuval Grossman, Sourov Roy, and Jure Zupan. Effects of initial axion production and photon axion oscillation on type Ia supernova dimming. *Phys.Lett.*, B543:23–28, 2002.

[176] M.A. Sanchez-Conde, D. Paneque, E. Bloom, F. Prada, and A. Dominguez. Hints of the existence of Axion-Like-Particles from the gamma-ray spectra of cosmological sources. *Phys.Rev.*, D79:123511, 2009.

[177] Alessandro Mirizzi and Daniele Montanino. Stochastic conversions of TeV photons into axion-like particles in extragalactic magnetic fields. *JCAP*, 0912:004, 2009.

[178] A. Neronov and I. Vovk. Evidence for strong extragalactic magnetic fields from Fermi observations of TeV blazars. *Science*, 328:73–75, 2010.

[179] Timothy C. Arlen, Vladimir V. Vassiliev, Thomas Weisgarber, Scott P. Wakely, and S. Yusef Shafi. Intergalactic Magnetic Fields and Gamma Ray Observations of Extreme TeV Blazars. 2012.

[180] Melanie Simet, Dan Hooper, and Pasquale D. Serpico. The Milky Way as a Kiloparsec-Scale Axion-scope. *Phys.Rev.*, D77:063001, 2008.

[181] Dieter Horns, Luca Maccione, Manuel Meyer, Alessandro Mirizzi, Daniele Montanino, et al. Hardening of TeV gamma spectrum of AGNs in galaxy clusters by conversions of photons into axion-like particles. *Phys.Rev.*, D86:075024, 2012.

[182] Clare Burrage, Anne-Christine Davis, and Douglas J. Shaw. Active Galactic Nuclei Shed Light on Axion-like-Particles. *Phys.Rev.Lett.*, 102:201101, 2009.

[183] Guido Walter Pettinari and Robert Crittenden. On the Evidence for Axion-like Particles from Active Galactic Nuclei. *Phys.Rev.*, D82:083502, 2010.

[184] Linda Ostman and Edvard Mortsell. Limiting the dimming of distant Type Ia supernovae. *JCAP*, 0502:005, 2005.

[185] Denis Wouters and Pierre Brun. Constraints on axion-like particles from gamma-ray astronomy with H.E.S.S. *Proc. of the 48th Rencontres de Moriond*, 2013.

[186] C.L. Carilli and G.B. Taylor. Cluster magnetic fields. *Ann.Rev.Astron.Astrophys.*, 40:319–348, 2002.

[187] B.R. McNamara, Michael W. Wise, P.E.J. Nulsen, L.P. David, C.L. Sarazin, et al. Chandra x-ray observations of the Hydra A cluster: An Interaction between the radio source and the x-ray-emitting gas. *Astrophys.J.*, 534:L135, 2000.

[188] D. Wouters and P. Brun. Constraints on axion-like particles from X-ray observations of Hydra galaxy cluster. *Astrophys.J.*, 772:44, April 2013.

[189] Jack W. Brockway, Eric D. Carlson, and Georg G. Raffelt. SN1987A gamma-ray limits on the conversion of pseudoscalars. *Phys.Lett.*, B383:439–443, 1996.

[190] R. Jansson and G. R. Farrar. A New Model of the Galactic Magnetic Field. *Astrophys.J.*, 757:14, September 2012.

[191] H. Sol, A. Zech, C. Boisson, U. Barres de Almeida, J. Biteau, J.-L. Contreras, B. Giebels, T. Hassan, Y. Inoue, K. Katarzyński, H. Krawczynski, N. Mirabal, J. Poutanen, F. Rieger, T. Totani, W. Benbow, M. Cerruti, M. Errando, L. Fallon, E. de Gouveia Dal Pino, J. A. Hinton, S. Inoue, J.-P. Lenain, A. Neronov, K. Takahashi, H. Takami, R. White, and CTA Consortium. Active Galactic Nuclei under the scrutiny of CTA. *Astroparticle Physics*, 43:215–240, March 2013.

[192] P. Brun and D. Wouters. Cta sensitivity to axion-like particles through spectral irregularities. *in preparation*.

[193] Jan Eike von Seggern. Status of ALPS-II at DESY. pages 72–75, 2011.

[194] E. Armengaud, F.T. Avignone, M. Betz, P. Brax, P. Brun, et al. Conceptual Design of the International Axion Observatory (IAXO). 2014.

[195] C. Veyssière, P. Brun, Corpace O., Micolon P., and Mirabel F. Managing energy issues for the Cherenkov Telescope Array. *CTA note*, 2009.

[196] T. Lacroux, G. Pelton, C. Ribéreau-Gayou, and V. Woillez. Technico-economic study of the means of storage and transformation of electrical energy stemming from photovoltaic panels through alternative methods. *Rapport de l'Ecole Centrale Paris et Supélec*, 2012.

[197] P. Brun, P.H. Carton, D. Durand, J.F. Glicenstein, C. Jeanney, et al. Composite mirror facets for ground based gamma ray astronomy. *Nucl.Instrum.Meth.*, A714:58–66, 2013.

[198] M. Actis, G. Agnetta, F. Aharonian, A. Akhperjanian, J. Aleksić, E. Aliu, D. Allan, I. Allekotte, F. Antico, L. A. Antonelli, and et al. Design concepts for the Cherenkov Telescope Array CTA: an advanced facility for ground-based high-energy gamma-ray astronomy. *Experimental Astronomy*, 32:193–316, December 2011.

[199] G. Pareschi, E. Giro, R. Banham, S. Basso, D. Bastieri, R. Canestrari, G. Ceppatelli, O. Citterio, M. Doro, M. Ghigo, F. Marioni, M. Mariotti, M. Salvati, F. Sanvito, and D. Vernani. Glass mirrors by cold slumping to cover 100 m$^2$ of the MAGIC II Cherenkov telescope reflecting surface. In *Society of Photo-Optical Instrumentation Engineers (SPIE) Conference Series*, volume 7018 of *Society of Photo-Optical Instrumentation Engineers (SPIE) Conference Series*, July 2008.

[200] John M. Davies and Eugene S. Cotton. Design of the quartermaster solar furnace. *Solar Energy*, 1(23):16 – 22, 1957. The Proceedings of the Solar Furnace Symposium.

[201] CTA Consortium. Contributions from the Cherenkov Telescope Array (CTA) Consortium to the ICRC 2011. *ArXiv 1111.2183*, November 2011.

[202] P. Brun. Composite mirror facets for ground based gamma ray astronomy. *To appear in the 33rd ICRC proceedings*, 2013.

# Curriculum Vitae

**Pierre Brun**

Mailing address: Irfu, Bâtiment 141, CEA Saclay, F-91191, Gif-sur-Yvette, France
email: pierre.brun@cea.fr
Phone: +33 16908 4264

## Current situation

- Permanent physicist at the Particle Physics Department of Irfu, CEA Saclay

- Member of the HESS collaboration

- Member of the CTA consortium

## Titles and diploma

- Title of "CEA expert" in particle physics and astroparticle physics since 2009

- PhD in particle physics, Université de Savoie, 2007

- Master of Science, Subatomic physics and astroparticles, Université Joseph Fourier, Grenoble 2004

- Engineer of INP Grenoble, 2004

## Education and jobs

- 2007-present: Physicist at Irfu, CEA Saclay

- 2004-2007: PhD student at the Laboratoire d'Annecy-le-vieux de Physique des Particules. Supervisor: Sylvie Rosier-Lees, Subject : *Indirect and inclusive search for dark matter with AMS-02 space spectrometer*

- 2004-2007: Teaching assistant in mathematics and physics, Université de Savoie

## Scientific activity

- Co-convener of the Astroparticle Working Group of the HESS collaboration: coordination of the prospects, observations and analyses related to astroparticle physics and exotic physics

- Coordinator of the CTA project at CEA

- Principal investigator of the CEA mirror project for CTA

- Principal investigator of the ANR funded CosmoTeV project ("projet jeunes chercheurs") dedicated to the search for new physics with extragalactic gamma-ray sources

- Member of the scientific committee of the French PNHE program (Programme National Hautes Energies) of INSU, dedicated to high energy astrophysics

- Participation to the European Strategy for Particle Physics, organized by CERN, as scientific secretary for the preparatory group, dedicated to astroparticle physics

- Referee for peer-reviewed journals: Physical Review Letters, Physical Review D, The Astrophysical Journal, Journal of Cosmology and Astroparticle Physics, Experimental Astronomy, Chinese Physics Letters, Astrophysics and Space Science Transactions

- Participation to the 2012 in2p3/Irfu prospect, as coordinator of the indirect searches for dark matter

- Participation to the 2012 technology transfer agreement with the Kerdry company in the framework of the CTA mirror project

## Supervision of post-docs, PhD students and master students

- 2011-2014: Supervisor of the PhD work of Denis Wouters, *"Searches for exotic physics with high-energy gamma-ray astronomy"*, 5 refereed publications as corresponding author and 2 publications in preparation, defended June 30th 2014

- 2009-2011: Supervisor of the post-doctoral work of Clementina Medina, on the development and characterization of composite mirrors for CTA, funded by ASPERA, one refereed publication as corresponding author

- 2011: Supervision of the Master 2 internship of Denis Wouters, *"Spectral deconvolution methods for gamma-ray astronomy"*

- 2010: Supervision of the Master internship of Hassna Id Barkach, *"Constraints on the Hubble constant with H.E.S.S."*

- 2009: Supervision of the Master internship of Benoît Avril, *"Phenomenological constraints on particle dark matter models"*

- 2009: NPAC master 2 short internships (3 students), *"CTA telescopes: mechanics and mirrors"*

- 2008: Supervision of the License internship of Hakim Taklanti, *"Interactions of ultra-high energy cosmic rays with the cosmic microwave background"*

- 2008: NPAC master 2 short internships (3 students), *"Experimental methods in H.E.S.S."*

## Teaching

- Since 2009: teaching assistant at Ecole des Mines de Paris (Mines-Paristech): special relativity, quantum physics, statistical mechanics, nuclear physics

- Since 2010: lecture at the Orsay summer school "Rencontres de l'infiniment grand à l'infiniment petit", *Introduction to astroparticle physics*

- Since 2013: teaching assistant at Ecole Nationale Supérieure des Techniques Avancées (ENSTA-Paristech), statistical mechanics

- 2010-2013: lecturer at Université Paris 11, basic physics for adults returning to full-time education

- 2007: lecture a the OHP astroparticle physics summer school, *Measurement of cosmic radiation in space*

## Organization of scientific events

- Member of the scientific advisory committee of the "Particle and Nuclei International Conference PANIC 2014", Hamburg Germany 2014, co-convener of the "Nuclear and Particle Astrophysics" session

- Member of the organizing committee of the "Very High Energy Phenomena in the Universe" international conference, Quy Nhon Vietnam 2014, convener and chair of the "Dark Matter" session

- Organization of the "Rencontres IPhT/SPP", quarterly one-day workshops on specific topics between the Particle Physics Department, and the Theory Division of CEA

- Scientific secretary for the Astroparticle session at the CERN council open symposium on European strategy for particle physics, Krakow 2012

- Member of the organizing committee of the ISAPP 2012 summer school, "Multi-messenger approach in high energy astrophysics", Paris 2012

- Organizer of the international workshop "Dark matter all around", Paris 2010

- Member of the local organizing committee of TeVPA 2010 international conference, Paris

- Organizer (chair) of the international workshop "TANGO in PARIS", Paris 2009

## Outreach

- 2007-2012 Outreach contact person for the Irfu Particle Physics Department

- 2007-2010 ASPERA-outreach contact person for CEA

- Member of the editorial board and co-author of the book "Passeport pour les deux infinis" (ed. Dunod)

- Seminars in high schools ($\sim$5/year) and seminars for the general public ($\sim$2/year), examples: "Elementary particles", "The missing mass of the universe", "Modern astronomy", "CTA and the future of gamma-ray astronomy", "The dark matter problem", "Do antimatter worlds exist?"

## Articles in peer-reviewed journals

**(appear only papers with direct personal implication, all HESS and CTA papers not shown)**

- **Gamma-ray and X-ray astrophysical tests of modified gravity**, P. Brax, P. Brun, D. Wouters, in preparation

- **Prospects for axion-like particle searches through spectral irregularities with CTA**, D. Wouters, P. Brun, in preparation

- **Anisotropy test of the axion-like particle Universe opacity effect: a case for the Cherenkov Telescope Array**, D. Wouters, P. Brun, JCAP 01 (2014) 016

- **Constraints on axion-like particles with H.E.S.S. from the irregularity of PKS 2155-304 energy spectrum**, H.E.S.S. collaboration, Phys. Rev. D 88 (2013) 102003

- **PKS 1510-089 – a rare example of a flat spectrum radio quasar with very high energy emission**, A. Barnacka, R. Moderski, B. Behera, P. Brun, S. Wagner, submitted to Astron. Astrophys.

- **Constraints on axion-like particles from X-ray observations of Hydra galaxy cluster**, D. Wouters, P. Brun, Astrophys. J, 772 (2013) 44

- **Discovery of very high energy gamma-ray emission from the BL Lacertae object PKS 0301-243 with H.E.S.S.**, H.E.S.S. collaboration, accepted for publication in Astron. Astrophys., 2013

- **The AMS-02 lead-scintillating fibres Electromagnetic Calorimeter**, C. Adloff *et al.*, Nucl. Instrum. Meth. A 714 (2013) 147-154

- **Introducing the CTA concept**, CTA Consortium, Astropart. Phys. 43 (2013) 8-13

- **First results from the Alpha Magnetic Spectrometer on the International Space Station: Precision Measurement of the Positron Fraction in Primary Cosmic Rays of 0.5-250 GeV**, M. Aguilar *et al.*, Phys. Rev. Lett. 110 (2013), 14

- **Composite mirror facets for ground based gamma ray astronomy**, P. Brun *et al.*, Nucl. Instrum. Meth. A 714 (2013), 58-66

- **Dark Matter and Fundamental Physics with the Cherenkov Telescope Array**, M. Doro *et al.*, Astropart. Phys. 43 (2013) 189-214

- **Irregularity in gamma ray source spectra as a signature of axionlike particles**, D. Wouters, P. Brun, Phys. Rev. D 86 (2012) 043005

- **Prospects for a dark matter annihilation signal toward the Sagittarius dwarf galaxy with ground-based Cherenkov telescopes** , A. Viana *et al.*, Astrophys. J. 746 (2012) 77

- **Searches for dark matter subhalos with wide-field Cherenkov telescope surveys** P. Brun *et al.*, Phys. Rev. D 83 (2011) 015003

- **Design concepts for the Cherenkov Telescope Array CTA: An advanced facility for ground-based high-energy gamma-ray astronomy**, CTA Consortium, Exper. Astron. 32 (2011) 193-316

- **Indirect search for dark matter with micrOMEGAs2.4**, G. Belanger *et al.*, Comput. Phys. Commun. 182 (2011) 842-856

- **The cosmic ray lepton puzzle in the light of cosmological N-body simulations**, P. Brun *et al.*, Phys. Rev. D 80 (2009) 035023

- **Constraints on WIMP Dark Matter from the High Energy PAMELA antiproton/proton data** , F. Donato *et al.*, Phys. Rev. Lett. 102 (209) 071301

- **Indirect Searches for Dark Matter with AMS-02**, P. Brun, Eur. Phys. J. 56 (2008) 27-31

- **Antiproton and Positron Signal Enhancement in Dark Matter Mini-Spikes Scenarios**, P. Brun *et al.*, Phys. Rev. D 76 (2007) 083506

- **Indirect dark matter search with diffuse gamma rays from the Galactic Center with the Alpha Magnetic Spectrometer** A. Jacholkowska *et al.*, Phys. Rev. D 74 (2006) 023518

## International conference proceedings

- **Multiwavelength study of the region around the ANTARES neutrino excess**, F. Schüssler *et al.*, ICRC 2013, Rio de Janeiro

- **Composite mirror facets for ground based gamma-ray astronomy**, ICRC 2013, Rio de Janeiro

- **Constraints on axion-like particles with H.E.S.S. from the irregularity of PKS 2155-304 energy spectrum**, ICRC 2013, Rio de Janeiro

- **Mirror development for the Cherenkov Telescope Array**, A. Foerter *et al.*, ICRC 2013, Rio de Janeiro

- **Constraints on axion-like particles from gamma-ray astronomy with H.E.S.S**, D. Wouters, P. Brun, Moriond 2013

- **Axion-like particles: possible hints and constraints from the high-energy universe**, TPC 2012, Paris

- **Imprints of axion-like particles in gamma-ray astronomy**, SUSY 2012, Beijing

- **H.E.S.S. observations of the distant BL Lac PKS 0301-243**, D. Wouters *et al.*, Gamma 2012, Heidelberg

- **Axion-like particles imprints in gamma-ray astronomy**, D. Wouters, P. Brun, Patras 2012, Chicago

- **First results on mirror design for CTA at Irfu Saclay**, C. Medina *et al.*, ICRC 2011, Beijing

- **Searches for dark matter subhaloes with wide-field Cherenkov telescope surveys**, P. Brun *et al.*, ICRC 2011, Beijing

- **Seeking particle dark matter in the TeV sky**, FFP11, Paris

- **A model for high-energy emission from blazars**, M. Reynoso *et al.*, HEPRO III 2011, Barcelona

- **Dark matter searches with H.E.S.S.**, RICAP 2009, Rome

- **Technologies of mirror facets for the telescopes of the CTA observatory**, M. Doro *et al.*, ICRC 2009, Lodz

- **Astrophysical boost factor and dark matter indirect detection**, T. Delahaye *et al.*, TAUP 2009, Gran Sasso

- **Mirror development for CTA**, A. Foerster *et al.*, SPIE 2009, San Diego

- **The Cosmic Ray Lepton puzzle**, P. Brun *et al.*, TANGO in PARIS, 2009, Paris

- **On the dark matter solution to the cosmic ray lepton puzzle**, TeVPA 2009, Stanford

- **On the dark matter solution to the cosmic ray lepton puzzle**, Windows on the Universe 2009, Blois

- **Antimatter in cosmic rays: background and signals**, T. Delahaye *et al.*, Moriond 2009

- **Dark matter searches with H.E.S.S.: nearby dwarf galaxies and IMBH mini-spikes**, E. Moulin *et al.*, Gamma 2008, Heidelberg

- **Indirect searches for dark matter with AMS-02**, PIC 2008, Annecy

- **Enhancement of the dark matter positron signal in the intermediate mass black holes scenario**, TeVPA 2007, Madison